

Assessment of beach face slope extraction and monitoring with ICESat-2

From local to global level

Master Thesis

Daniel Guerra Medina

Delft University of Technology

Assessment of beach face slope extraction and monitoring with ICESat-2

From local to global level

by

Daniel Guerra Medina

Student number: 5384338
dguerramedina@gmail.com | +34646547812
MSc student Geoscience and Remote Sensing

to obtain the degree of

Master of Science
in Civil Engineering

at the Delft University of Technology,
to be defended publicly on Tuesday June 22, 2023 at 9:30.

Thesis committee:	PhD candidate Floris Calkoen,	TU Delft/Deltares
	Dr. Antonio Moreno Rodenas	Deltares
	Dr. Arjen Luijendijk	TU Delft/Deltares
Chair assessment committee:	Dr. Roderik Lindenbergh	TU Delft

Preface

This thesis is the result of approximately 8-9 months of research at Deltares and concludes my master in Civil Engineering, track of Geoscience and Remote Sensing, at the Faculty of Civil Engineering and Geosciences at the Delft University of Technology. I would like to profoundly thank to all my supervisors, Roderik, Arjen, Antonio, and Floris for the opportunity of doing this master thesis with them, as well as their valuable guidance, discussions, feedback, ideas, and enthusiasm throughout one of the most insightful and learning academic stages of my life.

I am grateful for being able to combine topics that I am passionate about, coastal morphology, big data, and remote sensing, and do so while being guided by knowledgeable people from TU Delft and Deltares. I have grown thanks to the different experiences and knowledge that I have lived and obtained with them and this is irreplaceable.

Furthermore, I would like to thank all my friends in Netherlands, and back home in Canary Islands, as well as to my family for their support, kindness, and necessary distractions that helped me to keep going and give the best of myself. Finally, I want to express my gratitude to my parents, Luis and Araceli, and especially my grandmother, Rosa, for always being there.

*Daniel Guerra Medina
Delft, June 2023*

Abstract

Coastal areas are appealing for human beings and are the most populated areas of the world. Therefore, coastal processes have large impacts on economy and on millions of people's lives. Not only processes such as erosion, extreme events, and flood events must be understood and monitored, but the uncertainty given by the rapid climate change on these processes and on coastal systems pose a bigger issue on these populated areas. One of the key parameters of coastal processes, which is notably required for modelling coastal floods, is the beach face slope. Unfortunately, there is a lack of a reliable global dataset of the steepness of the beach face, which has been indicated to be key limitation for developing operational coastal inundation forecasting systems, as well as for quantifying the run-up and set-up contribution at the shoreline relative to global sea-level-rise.

In this report, a methodology for providing this parameter at a global level by using a LiDAR-based satellite (ICESat-2) is presented. Here, the accuracy of the beach face slope estimation, its dependency on the angle and distance between ICESat-2 measurements (passes) and the transect perpendicular to the coastline they are projected into (transect), a spatial and temporal exploration of ICESat-2 measurements on world's coasts, as well as the limitations and opportunities of this methodology are presented.

The findings of this study reveal strong visual agreement between the beach profiles and beach face profiles obtained from the validation datasets and ICESat-2. Moreover, the computed metrics, including the Mean Absolute Error (MAE), Mean Squared Error (MSE), and Root Mean Squared Error (RMSE), present low values, indicating a high level of agreement. The MAE values, ranging from 9 to 34 cm, not only demonstrate good agreement within the beach and beach face profiles but also indicate that the errors fall within the inherent variability of the beach. For assessing the impact of the angle and distance between passes and transect on the beach face slope extraction, synthetic data is generated using Digital Elevation Models (DEMs). The results demonstrate that long and spatially homogeneous beaches withstand larger α , whereas smaller, more variable, and pocket-shaped beaches are more sensitive to large angles due to the rapid decrease of spatial information alongshore. Nevertheless, regardless of the beach type, the closer the synthetic ICESat-2 measurements intersect over the beach face, the more likely the extracted beach face slope is to match the actual one. For both analysed cases, the beach face slope can be extracted with a tolerable level of uncertainty up to 60 degrees, and if the synthetic data is close to the beach face, the angle that it bears can be increased up to 70-80 degrees.

The novel methodology for upscaling the beach face slope extraction is validated using the Dutch yearly coastal dataset, JARKUS. The results reaffirm the dependence of the beach face slope on the angle between pass and transect. It is concluded that even though further refinement of the algorithm for demarcating the beach face is necessary, the extraction of beach face slopes can be implemented on a global scale, if some challenges are overcome. Moreover, this methodology yields a valuable byproduct in the form of cross-shore profiles, which can be extracted globally with high accuracy. This additional output enhances the utility and versatility of the methodology. Additionally, a spatial and temporal exploration of ICESat-2 ATL03 data on the world's coasts, by globally sampling boxes of 20 km², is implemented. Then, by analysing the preliminary results from boxes already processed, it is observed that these boxes can encompass anywhere from 0 to 160 passes over the course of the available 5-year data. On average, approximately 63 passes are recorded within each box. From this analysis, it is concluded that particular coastal stretches, depending on their geometry and cloud coverage, can be effectively monitored for beach face slope changes using ICESat-2. Moreover, from the information extracted from these boxes, a map is being constructed for the purpose of revealing potential areas where the extraction of beach face slopes are possible given the beach geometry and availability of data. In summary, this study provides a novel methodology that sets the basis for a new era of coastal management and monitoring using LiDAR-based satellites at a global level.

Contents

Preface	i
Abstract	ii
Nomenclature	iv
1 Introduction	1
1.1 Objective and research questions	3
1.2 Structure of the report	4
2 Background	5
2.1 Beach face slope	5
2.2 Extracting beach face slopes: from manual techniques to elaborated workflows using remote sensing devices	7
2.3 ICESat-2	9
2.3.1 ATLAS	9
2.3.2 Orbit, coverage, and sampling geometry	10
3 Data and Study Areas	13
3.1 ICESat-2 ATL03 data	13
3.2 CoastScan dataset	15
3.3 RTK-GPS dataset	17
3.4 Optical imagery: Water Occurrence Probability layer	18
3.5 Synthetic ICESat-2 ATL03 data	20
3.6 The JARKUS dataset	23
3.7 Global Coastal Transect System and global coastal buffer	23
4 Methodology	25
4.1 Assessing ICESat-2 accuracy for beach features	26
4.1.1 CoastScan	26
4.1.2 RTK-GPS	30
4.2 Generating and analysing synthetic ICESat-2 ATL03 data	30
4.3 Extracting beach profiles and subsequent beach face slopes at a global level	33
5 Results and Discussion	36
5.1 ICESat-2 validation: CoastScan and RTK-GPS	36
5.1.1 CoastScan	36
5.1.2 RTK-GPS	39
5.2 Synthetic ICESat-2 ATL03 data	41
5.3 Validation of methodology and ICESat-2 using JARKUS	48
5.4 ICESat-2 on coastal areas world-wide distribution	55
6 Conclusions and Recommendations	63
6.1 Conclusions	63
6.2 Recommendations	66
References	67
A Profiles	71
B Global Boxes Sample	73

Nomenclature

The different nomenclatures and abbreviations employed throughout the document are presented below.

Abbreviations

Abbreviation	Definition
ATLAS	Advanced Topographic Laser Altimeter System
AHN 2	Actueel Hoogtebestand Nederland 2
CRS	Coordinate Reference System
DEM	Digital Elevation Model
GCTS9	Global Coastal Transect System 9
GEDI	Global Ecosystem Dynamics Investigation
HDF-5	Hierarchical Data Format 5
ICESat	Ice, Clouds, and Elevation Satellite
ICESat-2	Ice, Clouds, and Elevation Satellite 2
IMU	Inertial Measuring Unit
JARKUS	Jaarlijkse Kustmetingen
LECZ	Low Elevation Coastal Zone
LiDAR	Light Detection And Ranging
MAE	Mean Absolute Error
MSE	Mean Squared Error
MSL	Mean Sea Level
NAP	Normaal Amsterdams Peil
NDWI	Normalized Difference Water Index
NSDIC	National Snow and Ice Data Center
PCL	Photon Counting LiDAR
PE	Percentage Error
POD	Precision Orbit Determination
PPD	Precision Pointing Determination
RD	Rijksdriehoeks-coordinates
RGE	Référentiel à grande échelle
RMSE	Root Mean Squared Error
RTK-GPS	Real Time Kinematics-Global Positioning System
SLR	Sea Level Rise
SNR	Signal-to-Noise Ratio
TLS	Terrain Laser Scanner
UNEP	United Nations Environment Programme
WOP	Water Occurrence Probability

1

Introduction

Human beings are drawn to coastal areas due to the vastness of opportunities and activities that they offer. Coastal areas are defined by the United Nations Environment Programme, *UNEP*, as those within 100 kilometers of the coast and, due to the former, they are densely populated, with approximately 38% of the world's population living in these areas [1]. Understanding coastal systems and processes is essential for developing prevention and mitigation strategies, which rely on monitoring critical parameters, to minimize the adverse socioeconomic effects of extreme events on coastal areas. Besides, the uncertainty on the future world climate as a result of the human induced climate change makes necessary a continuous monitoring of beaches across the globe. However, planet Earth contains 1,634,701 km of coastline [2], and monitoring any parameter in such a large and changing area, subject to different weather conditions and comprising different geomorphological features has not been feasible. Nevertheless, the rapid developments in remote sensing science might allow for the first time to consistently monitor these extensive systems.

Coastal areas, and especially settlements in coastal lowlands, are increasingly impacted by coastal hazards as the climate is changing, yet these lowlands are densely settled and growing rapidly. The Low Elevation Coastal Zone (LECZ), area below the 10 metres above sea level, covers 2% of the world's land area but contains 10% of the world's population and 13% of the world's urban population [3]. To support their ecosystem services but also to protect these areas from the increasing risk of hazards induced by climate change, such as cyclones/hurricanes, as well as a rising sea-level [4], humans influence the shore and shoreline evolution [5].

However, the coast in general, and beaches in particular, constitute systems with highly nonlinear, complex dynamics that are very vulnerable to the individual or joint action of different types of natural hazards, which can lead to erosion or flooding processes with significant impacts [6]. Hence, research on the different topics that have an effect on coastal areas are of keen importance for a better understanding and monitoring of the processes taking place on these systems. This will lead to a reduction on the extent of the socioeconomic impacts that coastal phenomena might have on coastal areas. For this, coastal engineers and planners must improve their models for understanding, predicting and mitigating the processes and impacts of the different hazards that affect the coast. Nevertheless, in order to do so, certain key parameters such as the beach face slope, are necessary inputs to these models, and these may not always be available. This applies for the main parameter of this research, the beach face slope. Overall, the beach face slope, the steepness of the beach face (see Figure 1.1), is an important parameter in understanding the behavior and evolution of the shoreline and coastal areas, and it is implicitly considered when making decisions about coastal development and management.

The absence of a comprehensive dataset for the beach face slope has been identified as a key limitation for developing operational coastal inundation forecasting systems [8], as well as for quantifying the wave run-up and set-up contribution at the shoreline relative to global sea-level-rise [9, 10]. This parameter is also a useful proxy for surf-zone hydrodynamics in the absence of costly surf-zone bathymetric surveys, and can provide insights into the beach swimmer safety and wave set-up across the surf-zone [11].

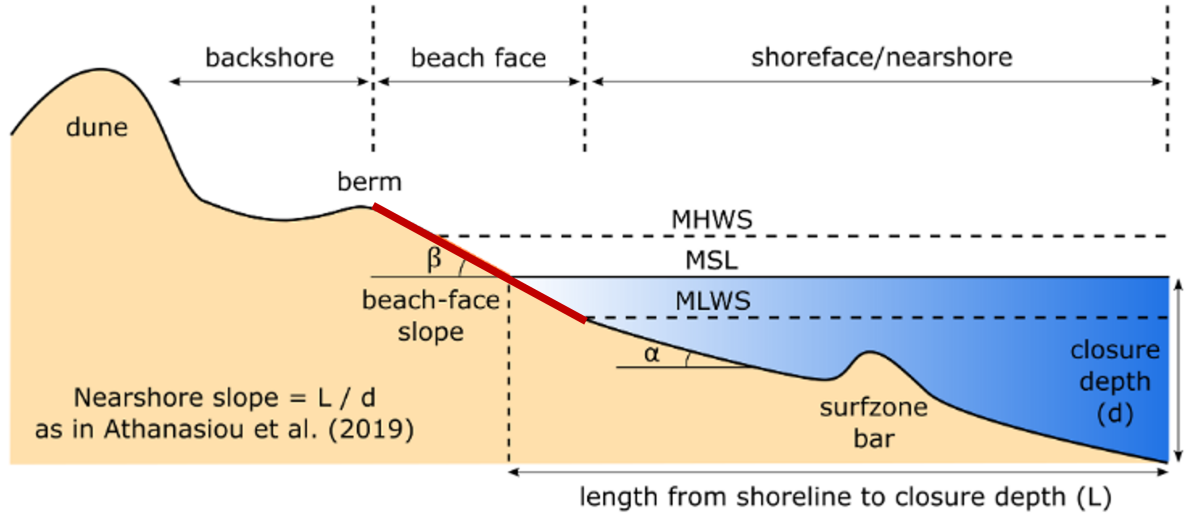


Figure 1.1: Generalized beach and nearshore profile showing names of major beach features and zones, highlighting in red the section and slope of interest. Adapted from Coastal Engineering Research Center, 1984 [7].

Nevertheless, even though it is a highly important parameter for modelling coastal processes, methods or techniques for obtaining this parameter at a global, or even continental scale, for a correct monitoring remain unavailable. A wide range of techniques for measuring beach face slopes are available, such as simple cross-beach measurements using theodolites, Abney levels, dumpy levels, or extracting them from detailed topographic profiles, which can be constructed using traditional surveying methods or modern technologies such as laser scanners, RTK-GPS measurements, unmanned aerial vehicle, or airborne LiDAR [12]. However, field measurement campaigns are time and resource consuming and unfeasible to implement for larger spatial scales. Moreover, in some coasts, the presence of intricate topography and/or bathymetry, currents, and energetic beaches makes manual methods challenging, dangerous and slow. Besides, even though the latter techniques allow a faster extraction of the parameter than the manual and laborious techniques, these can be only applied up to a local or regional scale and may require substantial financial resources.

To overcome the lack of a comprehensive beach face slope dataset, Athanasiou et al., 2019 [13] provides a complimentary global dataset of nearshore slopes. They define this slope as the steepness between the Mean Sea Level, MSL, and the depth of closure, depth at which the bottom does not suffer significant morphological changes (see Figure 1.1). Although offshore wave parameters can be transformed to nearshore parameters using the nearshore slope, beach face slope is required for computing the elevation of wave run-up and total swash-excursion at the shoreline, which are used in most common wave run-up formulations. However, nearshore slopes are milder than beach face slopes. More importantly, the foreshore slope is estimated from GEBCO bathymetry, which has a very coarse resolution [11]. To address this limitation and complement the nearshore slope dataset, Vos et al, 2022 [11], created a sophisticated workflow and manage to obtain a beach face slope dataset for Australia.

However, their method has a few limitations. First of all, the beach face slope is obtained through optical satellite imagery, hence, their method is highly dependant on cloud-free satellite imagery, which is more often available in Australia and USA than in most parts of the world. Secondly, the application of optical satellite imagery also depends on tidal range, therefore, in areas with small tidal range, such as the Mediterranean, the method cannot be applied. Finally, another limitation of their method is the excessive uncertainty given by the usage of tidal models, which due to the low density of tidal measurements, extrapolation to nearby zones is necessary. Consequently, this method carries a significant level of uncertainty.

Space-borne Light Detection and Ranging (LiDAR) offers a remarkable opportunity to extract impor-

tant beach features at a global scale, including areas that are inaccessible to ground-based extraction. Therefore, with the launch of the Ice, Clouds and land Elevation Satellite 2 (ICESat-2) in September 2018 [14], a new methodology for extracting beach face slopes at a global level can be implemented, as shown in a recent case study in Texas [15]. The exceptional precision of the LiDAR instrument onboard of ICESat-2, along with its impressive spatial and temporal resolution, presents a remarkable opportunity to obtain precise elevation data for coastal regions. This data can be utilized to derive beach profiles and determine the corresponding beach face slope. With the exception of the case study done by Ma et al. [15], published by the end of this research (March 2023), and another case study in Saint Lawrence island [16], in which ICESat-2 was used for shore zone classification, to the best of my knowledge, any study has attempted to extract beach face slopes with ICESat-2 from different environments, study the relation between ICESat-2 direction and beach geometry, nor set the basis of a workflow for a beach face slope extraction at a global scale with ICESat-2.

1.1. Objective and research questions

Due to the importance of the beach face slope for modelling processes such as coastal flooding and the future possibility of increased occurrence of these events due to sea level rise (SLR), as determined by IPCC experts, where an increase between 0.35 to 0.60 m of SLR is expected for the low emission scenario (Representative Concentration Pathways, RCP2.6) [17], ICESat-2 is assessed as a possible tool for providing a global dataset of this parameter. The main focus of this research is to evaluate to what extent can beach face slopes be derived by ICESat-2. Furthermore, beach geometries and its orientation with respect to ICESat-2 passes are analyzed for understanding what are the requirements for extracting the parameter of interest. Then, a workflow is created as an attempt to upscale the beach face extraction procedure to a global level, what allows to assess to some extent the spatiotemporal resolution provided by ICESat-2 on coasts world-wide. Finally, the upscaling methodology opportunities and limitations are discussed. Hence, for pursuing such endeavor, the following main research question and sub-questions that transpired from the above presented scope of this report, must be answered:

To what extent can the beach face slope be derived from ICESat-2?

1. **How accurate can beach profiles, and the subsequent beach face slopes be extracted from ICESat-2 ATL03 data?**

To answer this sub-question, the validation process utilizes data that is as close as possible in both time and space to the ICESat-2 observations. The validation data includes beach profiles, if available, or, alternatively, only the extracted beach face slope.

2. **How dependant is the beach face slope extraction from ICESat-2 passes on beach geometries and the direction of its own fixed ground track?**

The ideal scenario for obtaining beach face slopes is when a profile measured by ICESat-2 is perpendicular to the shoreline (parallel the cross-shore profile, or transect). When the angle between this profile or pass increases, it is expected a lost in accuracy on the extracted cross-shore profile and the beach face slope. If the ideal angle between pass and transect is 0° , it is possible to determine up to what angle may the ICESat-2 measurements be able to accurately reflect the actual beach profile and beach face slope? Are there more requirements regarding beach geometry, its spatial configuration with respect to the satellite's orbit, or distance between ICESat-2 pass and transect to be taken into account?

For answering this, synthetic ICESat-2 ATL03 data created by following the most recent up to date Algorithm Theoretical Basis Document (ATBD) prepared by NASA's personnel of ICESat-2's mission [18], is used for providing insight about different beach geometries, direction of the passes and distance from ICESat-2 pass to the transect to project the geolocated photons.

- 3. What are the limitations regarding the ICESat-2 spatial and temporal resolution? To what extent can ATL03 data be used for monitoring beach face slopes**

Regarding the spatial and temporal resolution of ICESat-2, does it have enough passes, or the data has enough quality, over the same area for implementing a monitoring method?

- 4. What are the possibilities for upscaling a beach face slope extraction methodology from ICESat-2 ATL03 data?**

To what extent can the beach face slope extraction from ICESat-2 be upscaled? Is there any step where a human input must be given?

1.2. Structure of the report

After an introduction in Chapter 1 of the parameter of interest, the beach face slope, the motivation for this research, its objective and the research questions to be answered, a comprehensive definition and background information of said parameter, and the remote sensing device to use, ICESat-2, follow in Chapter 2. Chapter 3 presents all data used throughout the research, as well as the different areas where examples were done. The different methodologies employed, including a novel methodology for extracting beach face slopes from ICESat-2 data at a global level are presented in Chapter 4. In Chapter 5 the results and their consequent discussion are shown. Finally, the main conclusions and recommendations to take into account for further research can be found in Chapter 6.

2

Background

The purpose of this chapter is to provide the reader with essential background information on the research topic, as well as on ICESat-2 and the beach face slope. To achieve this goal, a comprehensive definition of the beach face slope is presented, along with an overview of the existing knowledge on its extraction at local, regional, and global levels (Subsection 2.1). Additionally, key information about ICESat-2 is provided, including details about the LiDAR instrument onboard (ATLAS), its orbital configuration, coverage, and sampling geometry (Subsection 2.3). By offering this information, readers unfamiliar with these topics can gain a solid basis to understand the research problem. Furthermore, by highlighting the importance of the beach face slope and its relation to a variety of coastal processes and its impact on coastal areas, the readers can grasp the potential implications of the research findings.

2.1. Beach face slope

The intertidal area or beach face (see Figure 1.1) is generally described as the area contained between the low tide mark and the uppermost reach of high-tide wave run-up [12]. Different definitions given by the literature include “the zone between the mean low water level and the seaward berm, which is equivalent to the upper limit of wave uprush at high tide”, [19], and “the seaward slope of the beach between the low tide line and the upper limit of wave swash”, [20].

However, even though the definitions seem to be straightforward, correctly defining the lower and upper boundary of the beach face is not trivial. Usually, the investigator demarcates the width of the beach face by using different common beach features such as back-beach erosional scarp, vegetation line, or single berms that reveals the most recent frequent high-water levels [21]. In the presence of multiple berms corresponding to run-up elevations with different return period, the most common is to measure up to the highest berm [12]. As it is possible to conclude from this, measuring the width of the beach face is not simple and bias can be introduced by the investigator.

The beach face slope, also referred in the literature as beach slope, intertidal slope or shoreface slope, is defined as the steepness of the beach face (see Figure 1.1). The beach face slope, $\tan \beta$, is a crucial parameter for the study of coastal morphology, as well for coastal engineers due to its influence on a plethora of coastal processes, such as the wave run-up —time-varying position of the upper edge of the water on the beach face—, which is typically parameterized by

$$\frac{R}{H_s} = c\xi_0, \quad (2.1)$$

where R is a vertical run-up statistic, H_s is the significant wave height, c is a constant, defined empirically, and ξ_0 the Iribarren number — surf similarity parameter that gives the ratio of the beach face slope, and the wave steepness— [22]. The latter given by

$$\xi_0 = \frac{\tan \beta}{(H_s/L_0)^{1/2}}, \quad (2.2)$$

with L_0 being the deep water wave length, dependant on the gravitational acceleration, g , and the wave period, T , through the equation: $L_0 = gT^2/2\pi$, and $\tan \beta$ the parameter of interest, the beach face slope [23]. Also, most of the formulas employed for determining the vertical swash —upward movement of water on the beach face following the breaking of waves— in the literature (2 for total swash, 3 for incident, and 8 for infragravity swash, 13 in total) (7 out of 13) depend directly or indirectly through the Iribarren parameter on the beach face slope. These two processes, the wave run-up, and the swash excursion parameterizations as component of the wave run-up, are usually included in coastal hazards and vulnerability assessment framework, being critical when studying or managing coastal hazards [24].

Furthermore, this parameter is a useful proxy for surf-zone hydrodynamics —such as wave breaker type given by the Iribarren parameter, Equation 2.2, that allows to classify breaking waves: surging $\xi_0 > 5$, collapsing $0.3 < \xi_0 < 5$, plunging $0.5 < \xi_0 < 5$, and spilling $\xi_0 < 0.5$ — in the absence of costly surf-zone bathymetric surveys, and can also provide insights regarding swimmer safety, as well as wave set-up across the surf-zone. The beach face slope is also closely linked to the grain size of a beach, gravel beaches tend to have the largest slope values ($\tan \beta > 0.1$) and beaches with finer sediments like sand or mud tend to have a gentler slope ($\tan \beta 0.01 - 0.1$), as shown in Figure 2.1 [25, 12, 26, 27]. Therefore, the influence on these coastal processes, its relation with the tourist perception of the beach, coastal property assessments, species abundance, as well as the demarcation of legal boundaries [28, 29, 30, 21] makes of a world wide beach-face slope dataset, and its monitoring an increasing necessity, especially in areas of difficult access or lack of resources.

However, as explained, the beach face slope is the steepness of the foreshore, the most seaward area of the beach. Hence, it is under continuous interaction with waves, tides and currents, making this section highly variable, not only in the long-term, but seasonably and in even shorter periods of time such as days or even hours. These changes on the morphoplogy of a beach, generated by the different morphodynamic regimes that the beach might be subjected to —beach states— have been accounted for and a classification of six beach states was made by Wright and Short (1984) [31], sorted from the highest state, dissipative, to the lowest state, reflective.

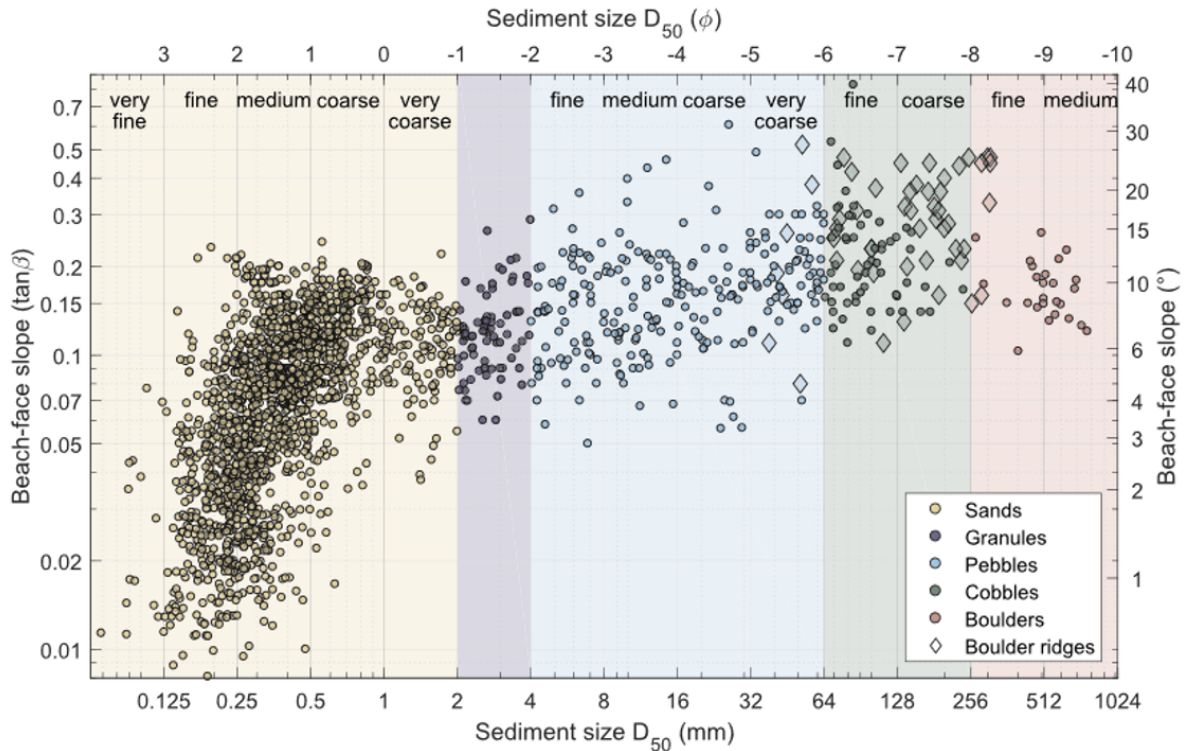


Figure 2.1: Log-log plot of beach face slope versus median grain size. Figure from Bujan et al. [12].

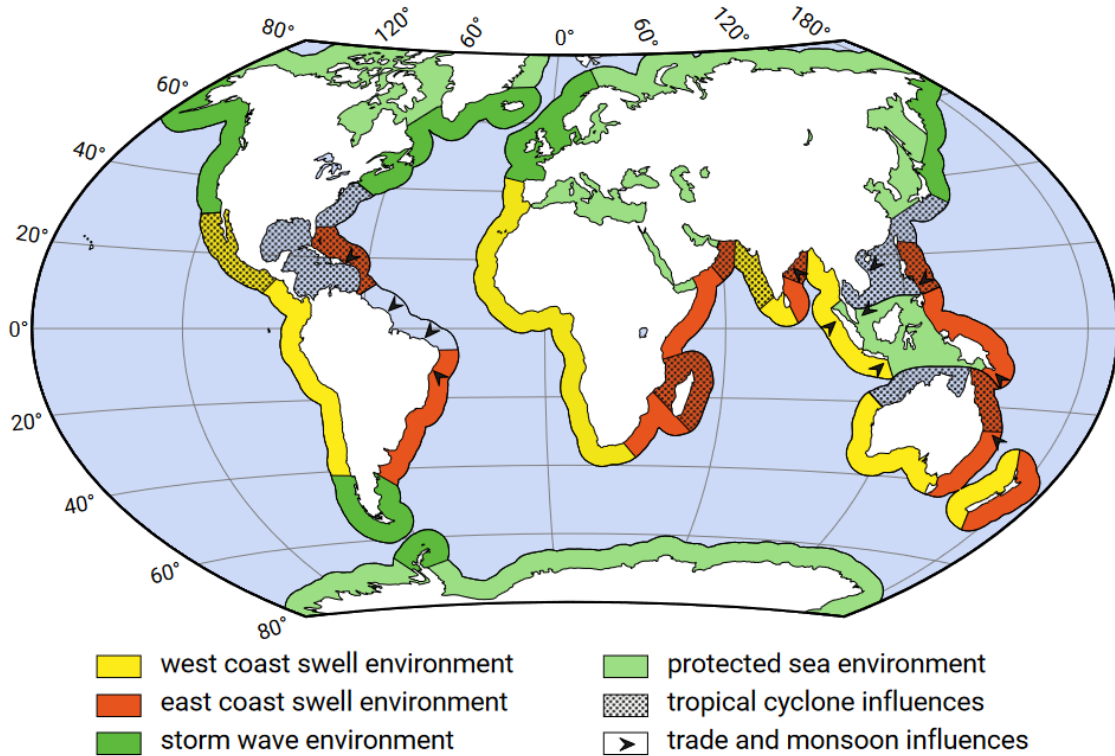


Figure 2.2: World-wide distribution of environments according to J.L Davies and Clayton, 1980 [32]. Adapted by Judith Bosboom and Marcel J.F. Stive, 2023 [27].

The cross-shore profile, which is also referred to as the beach profile, represents the elevations of the different sections of a beach from the backshore to the shoreline; it is possible to roughly relate the profiles of reflective and dissipative beaches to "summer" and "winter" profiles respectively (see Figure 2.3). The reflective beaches are relatively steep with a slope, $0.1 < \tan \beta < 0.2$, and Iribarren parameter, $\xi_0 > 2$. On the other hand, to the other end of the classification, with the four intermediate beach states being characterized by the corresponding intermediate features of both extreme states, the dissipative beaches are defined by beach face slopes of approximately 0.01 and Iribarren numbers of approximately 0.2 – 0.3. To sum up, named characteristics lead to the reflective beaches to be less dynamic and be found in swell and monsoon climates (see Figure 2.2) while the dissipative beaches result in a highly dynamic beach profile and often found in storm wave climates [27]. This fact might have as a consequence that the latest type of beach, as well as the intermediate beach states with similar characteristics, requires a more continuous monitoring than reflective beaches.

2.2. Extracting beach face slopes: from manual techniques to elaborated workflows using remote sensing devices

The beach profile is a crucial feature of a beach, as it not only allows for the calculation of the beach face slope, but also provides information about the wave climate that the beach is subjected to, as well as whether it is a winter or summer profile and a dissipative or reflective beach. By studying the beach profile, researchers can gain insight into the beach morphology and how it changes over time due to natural processes, such as erosion and sedimentation, and anthropogenic activities. This information is important for coastal management and planning, as well as for understanding the potential impacts of climate change and sea level rise on coastal areas.

There is a wide range of techniques for extracting beach face slopes (see Chapter 1). For this extraction, the elevations of a transect perpendicular to the shoreline need to be measured. In order to do this, the

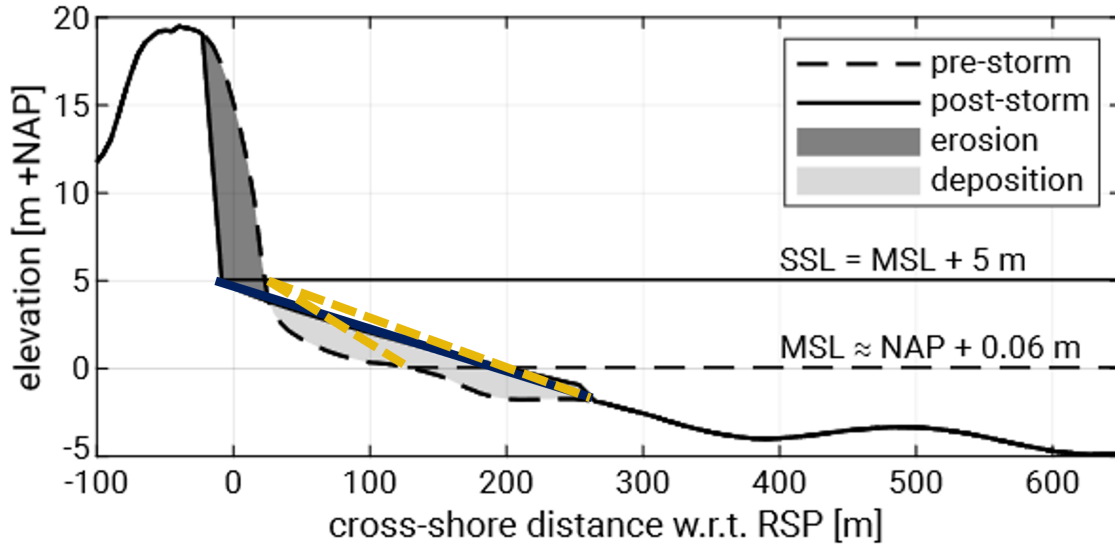


Figure 2.3: Beach profiles before (dashed line) and after a storm (black solid line), these profiles can be roughly compared to a summer and a winter profile, or a reflective and a dissipative beach, respectively. The colored lines show different beach face slope possibilities for both profiles, in yellow for the pre-storm or summer profile, and in dark blue for the post-storm or winter profile. Example case of a beach on Netherlands, adapted from Bosboom and Stive [27].

manual methodologies include measuring a simple cross-shore profile with theodolites, Abney levels, or dumpey levels. Newer and faster methodologies scan the beach and extract from the obtained point cloud the cross-shore profile, this is the case for laser scanners, unmanned aerial vehicle, RTK-GPS, measurements, or airborne LiDAR [12].

Despite the advantages of these modern measurement techniques, neither the manual nor the newer approaches can be easily upscaled. Manual methods can be challenging, dangerous, and time-consuming, while the cost of upscaling the newer techniques to measure larger areas can become too expensive. In order to solve this limitation, Vos et al., 2022 [11], created a workflow, but its dependency on optical satellite imagery and tides, what makes it invalid in areas such as the Mediterranean, or other areas with limited tidal range, and uncertainty given by tidal models makes it not valid globally. On the other hand, the methodology proposed by Ma et al., 2023 [15] tackles only sandy beaches at a regional scale using ICESat-2. The opportunities and limitations by the proposed methods are discussed in Chapter 5 in the discussion subsection.

Even though the beach profile seems straight forward to measure, coasts are continuously changing, and therefore beach profiles has seasonal modifications, or react to different wave regimes, leading to different beach face slopes. In addition, ICESat-2 data is subjected to the tidal level at the moment of the pass, and therefore, it can lead to different beach face slopes depending on which point of the profile is selected as the start of the ICESat-2 beach profile. In Figure 2.3 it is possible to see how this would affect the beach face slope, while the winter profile, blue, is quite constant from the assumed lowest sea level to the dune foot, and the beach face slope extracted from ICESat-2 at any tidal level of said profile might lead to similar values, the summer profile, yellow, has more variability cross-shore and two different beach face slopes can be obtained. Therefore, it is important to bear in mind that when comparing beach face slopes extracted from ICESat-2 with those takes as truth, the resulting beach face slope might be different, but it does not mean that ICESat-2 has not correctly captured the beach profile and the subsequent beach face slope. Furthermore, ICESat-2 is also cloud dependant so it has to be accounted for when assessing LiDAR-based satellites as monitoring tools.

2.3. ICESat-2

For the purpose of this research (stated above), ICESat-2, what stands for Ice, Clouds, and land Elevation Satellite 2, is employed. ICESat-2 is the successor of ICESat, which was the first spaceborne laser altimetry mission for Earth science, and collected measurements from 2003 to 2009 [14]. The state of the art spaceborne laser altimeters are onboard of ICESat-2, a photon counting LiDAR (PCL), and, a full-waveform, multibeam laser altimeter, onboard of GEDI (Global Ecosystem Dynamics Investigation). Both of them collect elevations at a global scale precisely. However, ICESat-2 is used because it outperforms GEDI when it comes to terrain height retrieval, with ICESat-2 giving more precise geolocated photons, and having a shorter along-track spacing than GEDI, this is, a higher measuring frequency [33].

A close analysis of the performance of ICESat was made and it is well summarised by Markus, T. 2017 [14], In this document they comment on what could be added, changed, or improved for the next space-borne Light Detection And Ranging (LiDAR), ICESat-2, and defined the science objectives for ICESat-2, which are paraphrased as follows:

- *Quantify polar ice-sheet contributions to current and recent sea-level change and the linkages to climate conditions;*
- *Quantify regional signatures of ice-sheet changes to assess mechanisms driving those changes and improve predictive ice sheet models; this includes quantifying the regional evolution of ice sheet change, such as how changes at outlet glacier termini propagate inward;*
- *Estimate sea-ice thickness to examine ice/ocean/atmosphere exchanges of energy, mass and moisture;*
- *Measure vegetation canopy height as a basis for estimating large-scale biomass and biomass change.*

The last item of the list above was the objective that determined that ICESat-2 should collect data over the mid- and lower-latitudes, and that ICESat-2 should utilize an operational off-nadir pointing capability for generating optimized (non-repeat) collection of measurements for canopy heights that has contributed to the generation of a global carbon inventory assessment. However, this decision has allowed other science fields to have precise measurements and create methodologies and techniques for assessing different processes and systems. Therefore, it is due to this fact that ICESat-2 is assessed here not only for how accurate beach face slopes can be extracted but to analyse to what extent this parameter can be monitored. Its main features are summarised in Table 2.1

Table 2.1: Major features of ATLAS and ATL03 data product

Launch date	September 15, 2018
Nominal altitude	496km
Orbit	Non-Sun-synchronous
Inclination angle	92°
Coverage	88°N – 88°S
Number of Reference Ground Tracks	1387
Laser wavelength	532 nm
Pulse repetition rate	10 kHz (0.7m along track spacing)
Number of beams	6 (3 pairs)
Footprint diameter	< 17.4m
Beam energy ratio	4:1
$\sigma_{\text{along-track, across-track}}$	5m
σ_z	0.17m

2.3.1. ATLAS

ICESat-2 was launched on September 15th, 2018, with a LiDAR instrument on-board, the so-called ATLAS, what stands for Advanced Topographic Laser Altimeter System. A LiDAR is an active remote sensing device that is able to transmit energy at a certain wavelength and collect the remaining energy reflected by different features on the Earth's surface. Besides, by measuring the time lapse between

the outgoing pulse of energy and the detection of the reflected (backscattered) energy pulse by the sensor, Δt , it is possible to convert the measured time interval to distance d , by applying the equation $d = c\Delta t/2$, where c is the speed of light and the factor $1/2$ is used because the energy has to travel back and forth [34, 35].

ATLAS is a photon-counting LiDAR (or PCL), this means that in contrast to its predecessor, ICESat, and GEDI, which are full-waveform LiDARs, and therefore, the full waveform sensor captures the entire time profiles of the reflected laser energy, the ICESat-2 detectors, photomultiplier tubes (PMTs), record the arrival time of individual photons and then these are geolocated [33, 14]. Therefore, this instrument is the most important part of ICESat-2. It can be roughly separated in three principle systems, the transmitter, which generates the laser pulses, the receiver where photons are detected and timed, and finally, for determining the laser pointing direction, the alignment monitoring and control system, which includes the laser reference system. The altimeter operates by making use of a green laser with a wavelength of 532 nm. It emits 10,000 laser pulses per second (pulse repetition rate of 10 kHz), which leads to a relative small along-track interval of 70 cm, and each pulse contains 20 trillion photons, from which only around 12 can be recorded back at the satellite by the sensor [36, 37].

The atmosphere's particles constantly reflect the sun's light, creating a false surface that causes certain photons from the pulse to return to the device from high up in the atmosphere. However, the ATLAS system only expects photons to return within a specific time range (or height range), so those with a lower time of flight are discarded. Nonetheless, the sun's effect on the atmosphere is also present near the actual surface, so any photon reflected within the desired time interval, regardless of its origin, is considered a photon event and it is time tagged accordingly.

To distinguish between background noise and signal photon events, a three-step procedure is employed. Firstly, onboard algorithms are utilized to reduce data volume by generating histograms and identifying the histogram bins that are most likely to contain the desired surface. Next, a second algorithm is used to classify the downlinked photon event as either likely signal or background, once again, with the purpose of reducing data volume. Finally, surface-specific higher-level data products are created to generate accurate ellipsoidal heights based on the identified signal photon events. These precise, surface-specific heights are integral in achieving the ultimate objectives of the ICESat-2 mission [18]. Further explanations on how ICESat-2 data, and specifically ATL03 data is extracted from ATLAS measurements is given in Chapter 3.

2.3.2. Orbit, coverage, and sampling geometry

The instrument presented in section 2.3.1 flies on-board of ICESat-2 at a nominal orbital altitude of approximately 492 km, generating daily grids similar to the example shown in Figure 2.5, and within this grid representing the ground track of ICESat-2, measurements with 6 beams following the sampling geometry of Figure 2.4 are taken. It is possible to observe in this figure, that ATLAS splits the laser in 3 pairs of beams separated approximately by 3.3 km and with a separation of 90 m within each pair of beams.

Each pair consists of a strong and a weak beam with a transmit energy ratio 4:1. Each beam has a footprint from approximately 11 m [38], possibly up to 17.4 m [36], with an along-track sampling interval of 70 cm. These difference on signal returns for the strong and weak beams might give a disadvantage for the weak beam when extracting ground elevation. Nevertheless, as concluded by Zhu et al., 2020 [39], both beams perform well for extracting ground elevations, and therefore, no distinction is done when working with strong or weak beams.

Regarding the spatial coverage, due to its large inclination angle, ICESat-2 covers most parts of the globe, generating a grid that is denser on high latitudes than mid and low latitudes. Therefore, for accounting for this effect, produced by ICESat-2's inclination angle, the named off-nadir pointing capability (see subsection 2.3) is employed. It is important to bear in mind this off-nadir pointing when assessing ICESat-2 as a monitoring tool. Another physical processes that add noise, uncertainty or make ICESat-2 passes not useful are clouds and sunlight [38]. For a global monitoring these topics must be

addressed, because the spatiotemporal distribution of these processes, sunlight and its interaction with the atmosphere, as well as cloud coverage, are highly variable throughout the globe.

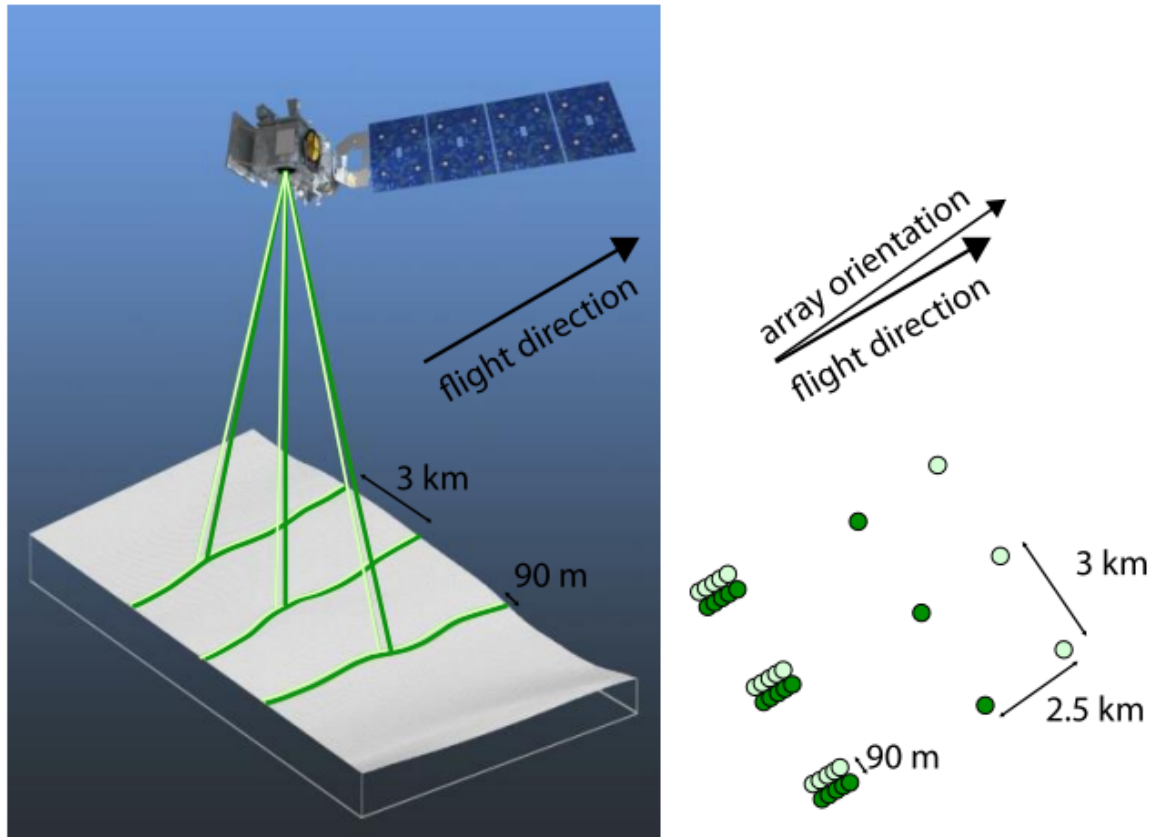


Figure 2.4: ATLAS idealized beam and footprint pattern [18]

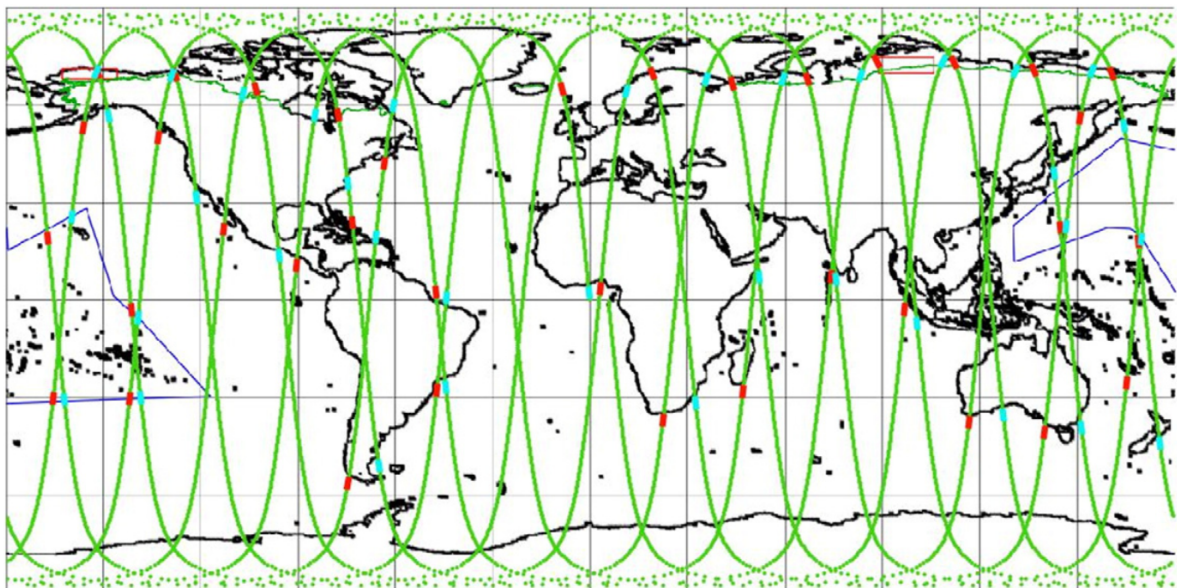


Figure 2.5: Illustration of one day of ICESat-2 orbits. The blue and red orbit sections indicate where the pointing transitions from polar "repeat-track mode" to "land/vegetation", respectively. The transition regions have been defined for all 1387 ground tracks and can be updated on orbit [14].

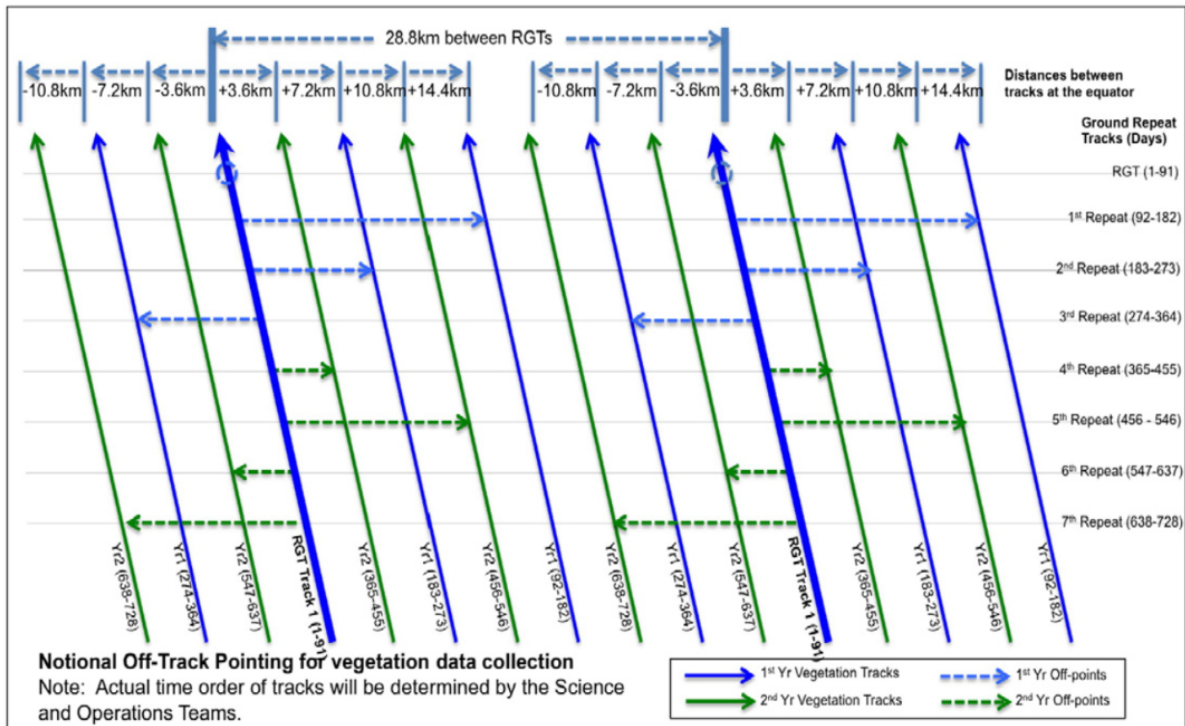


Figure 2.6: Ground track pattern at the equator during the first two years. The bold blue lines show the first passes for this period. These are the nominal 91-day repeat passes. At the equator, the gap between Reference Ground Tracks (RGTs) is 28.8 km. The passes were shifted 91 days later by 14.4 km to the right, reducing the gap by half. This halving of the gap was repeated over two years, i.e. 8 times. The combination of ascending and descending orbits results in a pass spacing of less than 2 km. The maximum off-nadir angle is about 1.5 degrees [14].

3

Data and Study Areas

This chapter provides detailed information of the various types of data used throughout the report, including different validation datasets, such as Terrain Laser Scanner (TLS) and RTK-GPS measurements, optical satellite imagery, synthetic ICESat-2 ATL03 data, JARKUS, and the system of transects. Each of these items is discussed in its own subsection, and the information presented is essential for understanding the rest of the report. Furthermore, the study areas selected for analysis are presented in a corresponding manner.

3.1. ICESat-2 ATL03 data

The most important data product that is used in this research project is ICESat-2 Global Geolocated Photon Data, a Level 2A data product identified henceforth as ATL03 data, which provides latitude, longitude and height over the ellipsoid of the individual photons detected by ATLAS. This data product, as well as the rest of the data products derived from the tagged photons by ICESat-2 (see Figure 3.1) are provided in a variety of formats such as the Hierarchical Data Format 5 (HDF-5). These are publicly available in the National Snow and Ice Data Center (NSIDC - <https://nsidc.org/data/icesat-2>).

Figure 3.1 shows that ATL03 combines the data products of the Precision Orbit Determination (POD), the Precision Pointing Determination (PPD) and ATL02 to produce a Level 2 product containing geolocated ellipsoidal heights for each time tagged photon event downlinked from ATLAS. These heights are corrected for several geophysical phenomena (e.g., atmospheric refraction, tides) and are classified either as likely signal photon events or likely background photon events.

The ATL03 product is the step between the lower level, instrumentation-specific products (ATL0102) and the higher-level, surface-specific, science-centric products (ATL06 and above). ATL03 classifies each photon event as either "likely-signal-photon event" or a "background-photon event" and provides a confidence assessment on these classifications. This classification is made by generating histograms of the number of photon events as a function of height and calculating the signal-to-noise ratio (SNR) of each histogram bin. The photon events in bins with a SNR greater than a threshold are classified as signal, while other photon events are classified as background [18].

Table 2.1 contains the major features of ICESat-2 orbit, altimeter on-board, as well as of the data product of interest for this report, ATL03. Most of the features listed here are commented on Chapter 2, with the exception of ATL03 data. With a maximum of $17.4m$ of footprint diameter, and a sampling interval of $0.7m$ ATLAS measures ground elevation, then, an algorithm is applied to the resulting measured photons. This algorithm is out of scope in this research, and if needed, it can be consulted in [18, Neumann et al., 2021]. Once the algorithm has filtered the noise and classified photons, as well as corrected measurements for different geophysical processes, ATL03 data is obtained. This dataset contains geolocated photons with an along-track and across-track accuracy of $5m$ and a vertical accuracy of $17cm$, providing enough data and accuracy to be the most optimal device available for extracting

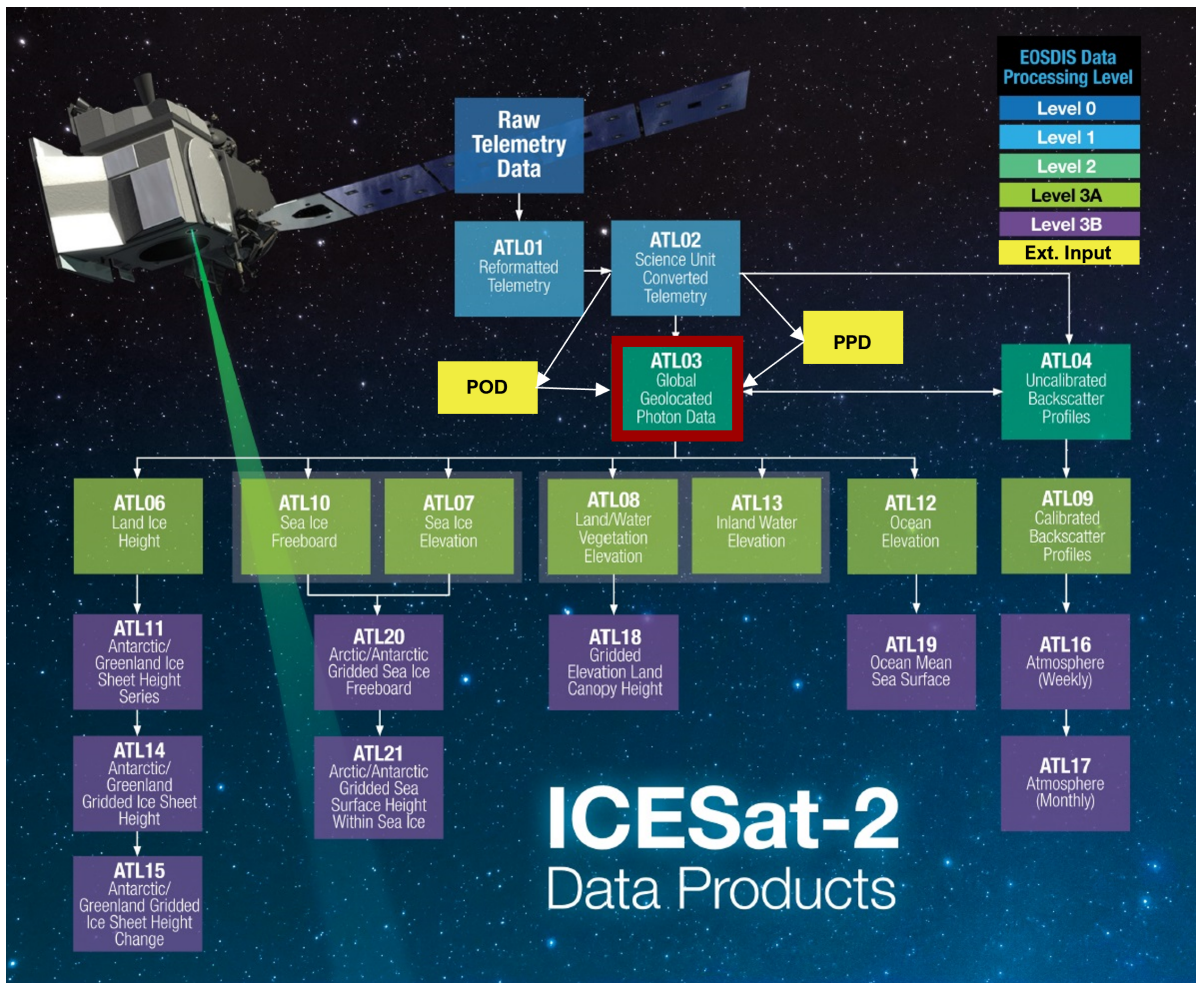


Figure 3.1: This figure shows the flow of ICESat-2 data from lowest to highest level of processing, with the data to use in this report highlighted with a red box. The color indicates data product levels, while the text reports data product number and short name. All products (ATLxx) are generated by the Science Investigator-led Processing System (SIPS), and distributed by the National Snow and Ice Data Center (NSIDC). Adapted from NSIDC website, visited on 10-03-2022.

features on the centimeter and meter levels. Furthermore, both beams, strong and weak, perform well for extracting ground surface elevations [39]. Consequently, ICESat-2 product ATL03 has been selected for extracting beach face slopes in this report.

Figure 3.2 shows three example passes of ICESat-2 ATL03 data collected over different areas, from left to right: Gran Canaria (Spain), Peniche (Portugal), and Ameland (Netherlands). Then, one of the beams in each location (highlighted in a red rectangle) is selected for extracting the corresponding profiles. The point clouds shown in the middle panels correspond to each extracted profile. In the point cloud it is possible to see the geolocated photons colored based on its quality, with the quality classification being: 'Noise', 'Buffer', 'Low', 'Medium', and 'High', corresponding in the profile to black, red, yellow, blue, and green. After filtering based on this classification and keeping only high quality photons, the profiles shown in the bottom panels are obtained.

These profiles have been selected in order to help the reader to familiarize with ICESat-2 profile and see the different features that they might provide, as well as its variability in water and land, as well as in the transition between both. As it is possible to observe, not only the surface elevation visually seems to be measured accurately, but it is possible to discern between land and ocean, and even glimpse the area that interacts between both of them, the beach face. However, even though in these cases the full profile is extracted over the area, there are cases where almost no 'High' quality data is obtained.

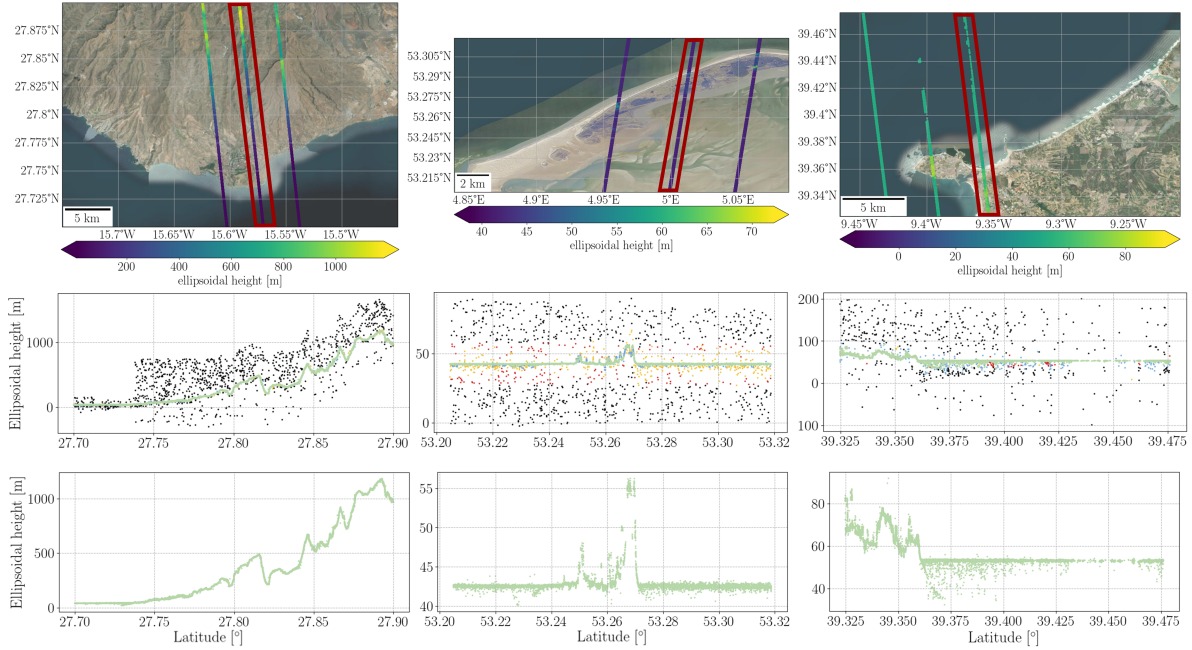


Figure 3.2: ICESat-2 example passes over different areas, from left to right: Gran Canaria (Spain), Peniche (Portugal), and Vlieland (Netherlands), are shown in the upper panels. Under each of them, the corresponding point cloud obtained for each pass is presented, with the points colored based on the quality of the data: black is 'noise', red is 'buffer', orange is 'low', blue is 'medium', and finally green is 'high'. The latter one is presented alone in the bottom panels.

The profile has gaps due to clouds or solar effect, and the amount of photons classified as 'Noise' is higher than other cases. For extracting the beach face slope, given that it is a beach feature that is highly variable depending on which elevation points are taken, only 'High' quality photons are selected to ensure the most accurate profile possible.

Another detail that must be address that can be seen in Figure 3.2, is how photons interact with the ocean surface. On the bottom panels, in which the photons has been filtered and only the high quality ones are shown, it is possible to observe that while in the case of Gran Canaria, Spain, the photons are concentrated on the surface, for the case of Ameland, Netherlands, there are 2 distinct water surfaces, the one to the right corresponds to the ocean, and waves can be observed, while the left section is inside the tidal basin. In the latter case and in Peniche, Portugal, it is possible to see how the green laser penetrates into the water, leading to a more spread point cloud around the actual surface, and it should be taken into account when it comes to automatizing beach face slope extraction based on the estimation of mean sea level (MSL) and/or wave height based on point clouds of this areas.

3.2. CoastScan dataset

The CoastScan is a research project of Delft University of Technology to monitor the variety of processes that happen on the coast, such as erosion, sediment transport or effects of bulldozer works. Near-continuous terrestrial laser scanners (TLS) were positioned in three different locations: Kijkduin and Noordwijk in Netherlands, and Oostende in Belgium. TLS were fixed at the said locations for months to years, scanning the beach surface hourly [40]. Kijkduin and Oostende cannot be used because their working time was previous to the launching of ICESat-2. However, the TLS of Noordwijk measured the area a few minutes before a pass of ICESat-2, providing an excellent dataset for comparing and validating how well ICESat-2 can be used for extracting beach features, such as beach profile and beach face slope.

This technology is ideal for detailed DEM (Digital Elevation Model) mapping of beach features because of several key factors. Firstly, TLSs are non-invasive and do not cause any disturbance to the beach ecosystem. Secondly, TLSs can be used to measure the same area repeatedly, which allows for the

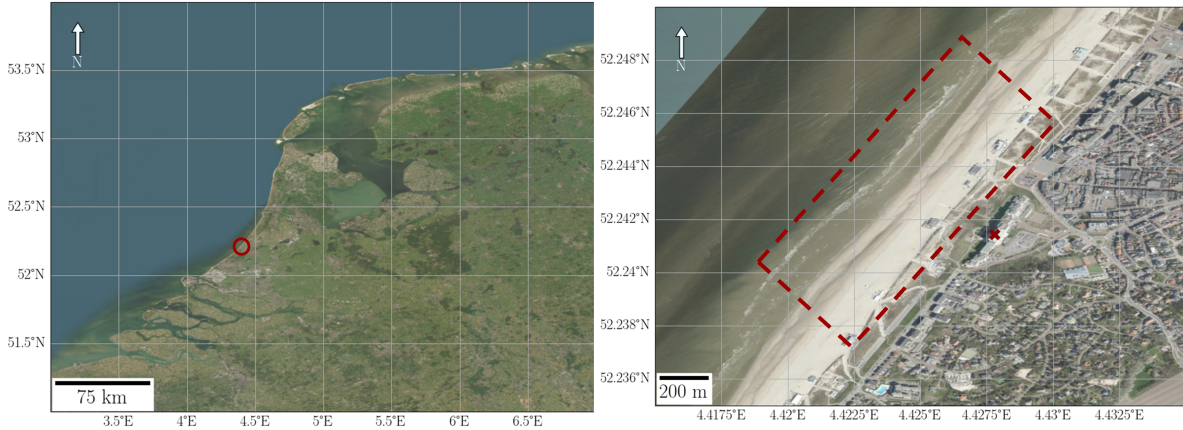


Figure 3.3: Location map of the Terrain Laser Scanner, TLS, in Noordwijk, Netherlands. The left map shows where the beach is located in Netherlands, and the right map shows the exact position of the TLS, as well as a bird's eye of the scanned beach.

identification of subtle changes over time. Additionally, TLSs are independent of illumination and can therefore be used to collect data during any time of day or night, and in any weather conditions. Finally, TLSs provide high-resolution, three-dimensional point clouds, making it possible to accurately map beach features ranging from small-scale topographic changes to larger-scale morphological changes that occur over hundreds of meters [41]. The aforementioned factors have enabled the comparison of this dataset with ATL03 data from ICESat-2. While ATL03 provides a thin line of measurements, the point cloud generated by the TLS captures a larger area containing the ICESat-2 measurements. Additionally, because TLSs are active sensors, it scanned the beach at 20:00 pm, at night, resulting in the extraction of a point cloud of the beach only 12 minutes before the ICESat-2 pass (see Table 3.1). Finally, due to the high accuracy point cloud extraction, it is possible to take this dataset as ground truth, bearing always in mind that the generated point clouds can contain errors and might deviate from the actual beach.

Figure 3.3 includes two maps that depict the location of the TLS. The map on the left highlights the TLS location in relation to the Netherlands (enclosed by a red circle), while the map on the right shows the scanned area in relation to the beach, and the exact position of the TLS, indicated by a red cross. The TLS is a RieglVZ-2000 laser scanner mounted on the balcony of Grand Hotel Huis ter Duin in Noordwijk, The Netherlands (see Figure 3.5). It covers approximately 1km in the alongshore direction and a varying width and height dependant on tides wave heights, weather conditions and human activities [42], in the case of the TLS of interest, the range on the sandy beach varies between 150 and 500 m, and its accuracy varies with the distance to the laser scanner, being approximately $\sigma = 0.008\text{m}$ at 150m range [41].

Table 3.1: This table lists the specific date and time when the validation dataset from the TLS and the ICESat-2 passes to validate were collected.

Location	CoastScan		ICESat-2		Time difference
	Date	Time	Date	Time	
Noordwijk	2021-03-30	20:01	2021-03-30	20:13	12 min

Figure 3.4 shows the point cloud obtained with the TLS, and overlapping this, it is possible to see the passes measured by ICESat-2. The coordinates are in meters, in the dutch coordinate reference system, Rijksdriehoeks-coordinates, RD-coordinates, and the elevation is given with respect to the dutch vertical datum, Normaal Amsterdams Peil, NAP, this is, with respect to the sea level. In the left panel it is possible to observe the whole ICESat-2 pass, while from the right panel, only the reprojected geolocated photons over the point cloud have been kept (for more detailed information, see the section regarding the ICESat-2 validation with the CoastScan data in Chapter 4). Here it is possible to see that some

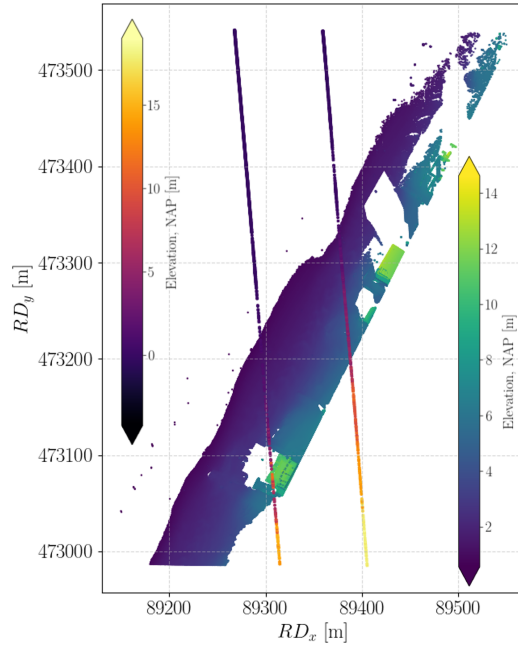


Figure 3.4: ICESat-2 passes overlapping CoastScan point cloud on Noordwijk, see Figure 3.3. Coordinates in the Dutch coordinate system, RD-coordinates, and the height given with respect to the the dutch vertical datum, NAP. The left map contains all the geolocated photons over the area, while the right map only geolocated photons overlapping the TLS point cloud are kept. Two different colormaps are employed for distinguishing between datasets, left colorbar for ICESat-2 passes and right colorbar for TLS scan.

sections of the resulting extracted profiles should be removed for a correct comparison of beach profiles, such as the beach house overlapping the left pass.

3.3. RTK-GPS dataset

Even though CoastScan provides a good case for validating ICESat-2 ATL03 data for extracting beach features, it consists only of one date of measurement with 2 beams/passes and therefore 2 profiles are available for validating. Therefore, for further validation, RTK-GPS measurements were done in the beach of Noordwijk, Netherlands, 2 days after an ICESat-2 pass. However, at the time of writing this report, the data has not being released yet. Nevertheless, the measured data was taken following a previous ICESat-2 pass, and therefore, it will be compared to this (see Table 3.2).

Real-Time kinematics (RTK) positioning data is essential in topographic surveys that require high precision. RTK involves transmitting corrected GPS signals in real-time from a base receiver located at a known position to one or more rover receivers. Thanks to recent advancements in RTK-based GPS systems, compensating for atmospheric delay, orbital errors, and other variables in GPS geometry can result in achieving a horizontal accuracy of 1 cm [43]. In this case, RTK-GPS measurements were done with the sensor from Leica Geosystems, GS18i (see Figure 3.5), which has the usual functionalities of a modern GNSS receiver, has an integrated photogrammetric camera, and compensates for tilting of the pole thanks to its internal IMU (Inertial Measuring Unit). It has a high 3D precision (with RMSE values of 12, 10, and 18 mm for the x, y, and z components) which is reduced when using the photogrammetric option [44]. Because of the high precision of this device, and the interest of only the beach profile and not of the 3D surveying of the beach of interest, only the GNSS option of the Leica GS18i was used, for extracting the most precise profile possible.

Table 3.2 shows the time difference between ICESat-2 passes and measured beach profile using RTK-GPS. This time interval is of more than 3 years, and not only this is a relatively large period of time between measurements, but the profiles correspond to different seasons and therefore they might have been subjected to different wave regimes. Therefore, the passes are not expected to exactly match the measured elevations and beach profiles, but the beach face slopes to have realistic and similar values as



Figure 3.5: Validation devices: TLS RiegIVZ-2000 (left) and RTK-GPS Leica GS18i (right).

well as a visual matching on some sections of the profiles.

Table 3.2: This table lists the specific date and time when the validation dataset of RTK-GPS measurements and the ICESat-2 passes to validate were collected.

	ICESAT-2	RTK-GPS	
Location	Date	Date	Time difference
Noordwijk	2019-11-19	2023-02-13	~3.25 yrs

Figure 3.6 shows the location of the beach where the RTK-GPS measurements were done, as well as the measurements themselves and the ICESat-2 ATL03 data over the area. This beach is found 3 km south to the section of the beach presented on Figure 3.3. This example shows the effect of clouds or the sun on the photons. Applying the algorithm that classifies and filters the photons based on quality has led to the gaps shown here. Thankfully, the profile over the beach is there. This figure shows as well the positions of the RTK-GPS measurements taken. First, the path of the beams were followed and measured with RTK-GPS in order to capture the same profile as the beams. Then, in order to extract and compare the beach face slopes between ICESat-2 and RTK-GPS, two beach profiles approximately intersecting in the intertidal area of each one of the measured passes. These beach profiles are used as lines for projecting the geolocated photons onto them and extract the beach face slope (see Chapter 4).

3.4. Optical imagery: Water Occurrence Probability layer

Further validation is necessary to assess how well ICESat-2 performs in extracting parameters of interest in coastal areas. Two validation datasets have been used so far, but a more comprehensive methodology is needed to compare profiles and validate ICESat-2 ATL03 data using a larger number of passes. To avoid the tedious task of manual extraction, the process is automated (as described in Chapter 3). However, one of the challenges of this automation is accurately identifying the upper and lower boundaries of the intertidal area.

Optical imagery has been used for computing the water occurrence probability at a global level for different water bodies [45, 46]. The water occurrence probability layer gives the probability of a pixel of being water or land. These layers are extracted using imagery from LandSat satellites, which has a resolution of 30 meters, and therefore, the resolution is too coarse for accurately extracting the beach face slopes. However, Sentinel-2 offers a possibility for creating this layer with imagery of a finer resolution, 10 m.

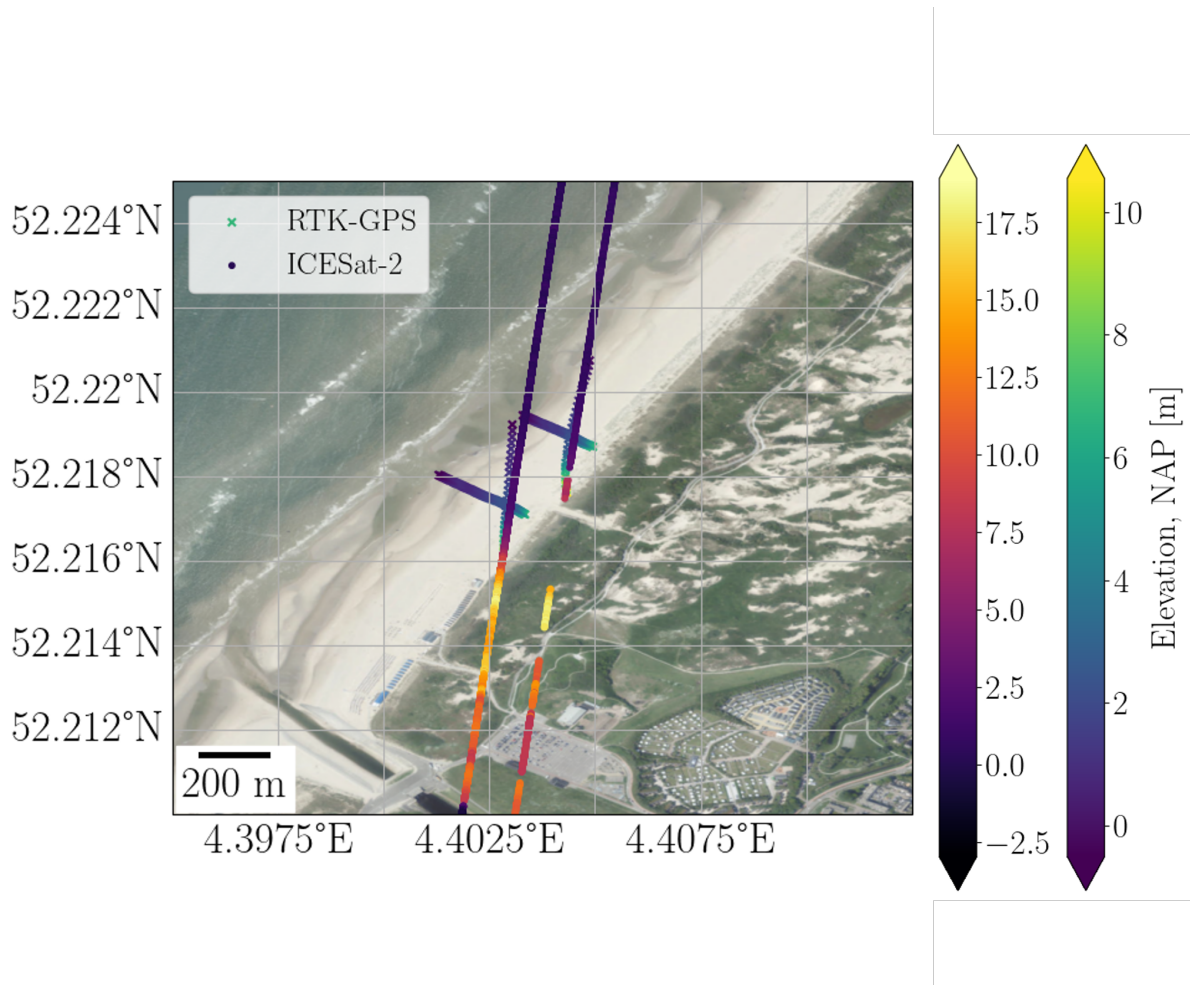


Figure 3.6: Exact location of the measurements done for validating ICESat-2, the beach on this figure is approximately 3 km south to the area shown in Figure 3.3. Measurements done with RTK-GPS and ICESat-2 ATL03 data are also shown here.

The creation of this layer was done in a pilot study previous to this report using Google Earth Engine, and the process for computing this layer is summarised as follows:

1. **Pre-processing and filtering:** the images over the area with a cloud percentage smaller than a certain value (15 %) are selected, and the clouds on the resultant images are masked.
2. **Computing NDWI:** the Normalized Difference Water Index (NDWI), one of the most common spectral indexes used for water body delineation is computed. It uses the green and near infra-red bands. This index is used in order to widen the difference between water and background and allow an easier threshold selection, this can widen the gap between classes and the threshold sensitivity is minimized [47].
3. **OTSU:** Nobuyuki Otsu [48] created a non-parametric and unsupervised method of automatic threshold selection for a picture segmentation. For the case of study, OTSU finds an optimal threshold that maximizes the separation between the NDWI values. This threshold is computed over the median of NDWI values of the image collection, and then, the threshold is applied over each image, generating a binary classification.
4. **Water occurrence probability:** The resultant composite for each image consists on zeros, if the pixel is classified as land, and ones, if it is classified as water. If the mean is computed, the probability of a pixel being 'water' or 'land' is found. When computing the mean of any data, firstly, all the you values are added, then, they are divided by the number of measurements. Hence, in this case, the values of each pixel (0 or 1) are added and later divided by the number of images, resulting in the probability of it being 0 or 1 (see Figure 3.7).

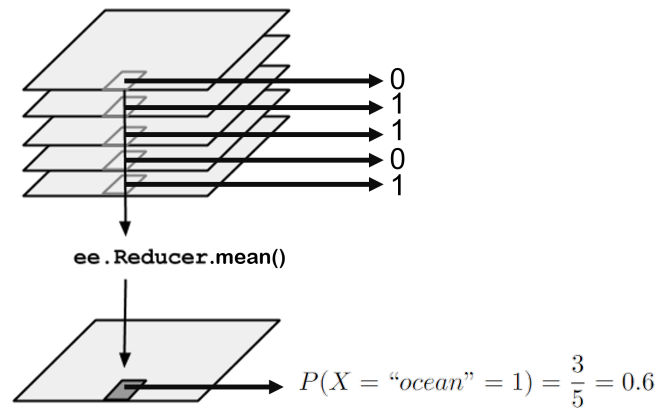


Figure 3.7: This figure shows how a reducer aggregates information along a given dimension. In this case the mean of all images is being shown. As a result of 5 binary layers with zeros and ones, the final result can be read as the probability of the given pixel of being ocean/water.

From this pilot study a few examples of the final Water Occurrence Probability layer (WOP) are shown in Figure 3.8, the layer goes from 0 to 1 (not including 0, the land has been masked), with 0 being land and 1 being water. The examples of panel a, b, and c, belong to the northern islands of Netherlands, panels e and h are coastal areas on Gran Canaria, Spain, panel d is in Guerrero, México, f is in Coquimbo, Chile, and panel g is in Zavala, Mozambique (see approximate location in world map in the center of the figure). As it is possible to see, this layer is able to capture tidal inlets (panel a), the intertidal areas (panel c), mouth rivers (panel d), and even small features such as groynes (panel b).

However, it fails to correctly capture the intertidal areas in different areas such as the ones on panels e, f, and h. In areas close to cities, where the reflectance of buildings (e) add noise to OTSU’s histogram, as well as in dune areas (h), and in areas with a wide variety of reflectance values from which the OTSU’s algorithm is not able to find a correct threshold. For this reason, the WOP layer is only used for automating the demarcation of the intertidal area on the synthetic profiles. In Figure 3.8 it is possible to observe how the WOP layer visually seems to follow the bathymetry, and even if it is not fully correct, for this methodology is not important how correct the intertidal area is defined, but how the profile of the passes translate to the transect and how it affects the subsequent beach face slope extraction.

3.5. Synthetic ICESat-2 ATL03 data

Due to the fixed orbit of ICESat-2 and its relatively low repetition orbit, synthetic data is created for providing information about the behaviour of the passes when they adopt different orientation over a beach, as well as to observe how much information is lost when the passes are moved away on the alongshore direction from the transect over which all the passes are projected, and which contains the assumed true profile.

In order to create the synthetic ICESat-2 ATL03 data, two different DEMs, from which the elevations for the assumed correct profile and synthetic passes are extracted, are used: *The Actueel Hoogtebestand Nederland 2* (AHN 2) and *Référentiel à grande échelle* (RGE). These publicly available DEMs are respectively from Netherlands and France, and each one contains the elevations for their own territory. From these DEMs, a beach from each one, with different geometries, are extracted and analyzed separately, see location and DEMs in Figure 3.9, and aerial views in Figure 3.10. Uncertainties on the elevations of the DEMs are not commented in this report because the usage of this data is solely intended to provide insights into how the information contained in each DEM translates within itself.

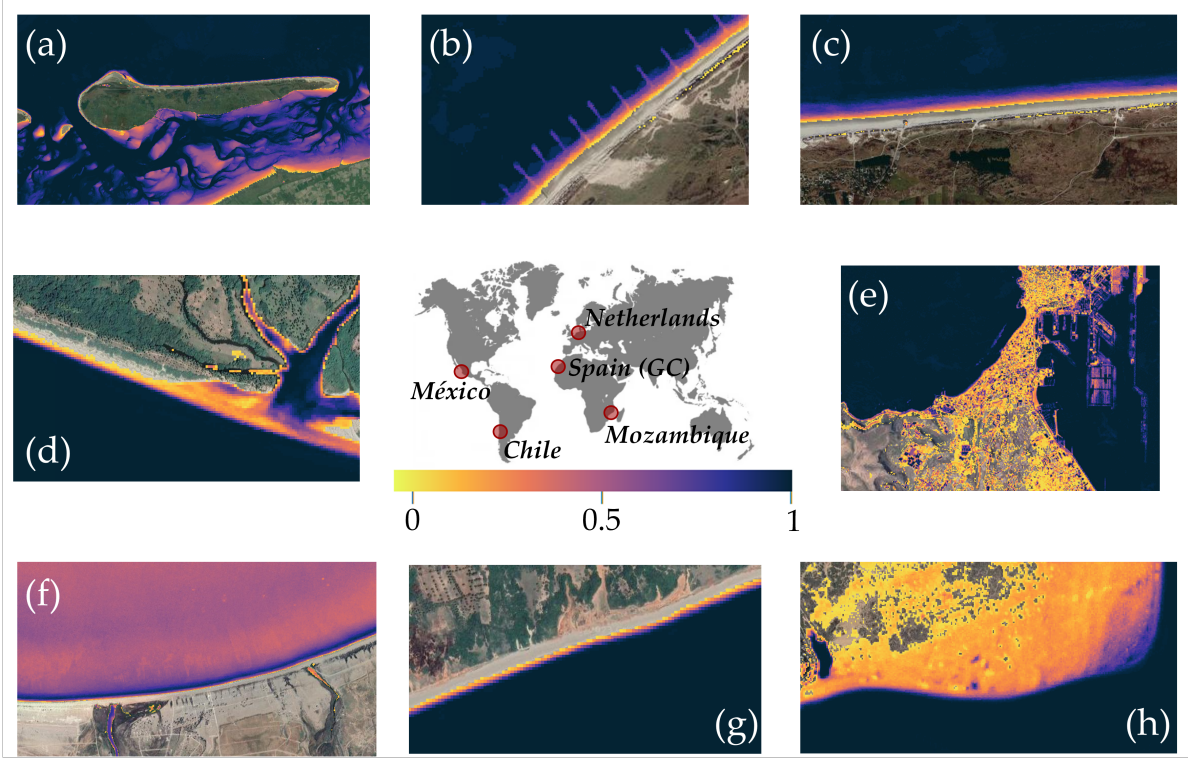


Figure 3.8: Computed Water Occurrence Probability layer, WOP, in different parts of the world. Panels (a), (b), and (c) belongs to the islands at the north of Netherlands, panels (e) and (h) to Gran Canaria, Spain, panel (d) to Guerrero, México, (f) to Coquimbo, Chile, and finally panel (h) to Zavala, Mozambique. The world map on the center shows the location of the different panels and below it has a color bar indicating approximately how the colors correspond to the water occurrence probability.

After setting the different passes over the DEMs and extracting elevations following the procedure explain in the corresponding section of Chapter 4, noise is added to the points following the default uncertainties that best represent the current most accurate estimates using on-orbit data as shown in Table 2.1: for height $\sigma_h = 0.17[m]$, and for the along and across track, $\sigma_{along} = \sigma_{across} = 5[m]$, or what is approximately the same for latitude and longitude, $\sigma_{lat} = \sigma_{lon} = 0.000063[deg]$ [18].

It is assumed that the uncertainties follow a Gaussian distribution,

$$p(x) = \frac{1}{\sqrt{2\pi}\sigma} e^{-\frac{(x-\mu)^2}{2\sigma^2}}, \quad (3.1)$$

where μ is the mean, or the location parameter, center in zero, and σ the standard deviation, or the scale parameter, the value given as uncertainty for each coordinates. The distribution has a bell-shaped curve with its peak at the mean, and its spread increases with the scale parameter (the function reaches 0.607 times its maximum at $x + \sigma$ and $x - \sigma$). This implies that values close to the mean are more likely rather than those far away [49].

From three Gaussian distributions, each having a mean of zero and a standard deviation of either 5 meters (for the "along" and "across" coordinates) or 0.17 meters (for the elevation), random samples are extracted. These randomly selected values are added to the corresponding coordinate, hence, obtaining the synthetic geolocated photon.

Figure 3.10 highlights the contrasting characteristics of two selected beaches. The upper beach located in Ameland, Netherlands, is a long beach with low alongshore variability, a wide beach face, and a tidal range up to 2.4 meters. In contrast, the lower beach located near Marseille, France, resembles a pocket beach with more variability alongshore, narrower than the first beach, and a tidal range up to 0.8 meters. The study of these two different beaches provides insights into how ICESat-2 might perform

on beaches with similar and intermediate characteristics around the world.

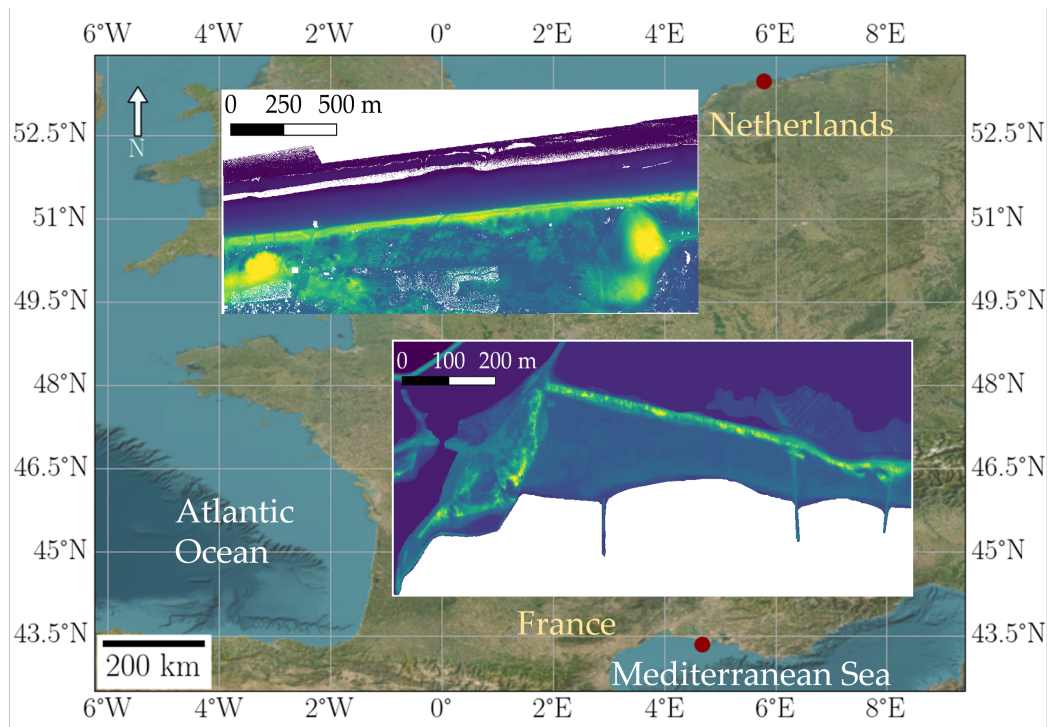


Figure 3.9: Location map and DEMs of the beaches employed for the synthetic data study. The upper DEM corresponds to the beach of Ameland, Netherlands, and the lower DEM to a beach close to Port du Grau de la Dent, in France.

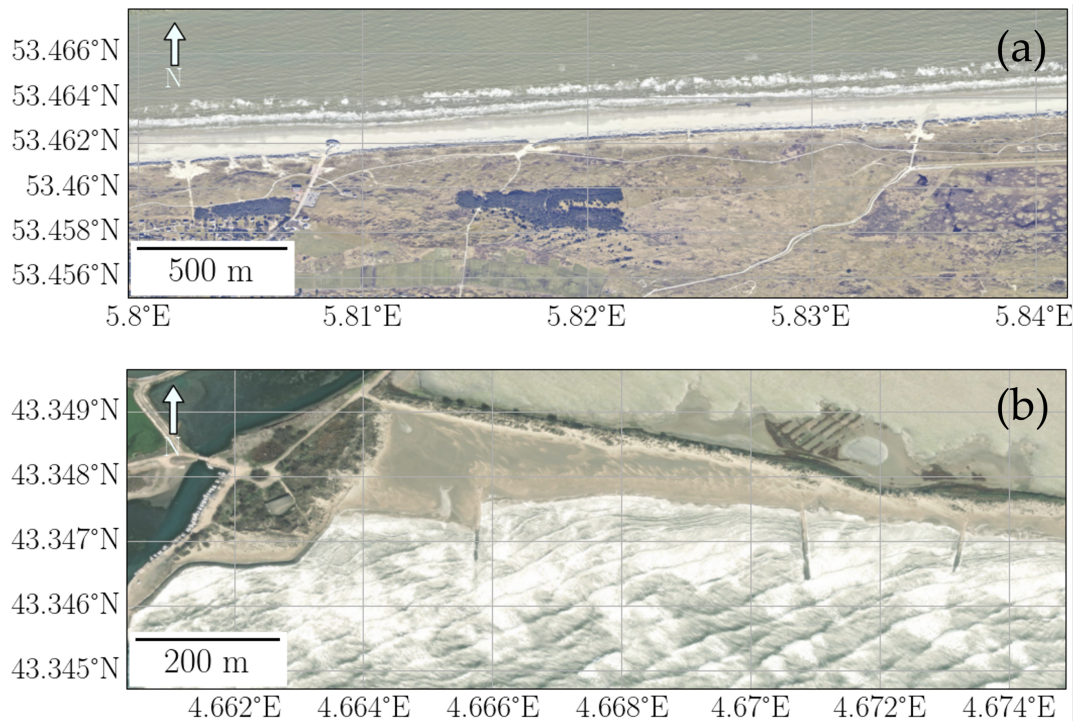


Figure 3.10: Aerial view of the selected beaches from which the corresponding DEMs are used for generating synthetic data. The upper panel (a) corresponds to a beach on Ameland (Netherlands), while the beach on lower panel (b) is located in Marseille, France.

3.6. The JARKUS dataset

The 'Jaarlijkse Kustmetingen' (Annual Coastal Measurement, from Rijkswaterstraat [50]), JARKUS, dataset comprises surveys conducted annually between April and September. This dataset includes cross-shore transect measurements, which are taken with respect to a series of permanent beach poles located along the coast. The JARKUS system was established in 1965 to monitor the coastal morphology of the Netherlands and provides data to support coastal management and policy-making. This monitoring program samples elevation profiles every 5 meters, with an alongshore interval between transects of approximately 250 meters, depending on the region [51].

The provided dataset comprises the approximately 250 meters spaced transects, onto which the ICESat-2 passes have been projected (refer to the methodology described in the corresponding section of Chapter 4). Additionally, it also includes beach profiles for each year since 1965, corresponding to the same transects. In this report, only the beach profiles that overlap with the time frame during which ICESat-2 has been in orbit are utilized. And, even though the profile comparisons are made using the measurements from the same year, it is important to bear in mind that some deviation is expected. This is, the JARKUS beach profiles are extracted between April and September, while ICESat-2 collects data through the entire year, what leads to have comparisons of winter and summer profiles. However, visual matching of the profiles, and similarity between beach face slopes are expected.

3.7. Global Coastal Transect System and global coastal buffer

The Global Coastal Transect System (GCTS9) consists of approximately 13 million cross-shore transects placed at 100 m equally-spaced alongshore resolution. The transects are derived from a generalized coastline zoom level 9(2023-01-23; Imagico, DE). The transects have a maximum length of 1500 m in their local UTM projection, but are shorter when they intersect the OpenStreetMap coastline multiple times. The global coastline buffer is derived from an OpenStreetMap coastline (2023-01-23) at 750 m, using the local UTM projection to obtain better approximate the distance. Both data products are stored in GeoParquet format.

The transect system is employed for automating the beach face slope extraction from ICESat-2 ATL03 data at a global level. However, it also allows to extract the beach face slope at any given location if necessary. The system is provided in Calkoen et al. [52]. This system allows to keep track of the areas studied, create buffers around the centre of the transects, ensuring that they contain the ICESat-2 ATL03 data over the area, and compute distances and angles between transects and ICESat-2 passes. The latter allows to project the geolocated photons to the most suitable transect, leading to the extraction of an ICESat-2 profile perpendicular to the beach, from which the subsequent cross-shore profile, beach face profile, and beach face slope can be derived.

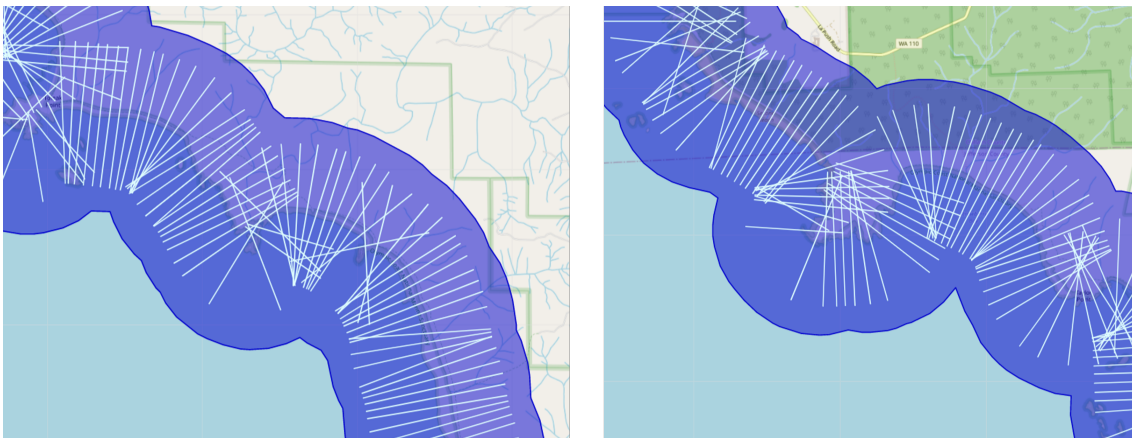


Figure 3.11: Examples of the transect system and coastal buffer

Finally, regarding the above presented global coastline buffer, it is used for reducing the amount of points of ICESat-2 passes to process, and focus on the ICESat-2 profile that contains the beach (see Chapter 4 for the methodology that implements this data structures).

4

Methodology

This chapter presents the methodology the main research question of this report: to what extent can the beach face slope be derived from ICESat-2? It encompasses a comprehensive approach to address the research questions (presented in section 1.1) by employing various designed methods. Each method has been tailored to tackle specific aspects of the study. Figure 4.1 provides a visual representation, outlining the key objective of these methodologies and illustrating the interplay between them. This figure serves as a valuable guide for understanding the sequential steps involved in the research process and the interrelationships among the different methodologies employed. The developed methods aim to answer the different research subquestions (section 1.1) and give the most realistic and accurate insights.

Figure 4.1 presents the different methods developed throughout the report, their individual goals, and how they relate to each other. Step 1-*Validation*, has as main goal to assess how well, ICESat-2 can extract beach features (beach profiles, beach face profiles, and beach face slopes). Therefore, this is the validation stage, which answers the first research subquestion (*How accurate can beach profiles, and the subsequent beach face slopes be extracted from ICESat-2 ATL03 data?*). This stage consists on two methods. These are developed for comparing ICESat-2 ATL03 data with datasets from two different sources: from a Terrain Laser Scanner (TLS) of the CoastScan project, and from an RTK-GPS (sections 3.2, and 3.3 respectively). These two methodologies are relatively similar and are described in section 4.1. Once the validation is done, step 2-*Synthetic data* assesses the impact of the angle, α , and distance, d , between passes and transects on the beach profiles, beach face profiles and beach face slopes. In this step, a method for creating synthetic data, and the subsequent one for its analysis, are developed and properly defined in section 4.2. This step aims to answer the second research subquestion: *How dependant is the beach face slope extraction from ICESat-2 passes on beach geometries and the direction of its own fixed ground track?*.

Step 2-*Synthetic data* sheds light on optimal values of α and d for the beach face face slope estimation, then, these values are used as thresholds for the novel method presented in the next step. Step 3-*Upscaling* presents a beach face slope extraction methodology that can be implemented at a global scale. The implemented methodology is locally tested using the JARKUS dataset (section 3.6) and it is also partially used for exploring the spatial and temporal resolution of ICESat-2 ATL03 data in coastal areas globally (answering third and forth research subquestion: *What are the limitations regarding the ICESat-2 spatial and temporal resolution? To what extend can ATL03 data be used for monitoring beach face slopes and What are the possibilities for upscaling a beach face slope extraction methodology from ICESat-2 ATL03 data?*). The method for upscaling the beach face slope extraction is presented and detailed in section 4.3.

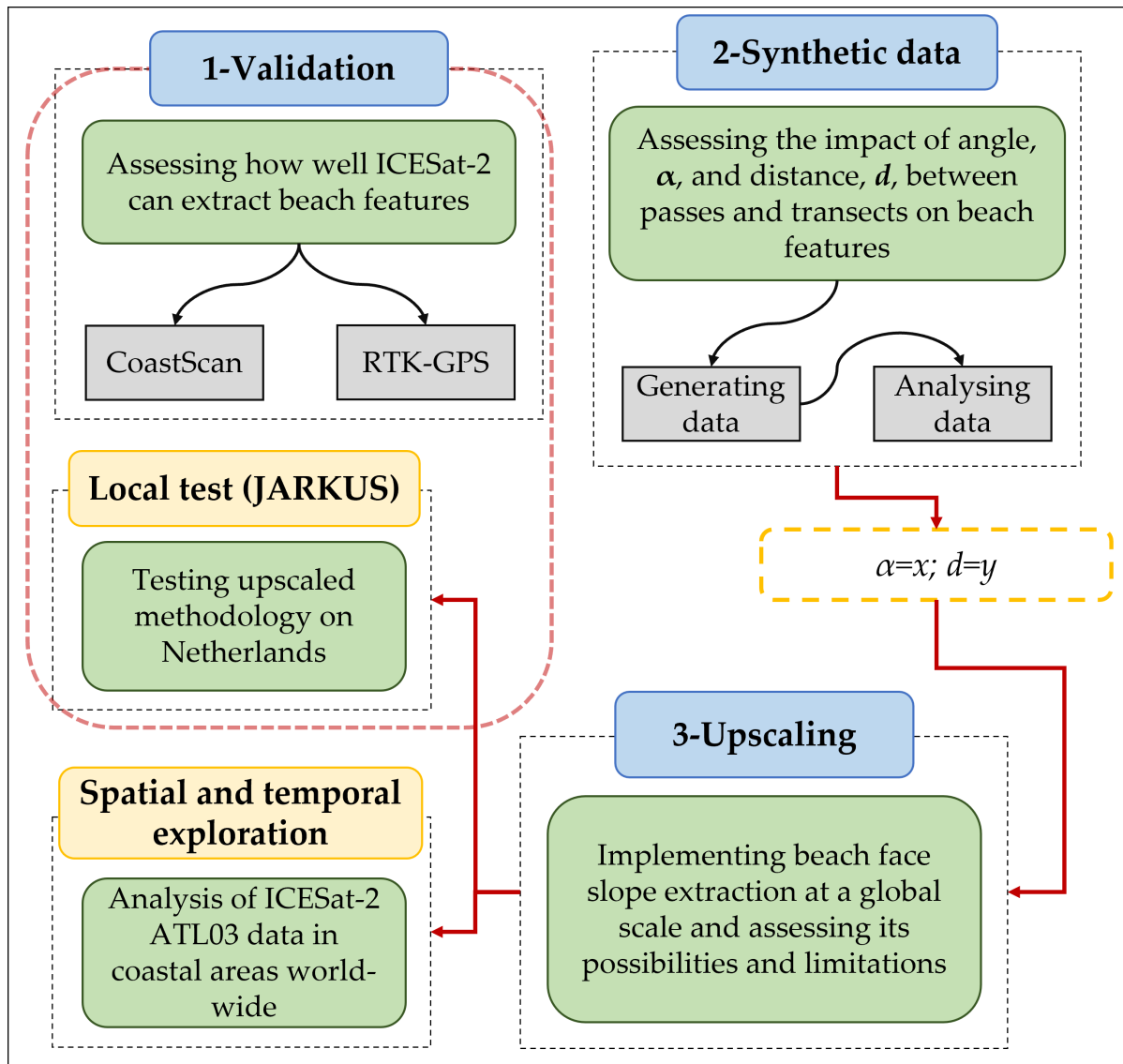


Figure 4.1: Scheme of the methodologies distribution and main goal of each one of them.

4.1. Assessing ICESat-2 accuracy for beach features

As a first step towards answering the main research question, to what extent can the beach face slope be derived from ICESat-2, a validation phase of the data to use is imperative. Then, for validating ICESat-2 ATL03 data, two datasets are employed, and two similar methodologies are implemented with this goal. The two validation datasets utilized are the Terrain Laser Scanner, TLS, point cloud from the CoastScan project, and RTK-GPS measurements (see sections 3.2 and 3.3 respectively)

4.1.1. CoastScan

This subsection describes how ICESat-2 ATL03 data is compared against field data from the CoastScan project (section 3.2). The objective of the developed method is to compare ICESat-2 profiles on the shoreface with data as close in space and time as possible; to assess in the most optimal way an area as variable in time and space as beach faces are. The Terrain Laser Scanner (TLS) of the CoastScan project located on Noordwijk, Netherlands (see Figure 3.3), allows to compare a scan done the 30th of March of 2021, at 20:01, with two ICESat-2 passes (the strong and weak beam) with a difference in time of 12 minutes, and from the same date, but acquired at 20:13 (Table 3.1).

Firstly, the region of interest surrounding the laser scanner was selected for determining if any ICESat-2

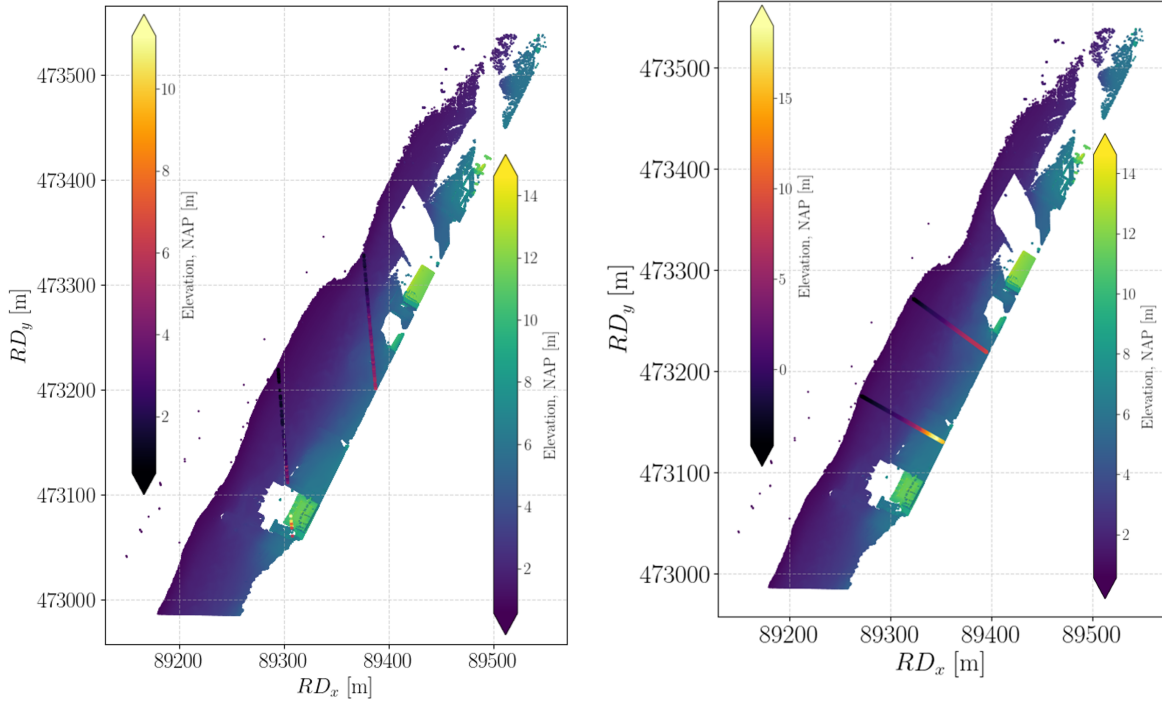


Figure 4.2: The left panel contains ICESat-2 geolocated photons from the passes that overlap the TLS point cloud, while the right panel presents the projected ICESat-2 passes into a drawn transect perpendicular to the coastline. Two different colormaps are employed for distinguishing between datasets, left color bar for ICESat-2 elevations and right color bar for the TLS scanned elevations.

data was available. Only these two beams from the same pass were overlapping the area scanned by the TLS. Once the pass of interest was determined, the closest TLS point cloud in time was selected and transformed from its native coordinate system, where $(0, 0, 0)$ corresponds to the laser scanner, to the Dutch coordinate system RDNAP. Next, after filtering the passes to keep only the photons with 'High' quality flag, the resultant photons, in geodetic spherical coordinates as geodetic latitude, longitude and height above the WGS-84 ellipsoid, are also converted to the Dutch coordinate system RDNAP. Both datasets in the same coordinate reference system can be seen in the left panel of Figure 3.4. Meanwhile, in the left panel of Figure 4.2 only the photons that overlap with the TLS point cloud are retained.

As a final step of the pre-processing stage, each ICESat-2 pass is smoothed by applying a moving average with a windows size of 20 points. Now that the data has been pre-processed and both datasets are in the same Coordinate Reference System (CRS), the methodology for comparing ICESat-2 and the TLS point cloud can be applied. The goal of this workflow is to extract profiles from the TLS point cloud for a qualitative, as well as a quantitative assessment by comparing them with the ones given by the passes, or with their projections into a perpendicular transect to the coastline. In Figure 4.3 it is possible to see that the first step is to create a circular buffer around the geolocated photons coordinates of 30 cm of radius. Then, all the elevations of the points from the TLS point cloud within the buffer are kept and the mean is taken (step 2). If there is no TLS points inside the buffer, the geolocated photon is dropped. After this, two profiles, with the same number of points, the number of geolocated photons within the point cloud, are obtained and compared (step 3).

The step 4 of the method is to manually draw a transect perpendicular to the coastline. This is done for each pass. Then, in step 5, the smoothed ICESat-2 passes are projected onto the created transects. In Euclidean geometry, for projecting a point to a line, the shortest distance must be found. The shortest path from a point to a line is through a perpendicular line, then, assuming the line to be the drawn transect, the slope of the transect, m_t , is computed,

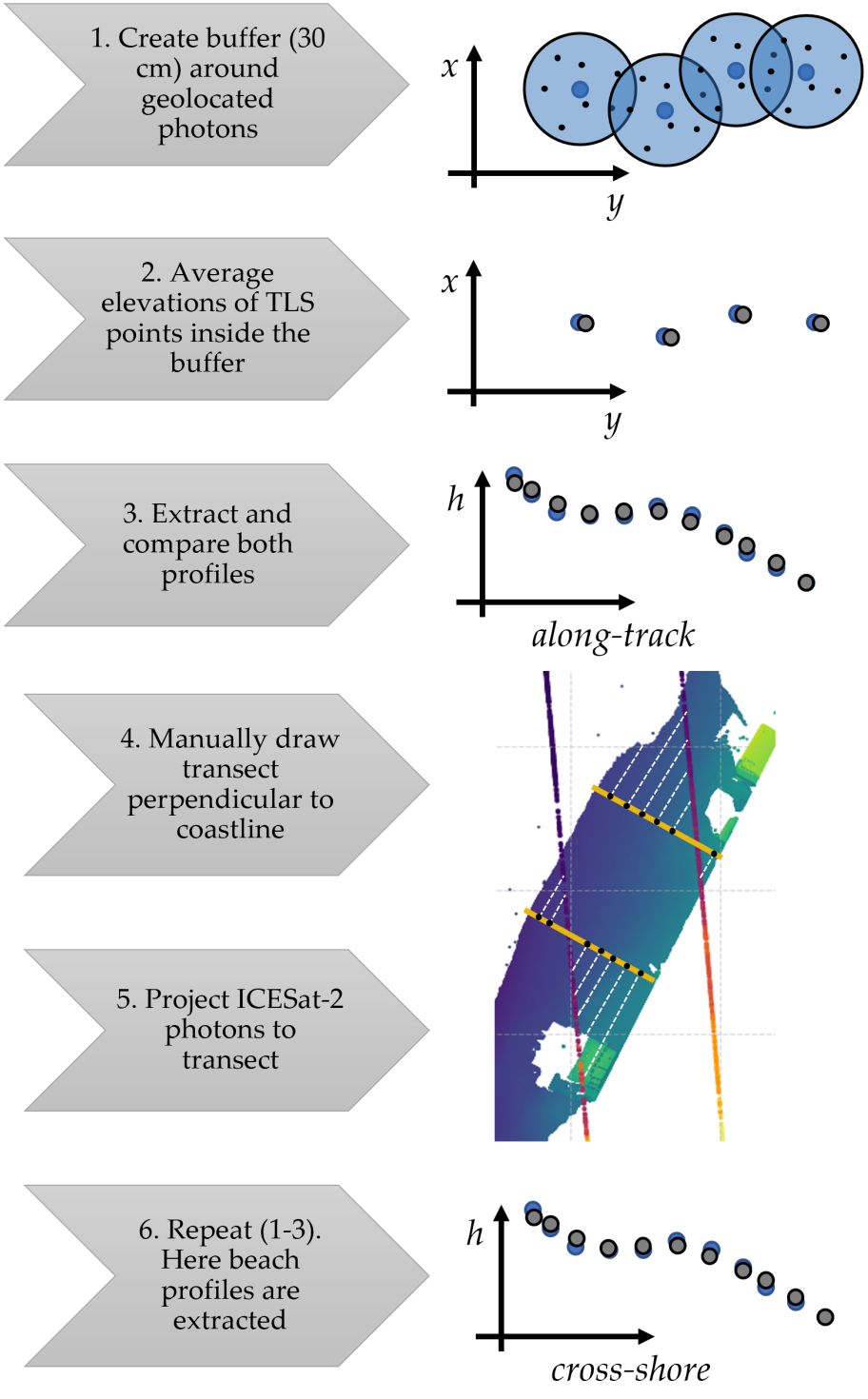


Figure 4.3: Method created for extracting profiles from TLS point cloud using ICESat-2 ATL03 geolocated photons.

$$m_t = \frac{y_2 - y_1}{x_2 - x_1}, \quad (4.1)$$

where (x_1, y_1) and (x_2, y_2) are two points within the transect. Then, if the slope of the transect is known, the slope of a perpendicular line is computed as $m_{pt} = -1/m_t$, where the subindex pt stands for point, because this is the slope for the perpendicular line joining the geolocated photon of the pass with the transect. Now that the slopes of both lines are known it is possible to compute the intersection of these lines with the y -axis, n_{pt} and n_t . Once these are computed both lines have been completely defined and it is possible to find the intersection point (x_0, y_0) between these two lines by applying the following equation:

$$(x_0, y_0) = \left(\frac{n_{pt} - n_t}{m_t - m_{pt}}, \frac{n_t \cdot m_{pt} - n_{pt} \cdot m_t}{m_t - m_{pt}} \right) \quad (4.2)$$

Once the intersection point of the two lines, (x_0, y_0) , has been found, the point is projected to its new location over the transect. This is done for all the points of the smoothed passes, each pass is projected to its respective drawn transect, and then, with the new cross-shore profiles, the corresponding TLS points are extracted from the point cloud (by repeating steps 1 to 3 of this methodology, see right panel Figure 4.2). Finally, these beach profiles can also be compared, and analyzed in detail.

The Mean Absolute Error (MAE , Eq. 4.3), the Mean Squared Error (MSE , Eq. 4.4), and the Root Mean Squared Error ($RMSE$, Eq. 4.5) are computed for both ICESat-2 profiles, as well as for the projected ones. Also the beach face slopes of the profiles are extracted, and the difference between the slope extracted and the computed from the assumed true beach face profile is presented, as well as the respective Percentage Error (PE , Eq. 4.6). The different statistics are computed as follows,

$$MAE = \frac{1}{n} \sum_{i=1}^n |y_i^{obs} - y_i^{pred}|, \quad (4.3)$$

$$MSE = \frac{1}{n} \sum_{i=1}^n (y_i^{obs} - y_i^{pred})^2, \quad (4.4)$$

$$RMSE = \sqrt{MSE} = \sqrt{\frac{1}{n} \sum_{i=1}^n (y_i^{obs} - y_i^{pred})^2}, \quad (4.5)$$

,and

$$PE = 100 * \frac{abs(y_{obs} - y_{pred})}{y_{obs}}, \quad (4.6)$$

where y^{obs} or y_{obs} is the observed or ground truth value of the corresponding parameter, y^{pred} or y_{pred} is the predicted/extracted value, and n is the number of comparisons, the length of the true or predicted value.

In Noordwijk the mean semi-diurnal tidal range is 1.7, with 2.1 m at spring tide [53]. For accounting for wave set-up and extreme events that might have occurred, for the validation cases, TLS and RTK-GPS, the statistics for the different profiles are extracted from the manually demarcated coastline up to 2.5 m over the NAP. Then, the beach face slope is computed for this section of the profile, and as mentioned, the difference between the slope extracted and the computed from the assumed true beach face profile is presented, as well as the respective PE (Eq. 4.6). Furthermore, the mentioned metrics are also calculated for the entire profiles, spanning from the delineated shoreline to the highest elevation permitted by the datasets.

Finally, it is important to address that the inclination file, responsible for correcting possible variations due to wind or small movements of the TLS, has not been applied to the point cloud because it was corrupted. In order to solve this, after obtaining the resulting profiles from ICESat-2 and the CoastScan,

the profiles are overlapped manually and the height difference is then added to the vertical axis on the point cloud and the process is repeated. This de-trending process does not pose a major problem when it comes to comparing beach profiles, their shape and the beach face slopes extracted. The shape of both profiles and how they relate to each other is more important than the accuracy with which ICESat-2 is able to extract the elevation, but how well it works for extracting the elevations within a range (beach profile) and how this elevations relate to each other (beach profile shape).

4.1.2. RTK-GPS

For this validation method, the real-time kinematics-global positioning system, RTK-GPS measurements are used. As explained in Chapter 3, in principle, the measurements were taken following the expected path of an ICESat-2 pass of the previous day. However, by the end of the report, the data has not been released, and therefore, the comparison is made using an older ICESat-2 which path was followed (see Table 3.2, and Figure 3.6).

This method has some points in common with the explained in the previous subsection, subsection 4.1.1. However, a few details are different regarding the steps taken prior to the extraction of the profiles to compare. Even though in this case the measurements done are directly profiles, because it was done manually, in Figure 3.6 some small deviations from the passes can be seen. Then, for having the profile over the same line as the geolocated photons of ICESat-2 ATL03 data, the measured profiles are projected over the ICESat-2 passes. This is done as previously explained in section 4.1.1, but the line to project the points onto is generated by taking two points from the ICESat-2 pass and projecting the measured points onto them.

Then, the validation profiles are compared to the ICESat-2 profiles, and metrics are computed to evaluate their similarity. Secondly, for extracting beach profiles from ICESat-2, the measured cross-shore profiles with RTK-GPS, are used for creating two lines by taking the first and last points of both profiles. The geolocated photons from the respective ICESat-2 profiles are projected onto these lines, and metrics are calculated to compare the profiles. Additionally, the lower boundary of the beach face is demarcated manually, and the upper boundary is set at 2.5 meters as in the TLS validation method (subsection 4.1.1) due to the tidal range of the area [53]. The resulting beach face profiles and slopes are then compared.

4.2. Generating and analysing synthetic ICESat-2 ATL03 data

This section describes the methods employed for understanding the dependency of ICESat-2 ATL03 extracted beach profiles, and subsequent beach face profiles and beach face slopes on the angle and distance between passes and the transects they are projected into. This section consists on two parts: 1) the synthetic data generation; and, 2) the comparison between this synthetic data and the elevation beach profile, that is considered as ground truth. Figure 4.4 shows the first part of this methodology, for visually understanding the process, to the right of each step the 2 cases used are presented (see previous Chapter 3 for exact location and data description). First, a beach DEM (see section 3.5) is selected, here it is possible to observe how the one to the left, Ameland in Netherlands, is longer and wider than the selected beach of Marseille, France. Then, for both DEMs, the coastline is manually defined based on the features of the DEM or the area itself (satellite imagery from Worldview), and from the drawn line, a perpendicular transect is generated by computing the slope of the line defining the coastline, and getting its opposite reciprocal, $m_{transect} = -1/m_{coastline}$, this is, the perpendicular slope which defines the perpendicular transect. The transect is intended to capture the beach profile, from the most upper part to the most offshore section on the DEM (see Figure 4.4). The point further away from the ocean of this beach profile is considered the (0,0) and all distances are computed based on this.

In step 4 and 5, the transect is divided in 21 equivalent parts and 20 points are taken as intersection points. Then, a set of $d/0.7$ number of points is created over each line with a step of 70 cm, the along-track interval of ICESat-2. Each line intersecting each of the intersection points with different angles (α), $[0, 90]$, with respect to the transect, are created. Finally, the last step of this part of the

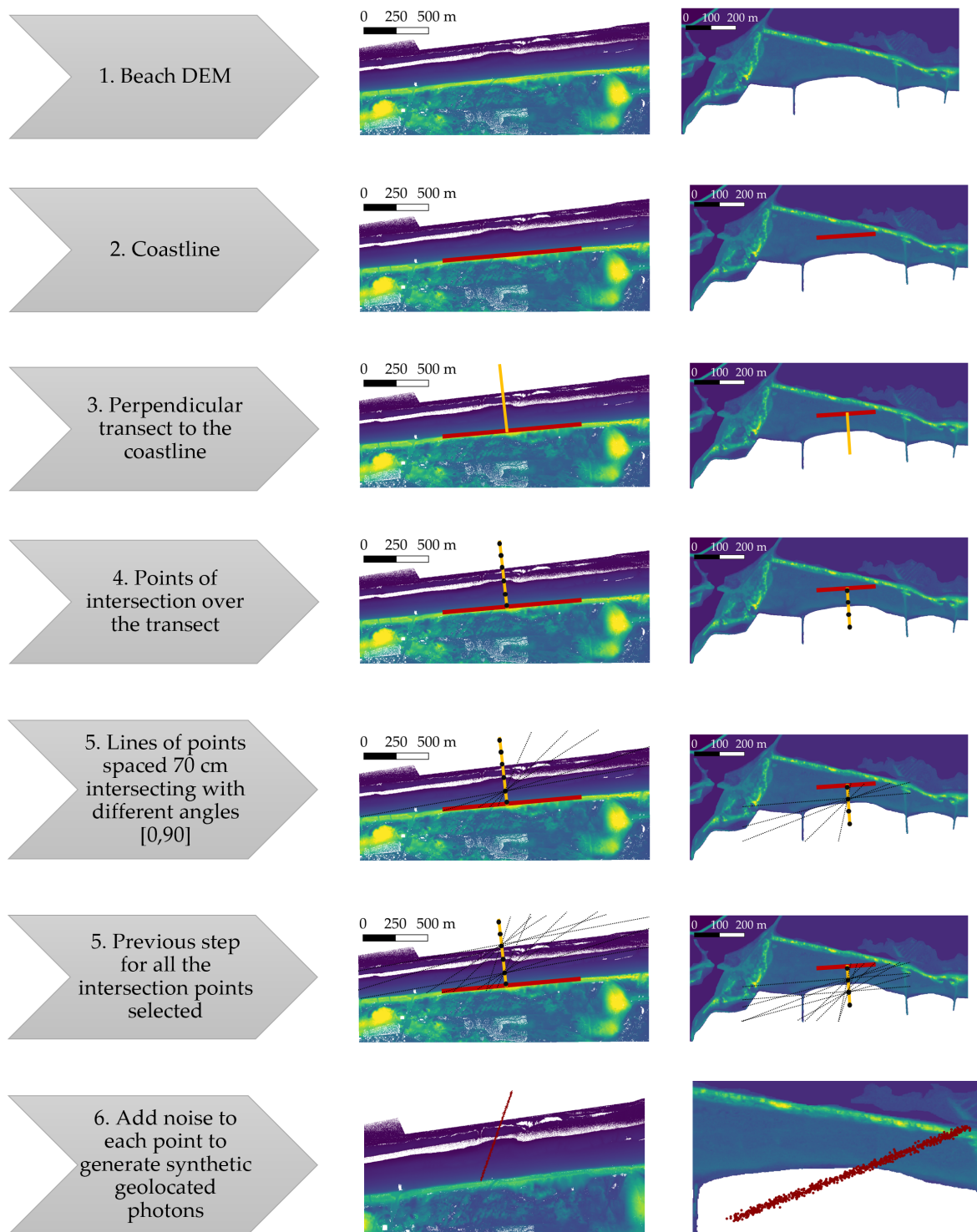


Figure 4.4: Method followed for generating synthetic ICESat-2 ATL03 passes with different angles, from 0 to 90 degrees with respect to the transect, and repeating the same process at different intersection points of the transect.

methodology is to add noise to the created points in order to get a pseudo-geolocated photon, noise is added in the 3 dimensions, in the latitude and longitude (along-track and across-track) and in height. The added noise follows a Gaussian distribution (Eq. 3.1) following the given uncertainties that characterize ICESat-2 ATL03 data presented in Chapter 3. This is, to the along-track and across-track, noise is generated randomly following a normal distribution of $\mu = 0[m]$ and $\sigma_{along-track, across-track} = 5[m]$ and to the height over the ellipsoid, noise is also generated but with a normal distribution with $\mu = 0[m]$ and $\sigma_{height} = 0.17[m]$.

For each DEM, the respective transects contain 20 intersection points, and on each of these points 91 passes intersect with different directions, what leads to 1820 synthetic ICESat-2 ATL03 passes created per DEM. Then, they are assessed according to the second stage of this method, the steps taken for comparing both: the assumed true beach profile and beach face slope, with the different beach profiles and beach face slopes extracted from the synthetic passes.

Figure 4.5 shows the process followed for comparing the elevations of the profiles created following the above presented methodology, are compared with the assumed true profile. The first step is to overlap to the profiles with the corresponding WOP layer extracted for each AOI, Marseille (FR) and Ameland (NL). This layer contains the probability of a pixel/area being water or land, and it has been fixed to contain values between the interval $[0.1, 0.9]$, if the value is below 0.1 it is assume that the point is always land, and if it is above, it is always water. This is done for avoiding possible noise and capturing only the intertidal area. Finally, following a similar idea to what is presented as the first step in Figure 3.4, a buffer is created around the synthetic photons and the values of the WOP layer inside the buffer are averaged, then this value is assigned to the corresponding point.

Once it is known with which probability each point is land or water, the generated point cloud lines are smoothed by applying a moving average (windows size of 20 points), and these points are projected onto the transect, in which the same profile is obtained, but the distance between the points has become smaller. Now, all the passes are over the transect, with photons containing values from the WOP layer if it is inside the intertidal area, or not a value if it is outside this area. A first comparison, shown as the third step in Figure 4.5, is to compare the full profiles, the synthetic, projected and smoothed pass, including all the pseudo-photons, and the assumed true profile. For doing this, the most onshore point of the transect is taken as the $(0, 0)$, and all the distances from this point to the points of the transect, and the projected pass are computed. With this, a 2D profile is obtained, with the distance in meters as $x - axis$ and the elevation in meters as the $y - axis$. Then, for comparing the elevations at the same distance from the center of the fixed coordinate system, a curve is fitted to the synthetic pass and the respective elevations are obtained for the value of interest over the $x - axis$. This allows to compare it with the assumed true profile. The statistics computed are MAE, Equation 4.3, MSE, Equation 4.4, and RMSE, Equation 4.5.

In step 4 the profile containing values from the WOP layer, this is, the intertidal area, are kept, and the profiles obtained are again compared by computing the same statistics as for the full profiles (MAE, MSE, and RMSE). Finally, with the beach face profile demarcated, it is possible to compute the beach face slope. For this, the first and last point of this profile are taken and the beach face slope is obtained by making use again of Equation 4.1.

The results for *MAE*, *MSE*, and *RMSE*, as well as for the slope differences are presented in a 3D mosaic with the angle as $y - axis$ and the transect distance as $x - axis$. Once the statistics and slopes for all the profiles of the 20 intersection points over the transect and per degree has been computed, for creating the 3D mosaic, a linear interpolation is done.

It is important to bear in mind that the importance of this methodology is not how well the beach face is extracted, or the quality of the synthetic data, but how the passes behave when being projected into a beach profile, into a transect perpendicular to the coastline, if it loses spatial information in the intertidal area or if it is able to keep it and show similarities with respect to the actual beach face of the beach profile.

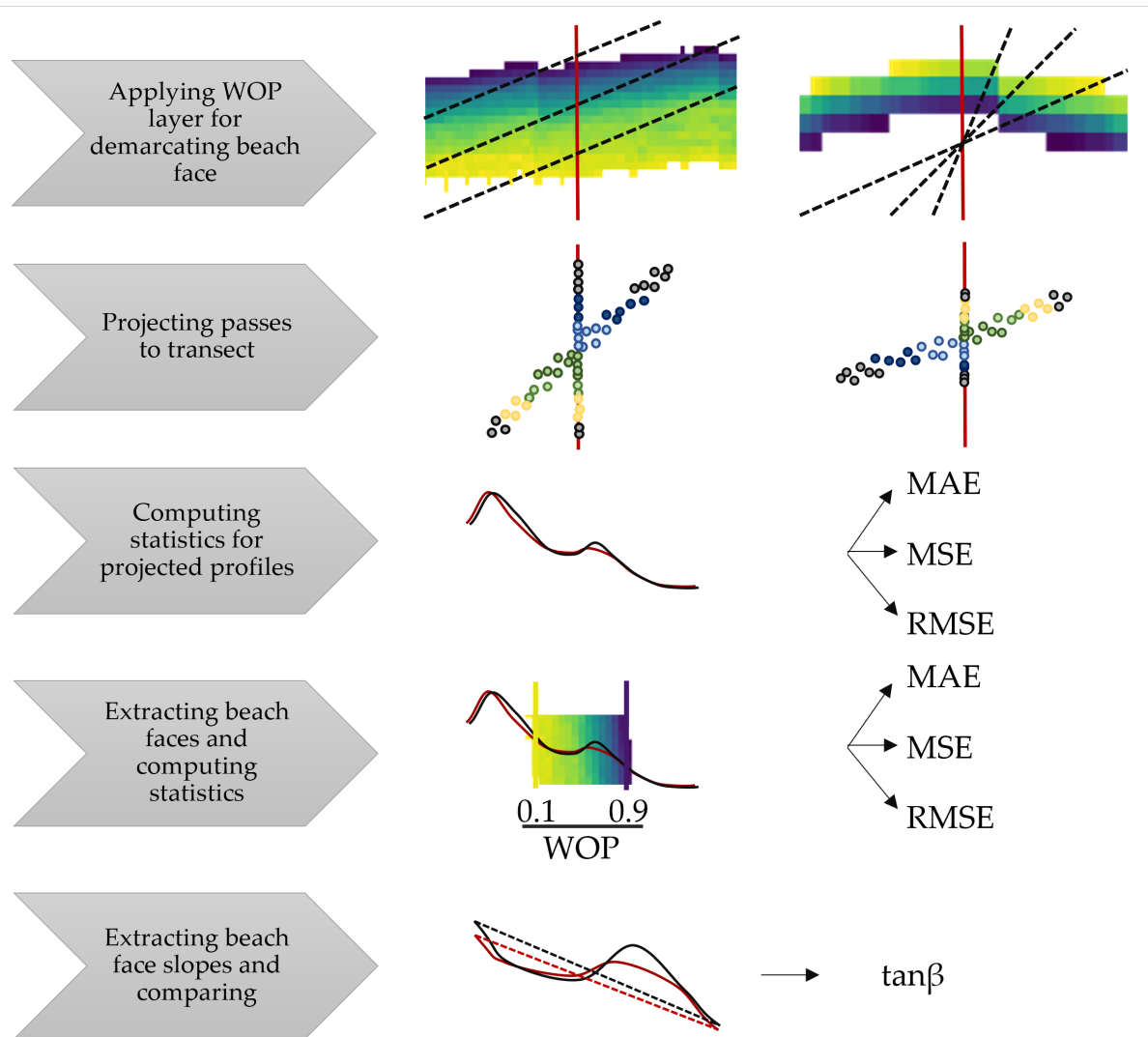


Figure 4.5: Sketch of the methodology used for demarcating the beach face profile using WOP layer and computing the beach face slope, $\tan\beta$.

4.3. Extracting beach profiles and subsequent beach face slopes at a global level

As stated in the previous chapters, the main goal of this report is to assess the validity of ICESat-2 data, specifically ATL03 data, for extracting beach face slopes. For this, not only beach face slopes but beach profiles of different areas and from different datasets has been compared (see Chapter 3). These comparisons have been made in order to assess how accurate can beach profiles, and subsequent beach face slopes be extracted from ICESat-2 ATL03 data. However, the validation datasets are small and more comparisons must be made to give a more informed discussion and conclusion. Therefore, the upscaling methodology explained in this section does not only provide the workflow to follow in order to extract beach profiles, and the subsequent beach face slopes, world-wide with ICESat-2, but it is also employed as validation methodology by using the JARKUS dataset presented in Chapter 3.

First of all, for implementing the methodology it is important to consider the beach face slope definition given in this report. As explained in Chapter 2, the beach face slope or beach slope is the inclination of the area comprised between the upper limit of the high tide and the lower limit of the low tide, the beach face or intertidal area. In addition, the beach face slopes are computed from the section of the beach profile that falls in the named section, and the beach profile has to be perpendicular to the

coastline, therefore, in order to correctly implement this novel methodology, transects perpendicular to the coastline must be provided.

As shown in the schematic overview of the process for upscaling the beach profile and beach face slope extraction presented in Figure 4.6, the workflow starts by using the system of transects presented in Chapter 3. One transect is taken, and its centroid, or center of the transect, is computed. From the defined centroid, a buffer of 30 km is created and a box enveloping such centroid is originated from this. Then, with this box of 60 by 60 km, the Reference Ground Tracks (RGTs) of the satellite over the area can be found. With a square of this size, it is ensured that the RGTs over the area which may contain profiles of the area of interest (AOI) are found, finding at least three RGTs (see Figure 2.6). Downloading all the data within a box of 3600 km² is a large query, hence, an inner buffer is created for reducing the amount of data to download. From the already computed centroid, a buffer of 10 km and the respective box encapsulating it are generated. Taking the corners of the box as the extents for

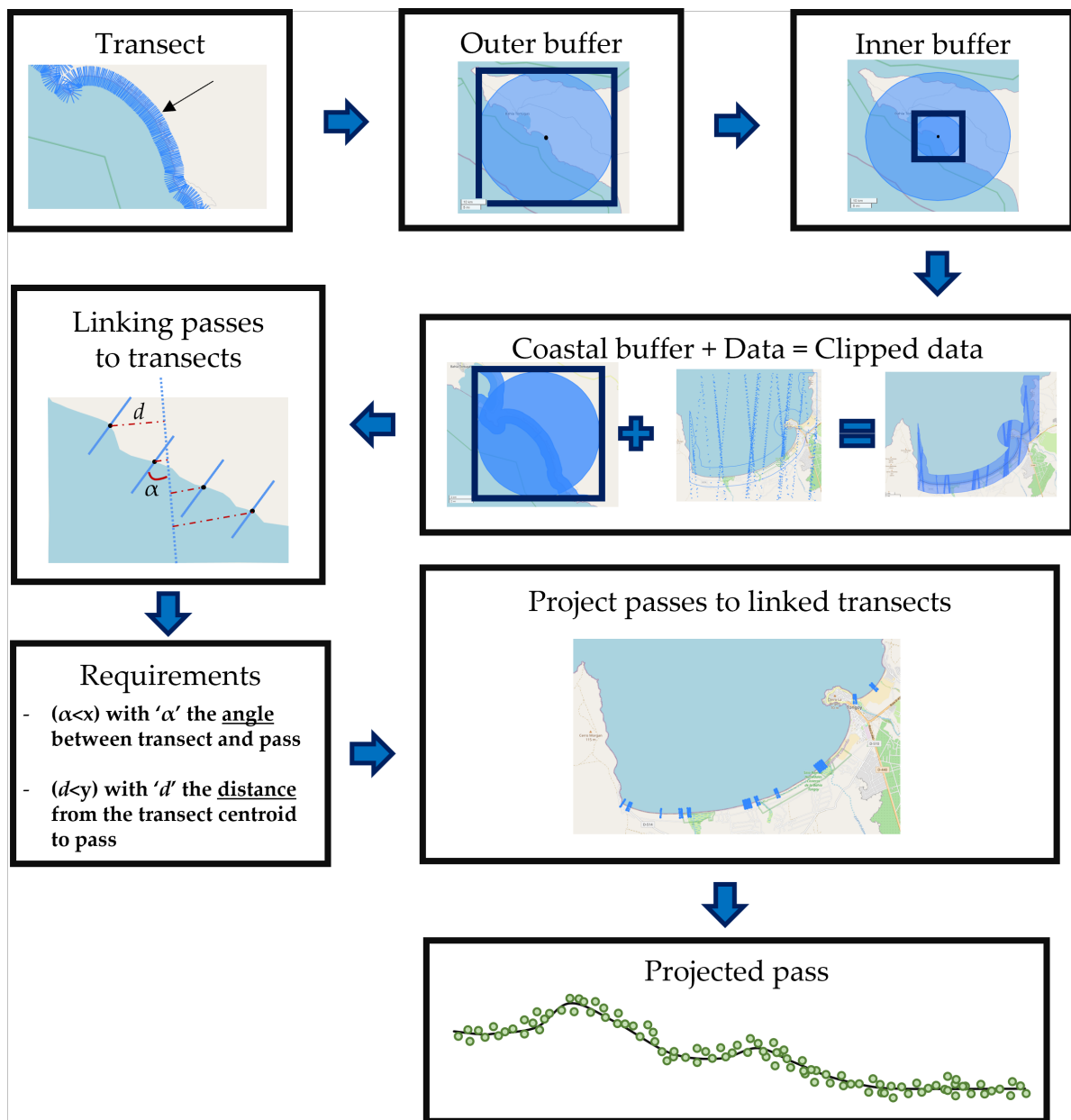


Figure 4.6: Methodology followed for extracting beach profiles.

querying the data, it is downloaded.

Once all the data of the box has been downloaded, the coastal buffer (see Chapter 3) is fixed to the inner box, and the data inside the polygon is kept. After ICESat-2 data has been downloaded, re-projected to the local UTM, and clipped to the coastal area of the inner box, each pass is linked to the closest transect by computing the distance between the centroid of the transects inside the inner box. For doing this, a methodology similar to the one explained in step 5 for Figure 4.3 for projecting points is employed. This is, the intersection of a line perpendicular to the ICESat-2 pass with respect to the centroid must be found. Then, by making use of Equations 4.1, and 4.2, the projected point of the transect centroids on the ICESat-2 generated line are found. The distance between both points, or what is the same, the distances between transects and a pass are found by simply applying the Pythagorean theorem,

$$d = \sqrt{(\Delta x)^2 + (\Delta y)^2} = \sqrt{(x_c - x_0)^2 + (y_c - y_0)^2}, \quad (4.7)$$

where (x_0, y_0) is the point where both lines intersect and (x_c, y_c) is the centroid of the transect. Finally, with the distances from all transects to the pass of interest, the closest transect is linked to the pass. At this step, also the angle between the selected transect and the pass is computed as follows

$$\alpha = \arctan \frac{\text{abs}(m_p - m_t)}{(1 + m_p * m_t)}, \quad (4.8)$$

where m_p is the slope of the pass and m_t the slope of the transect.

Based on the computed parameters in the above step, angle between pass and transect, and distance from transect to pass, the passes can be filtered based on the different requirements, which are derived from the synthetic ATL03 data analysis explained in Chapter 3.

Then, the passes that meet the requirements, and their respective transects inside the inner coastal buffer, are left. A moving average (window size of 20 points) is then applied to each ICESat-2 pass to smooth the profile. The resultant points are projected onto their respective transects (see step 5 of Figure 4.3, and Eqs. 4.1, and 4.2), and as a result, a profile perpendicular to the beach is obtained.

Finally, after extracting the perpendicular beach profiles, the next step is to demarcate the beach face and compute its slope. For this, a simple method is implemented as a first step of automation. First of all, the ICESat-2 pass inside the coastal buffer is divided in five sections, and the section located the most offshore is selected. The goal of this is to select the sea section, and compute the MSL of that section, which depends on the tide at the moment of the measurement. Once this is done, a buffer based on a primary standard deviation from the points within the section is created. Then, from the geolocated photons within the buffer, the coastline is defined as the mean of the points within the buffer plus 2 times the standard deviation of the points inside the named buffer. The latter proposed method for defining the beach face has been made following a similar methodology as in a recent report [15]. But some modifications have been done in order to get as much information as possible from the beach profile extracted (by projecting ICESat-2 passes to cross-shore transects and obtain cross-shore profiles rather than just the final beach face slope value), and to define better the lower boundary of the intertidal area (by taking geolocated photons closer to the beach face profile, instead of using the photons from 1 to 5 km off coast for computing the MSL).

Once the lower boundary of the beach face has been defined, the upper boundary would be demarcated by an approximation depending on the tidal range of the region. For example, for the validation case using the JARKUS dataset presented in Chapter 3, as it belongs to Netherlands, the upper boundary of the intertidal area has been fixed to be 2.5 meters over the lower boundary, what is a reasonable height for Netherlands given the different tidal range through out the country, the possible wave set ups and wave extreme events.

5

Results and Discussion

In this chapter, the diverse results obtained from the conducted research are presented and discussed for providing additional clarification and insight into the findings. Therefore, this chapter presents the outcomes of the validation stage, which involves comparing validation datasets obtained from TLS (CoastScan project) and RTK-GPS with ICESat-2 passes (refer to section 5.1). Additionally, it encompasses the examination and discussion of synthetic ICESat-2 ATL03 data (refer to section 5.2). Moreover, the chapter includes the results of scaling up the methodology, demonstrated through a test case utilizing the JARKUS dataset (refer to section 5.3). Finally, the chapter explores the spatial distribution and temporal resolution of ICESat-2 along coastlines (refer to section 5.4).

5.1. ICESat-2 validation: CoastScan and RTK-GPS

In this section, the results obtained for validating ICESat-2 against field observations and terrestrial laser scanner data are shown. It comprises both initial validation datasets, CoastScan and RTK-GPS. This is, a dataset provided by the CoastScan project on Noordwijk—a point cloud measured with a TLS \sim 12 minutes before an ICESat-2 pass—, and profiles measured specifically for this document using an RTK-GPS device.

5.1.1. CoastScan

Figure 5.1 shows the different comparisons between ICESat-2 and the TLS data. The upper panels (a and b) presents the ICESat-2 geolocated photons and the extracted corresponding averaged elevations from the point cloud of the terrain laser scanner. Panels c and d present the smoothed ICESat-2 passes, and again the corresponding elevations from the TLS. Finally, the lower panels (e and f) show the profiles of the projected smoothed ICESat-2 passes, the ICESat-2 cross-shore or beach profile, and the corresponding TLS profile. For the middle and lower panels, a dashed blue line is also drawn as visual aid for the demarcation of the upper boundary of the beach face, $+2.5m$ NAP, based on the tidal range of the area [53]. Furthermore, in panel b an artifact on the beach can be observe, which is a beach house. The beach house is captured by both measurements, the ICESat-2 pass and the corresponding profile of the TLS point cloud. The presence of this house leads to a shadow in the TLS dataset, and a sudden change in height can be observed for both datasets in Figure 3.4. Then, the common data between TLS and ICESat-2 over the beach house and its shadow is removed and the rest of the profile in the offshore direction is kept. By qualitative comparison, the different profiles seem to have a relatively good agreement, when ICESat-2 passes are smoothed by applying the moving average, the match between profiles seems to increase, and when projecting the passes over the cross-shore profile some of this agreement might be lost.

Table 5.2 presents the statistics, MAE , MSE , and $RMSE$ for the profiles on panels c, d, e, and f. Correspondingly, Table 5.2 shows the different slopes extracted from the profiles of the different panels in its dimensionless form, as well as in degrees. Furthermore, the latter table also presents the difference between the compared profiles, and the percentage error (PE , Eq. 4.6). When assessing both passes or beams of ICESat-2 (IS-2) and the respective CoastScan (CS), the resulting values of MSE and $RMSE$

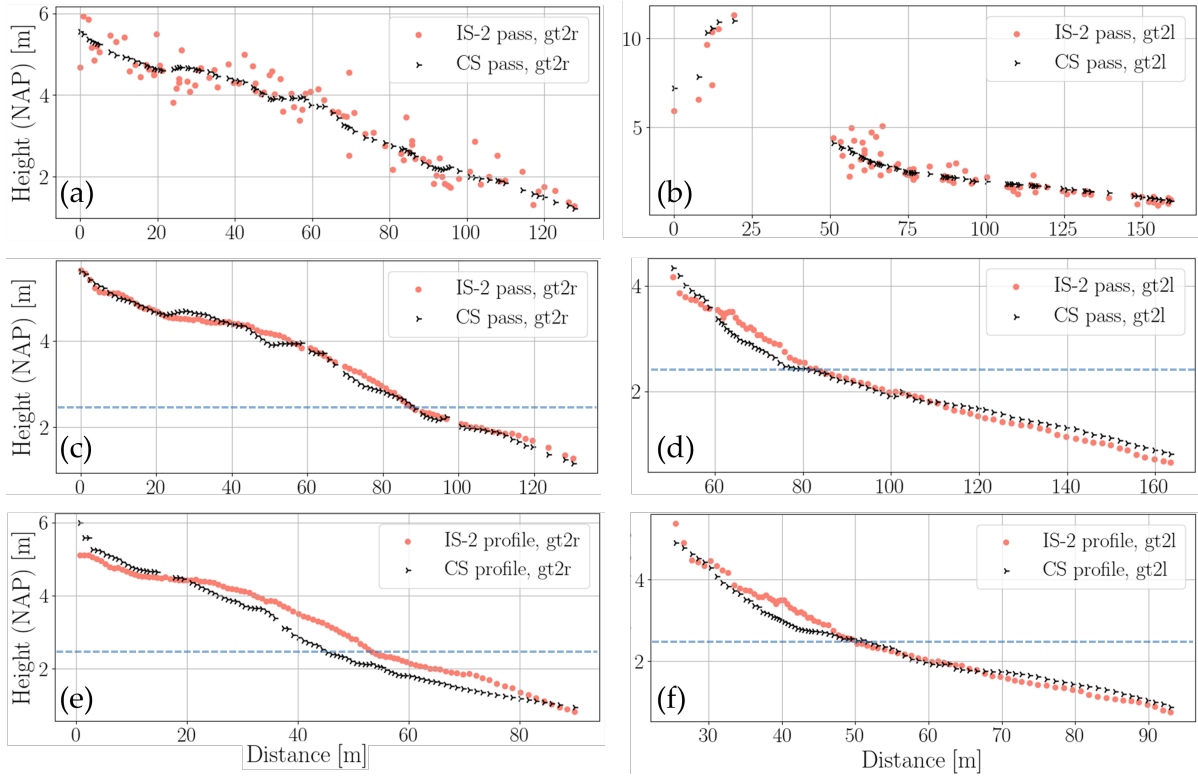


Figure 5.1: A comparison between the different profiles extracted from ICESat-2 and the corresponding ones from the CoastScan data are shown here. The profiles to the left (a,c,e) belong to the beam 'gt2r', while the profiles to the right (b,d,f) correspond to the beam 'gt2l'. The upper panels (a,b) show the geolocated photons from ICESat-2 (red) and the corresponding profile from the TLS (black). Panels c and d contain the smoothed ICESat-2 passes after applying the moving average, with a window size of 20 points. Finally, the lower panels (e,f) show the smoothed profiles after been projected into the cross-shore transect and it is again compared to the respective TLS extracted profiles. The blue dashed line represents the upper boundary of the beach face (+2.5 NAP).

are relatively low, showing good agreement between them. In addition, the *MAE* values of the profiles fall below the vertical accuracy of ATLAS (17 cm), with the 'gt2r' beam presenting a *MAE* of 9 cm, and the 'gt2l' beam 15 cm. Regarding their slopes, the differences are relatively low, with values below 0.2 degrees, what can be read as a change of less than 0.3 cm/m. Furthermore, the *PE* of both are as well relatively low, with values between 10-11 %, indicating good agreement between slopes.

However, when the passes are projected into the respective cross-shore profiles (Figure 5.1, panels e and f), Table 5.1 shows a decrease of the agreement between both profiles, especially between profiles of panel e, where the values of *MSE* and *RMSE* for these cross-shore profiles are again low, but higher than for the analysed passes. Also, *MAE* values are larger, 34 and 19 cm for panels e and f respectively, pointing to the commented loss of agreement. Nevertheless, these differences of up to 34 cm between the TLS cross-shore profile and the smoothed ICESat-2 projected cross-shore profile are within the own variability of the beach. This means, that if the cross-shore profile is moved alongshore, the elevations are expected to change, and the profile to vary its shape, and the same is expected for the beach face, and therefore, for the beach face slope. This is concluded as well when analysing the beach face slope values given by the respective profiles in Table 5.2. Here, the beach face variations have led to a case where the extracted slope has the largest difference with the assumed true slope and the largest *PE*, 0.71 degrees (change of 1.2 cm/m) and 37.63% respectively. But this projection also led to the opposite case, where the beach faces are in really good agreement (see Figure 5.1, panel f, and Table 5.1), and therefore, the beach face slope is nearly the same, with a difference in degrees of 0.09 (change of 0.16 cm/m), and the lowest value of *PE*, 4.04 %.

Another observation that can be made from the presented figure and tables (Figure 5.1, and Tables 5.1

Table 5.1: Values of MAE, MSE and RMSE are presented in this table for the comparisons between ICESat-2 and CoastScan passes and cross-shore profiles.

Beam (pass/profile)	$MAE[m]$	$MSE[m^2]$	$RMSE[m]$
gt2r (pass)	0.09	0.01	0.11
gt2r (profile)	0.34	0.15	0.39
gt2l (pass)	0.15	0.03	0.18
gt2l (profile)	0.19	0.05	0.23

Table 5.2: Slopes for the different passes, in its dimensionless form and as degrees, as well as the differences between them and the PE are presented in this table.

Beam (pass/profile)	ICESat-2 $[/math>/^{\circ}]$	TLS $[/math>/^{\circ}]$	Difference $[/math>/^{\circ}]$	PE [%]
gt2r (pass)	0.0278/1.59	0.0311/1.78	0.0033/0.19	10.56
gt2r (profile)	0.0452/2.59	0.0328/1.88	0.0124/0.71	37.63
gt2l (pass)	0.0217/1.24	0.0196/1.12	0.0022/0.12	11.05
gt2l (profile)	0.0392/2.25	0.0378/2.17	0.0015/0.09	4.04

and 5.2) is that the projection of ICESat-2 passes into transects perpendicular to the coastline lead to a loss in agreement among profiles. Table 5.1 shows how MAE increases after the passes are projected, from 9 to 34 cm and from 15 to 19 cm. However, in Table 5.2 it is observed that this projection might lead to more or to less agreement between beach face slopes, showing how the PE values for the beach face slopes can be larger (for 'gt2r'), or lower (for 'gt2l') than the slopes computed from the passes. This behavior is attributed to the own beach variability. Therefore, even though the projection might lead to large errors on the cross-shore profile, the final beach face slope estimation might lead to closer values to the actual beach face slope. Additionally, low agreement between profiles or beach face slopes does not necessarily mean that they are not representative of the actual beach, but that it is not representative of the cross-shore profile which it is being compared to.

To clearly extract the main conclusions and evaluate the reliability of this section, it is important to acknowledge the following: first, the TLS point cloud was detrended, and second, the TLS data has been assumed as the ground truth, and this device itself is not perfect. For analysing the TLS data, the procedure for extracting the profiles was done twice, as explained in sections 3.2 and 4.1.1. The first time, the methodology was employed for detrending the TLS point cloud: the profiles shown in panels c and d of Figure 5.1 were obtained and compared. Then, the MAE was computed for each pair of profiles, and as a result, both profiles from the TLS were approximately 35 cm off, under the ICESat-2 profiles. This error is most likely because the inclination file, which for the scan of interest is corrupted, was not applied. To correct for this error, 35 cm were added on the vertical axis to each point of the point cloud. Then, the methodology is applied again using the corrected point cloud, and Figure 5.1 presents the corresponding results. The TLS data is an excellent dataset, with state-of-the-art accuracy and with relatively large spatial and temporal resolution. However, it can also contain errors and it is important to account for these when analysing the comparisons made.

Taking into account the above, it is concluded from this subsection that ICESat-2 passes capture the ground elevations with sufficient accuracy to extract beach features: beach profiles, beach face profiles, and beach face slopes. The comparisons done with the corresponding features from the TLS point cloud, show low values of MAE , MSE , and $RMSE$, as well as small errors and PE between slopes. Although, passes, when projected, lose information and the agreement between the projected ICESat-2 passes and the cross-shore profiles diminishes. However, the profiles still visually matches and the errors detected here are within a tolerance range that can be assumed in such a varying environment. Nevertheless, depending on the section of the beach the pass is in, and the cross-shore transect that the pass is projected into, the difference between the ICESat-2 extracted beach face slope and the TLS beach face slope, on the cross-shore profiles, can be larger or smaller than the differences from the passes. This means, that when ICESat-2 passes are projected into the cross-shore transects, two things may happen: either it is projected into a section of the beach with a different slope, leading to a big difference between slopes; or to a similar section containing a similar slope and therefore leading to

a good matching. Nevertheless, for both cases, the differences on beach face slope are relatively low and are within an expected variability of a beach with such conditions as the one of this case, with a relatively wide shore face and subjected to a relative energetic wave environment.

5.1.2. RTK-GPS

For this validation case, more attention is paid to the intertidal area rather than to the full profile because the RTK-GPS field survey was performed in February 2023 whereas the ICESat observations are from November 2019 (see subsection 4.1.2). The purpose of these fieldwork measurements was to assess ICESat-2 passes over the area 2 days prior. However, at moment of this writing, the ICESat-2 data has not been released. Therefore, because the paths followed for measuring also correspond to a previous ICESat-2 measurement, these passes are used for comparing with the RTK-GPS measurements. Nevertheless, due to the difference between measurements of more than 3 years (see Table 3.2), only the intertidal area is analysed for assessing how well the profiles relate to this section (from the manually defined instantaneous coastline of ICESat-2, up to 2.5 meters over the NAP) and how similar the beach face slopes are. In addition, these measurements were taken during different seasons, and therefore, the cross-shore profiles are in accordance to the different wave climates that they have been subjected to. Additionally, it is important to take into account the substantial angle between the ICESat-2 satellite's passes and the cross-shore transects they are being projected into (see Figure 3.6).

In Figure 5.2, panels a and b show the smoothed ICESat-2 passes, which are compared with the measured RTK-GPS profile. Despite the interval between measurements and their respective seasons, these profiles exhibit a significant level of agreement. However, when examining panels c and d, where the ICESat-2 passes are projected onto the cross-shore transect measured by the RTK-GPS device, a deviation is observed in the upper part of the profile. This discrepancy could be attributed to various factors. One possibility is the occurrence of an accretion process, most likely human-induced. Another potential cause is the geometric arrangement and distribution of dunes along the beach in relation to the angle of the satellite pass relative to the transect. Notably, the area with the largest disparity between the profiles is situated near the base of the dunes. This disparity in the projected profiles may arise from the satellite pass capturing an area where the dunes are closer to the ocean compared to the locations where the cross-shore RTK-GPS profiles were measured.

Finally, in the lower panels of Figure 5.2, the beach face profiles are presented. The agreement between the profiles of this section are assessed by computing the MAE , MSE , and $RMSE$, presented in Table 5.2. In this particular section spanning approximately 100 meters, the MAE is 24 cm for 'gt3r' and 32 cm for 'gt3l', indicating relatively low errors. Similarly, the MSE and $RMSE$ also exhibit low values. Moreover, comparing the beach face slopes derived from both cross-shore profiles reveals similarities in the differences between slopes and PE as observed in the previous validation dataset. Specifically, the difference in slopes amounts to 0.14° and 0.22° (changes of 0.24 and 0.38 cm/m), with PE values of 15.42% and 17.65% respectively. Therefore, not only do the profiles visually align, but the slopes derived from the demarcated area demonstrate comparable differences and PE values to those obtained in the TLS validation dataset.

Table 5.3: The MAE, MSE, and RMSE values for the comparisons between ICESat-2 and RTK-GPS passes and cross-shore profiles are shown here.

Beam	$MAE[m]$	$MSE[m^2]$	$RMSE[m]$
gt3r	0.24	0.09	0.29
gt3l	0.32	0.14	0.37

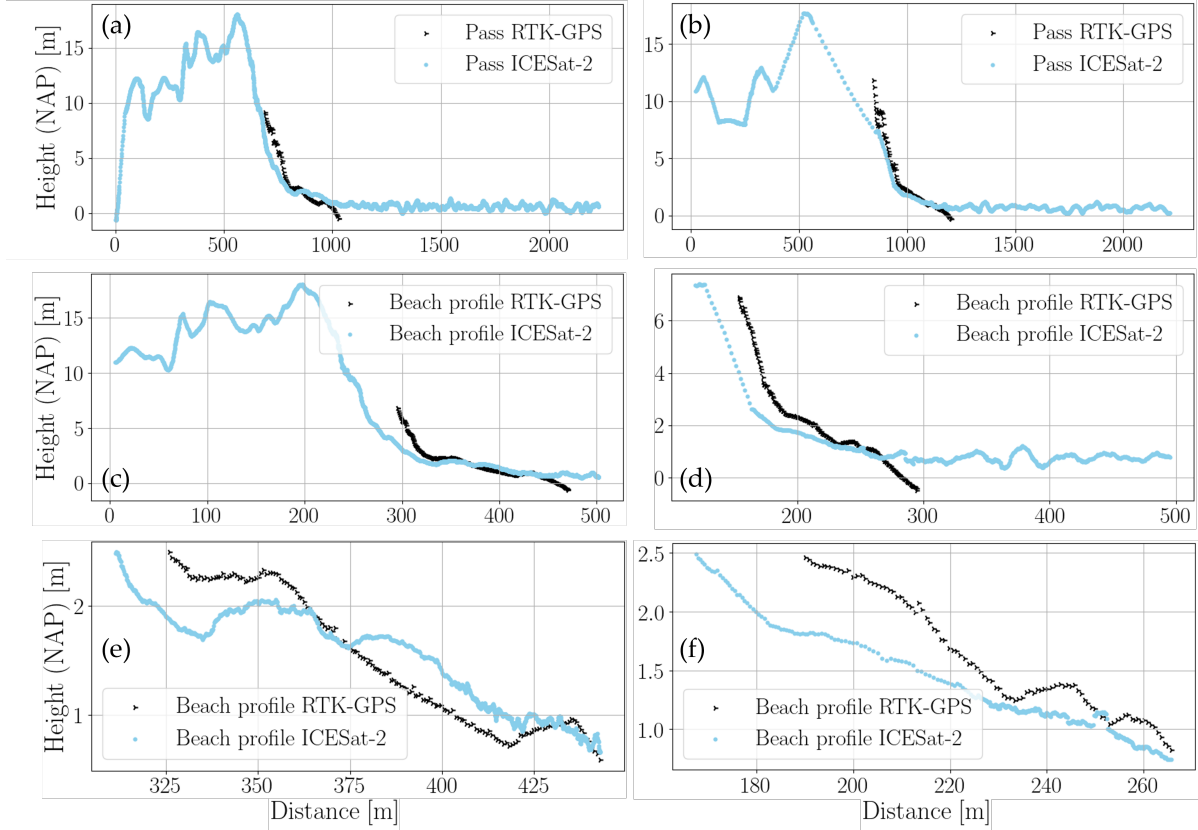


Figure 5.2: A comparison between the different profiles extracted from ICESat-2 and from RTK-GPS measurements. The profiles to the left (a,c,e) belong to the beam 'gt3r', while the profiles to the right (b,d,f) correspond to the beam 'gt3l'. The upper panels (a,b) show the points obtained after applying the moving average, with a windows size of 20 points, to the geolocated photons from ICESat-2 (red) and the corresponding profile from the TLS (black). Panels c and d contain the projected smoothed ICESat-2 passes and the cross-shore profiles measured with RTK-GPS. Finally, the lower panels (e,f) show the beach face of both ICESat-2 and RTK-GPS.

Table 5.4: Slopes for the different passes, in its dimensionless form and as degrees, as well as the differences between them and the PE are presented in this table.

Beam	ICESat-2 $\square/[\circ]$	TLS $\square/[\circ]$	Difference $\square/[\circ]$	PE [%]
gt3r	0.0138/0.78942	0.0163/0.9333	0.0025/0.14	15.42
gt3l	0.0178/1.0195	0.0216/1.2379	0.0038/0.22	17.65

From the results of this validation section, where 2 different validation datasets have been employed, different ideas and conclusions can be derived. First of all, ICESat-2 is able to extract beach features with relatively high accuracy with MAE values below the vertical accuracy given by the default uncertainties of ICESat-2, as shown in section 5.1.1. Secondly, with the results obtained up to this point it is concluded that ICESat-2 is capable of representing the beach profile even if they are projected into a perpendicular transect to the coastline, resulting in low values of MSE and $RMSE$, and values of MAE ranging from 9 to 34 cm. ICESat-2 is not only capable of resembling the beach profile with a relative large angle, but also the beach face slope, although it is not known yet to what extent this projection affects to the final cross-shore profile and subsequent beach face slope ICESat-2 beach face slopes have shown good agreement with the ones extracted from the validation datasets, with differences in degree below 0.71° and PE ranging from 4 to 38%. However, it can be also concluded, that when projecting the passes into the cross-shore profiles, spatial information is not enough and less agreement between profiles is observed. For understanding how the spatial geometry of beaches affect the direction of ICESat-2 passes, synthetic data was generated and the results are shown in the next section.

5.2. Synthetic ICESat-2 ATL03 data

This section presents the results concerning the effect that the angle between pass and transect has on the final beach profiles, beach face profiles, and beach face slopes. For assessing this impact, the creation of synthetic passes with different angles and distances to a cross-shore profile is necessary (see Figure 4.4). After generating the pseudo-geolocated photons, the water occurrence probability (WOP) layer (see section 3.4) is utilized for automating the comparisons and analysis (see Figure 4.5). To generate synthetic data, two beaches with distinct geometries are utilized. The analysis of these passes produces 3D mosaics, which can be used to determine how much agreement might exist between the assumed true transect and the synthetic pass based on the angle between pass and transect, as well as the intersecting point of the pass along the transect. To overcome the visual challenges in interpreting the mosaics, this section presents multiple examples representing different mosaic profiles. By showcasing diverse profiles from different parts of the mosaics, the analysis facilitates a clearer comprehension of the metrics variations and patterns within the mosaics, mitigating visual complexity and enabling the reader to better grasp the conclusions of this section.

Figures 5.3 and 5.4 show the beach profiles of both, the transect and assumed true beach profile, and the synthetic ICESat-2 pass projected onto the transect, for Ameland, Netherlands, and Marseille, France, respectively. The profiles taken as example are intersecting on the offshore section of the transect, approximately over the beach face, and onshore. For each intersecting point, with α being the angle between the transect and the projected pass, three different angles are used, 12° , 48° , and 72° . For the same profiles, the WOP layer is applied and the beach face profiles are presented in Figures 5.5 and 5.6 for the cases of Netherlands and France respectively. The agreement of both, the beach profile and the beach face profile are analysed by computing the *MAE*, *MSE*, and *RMSE*. Finally, from the demar-

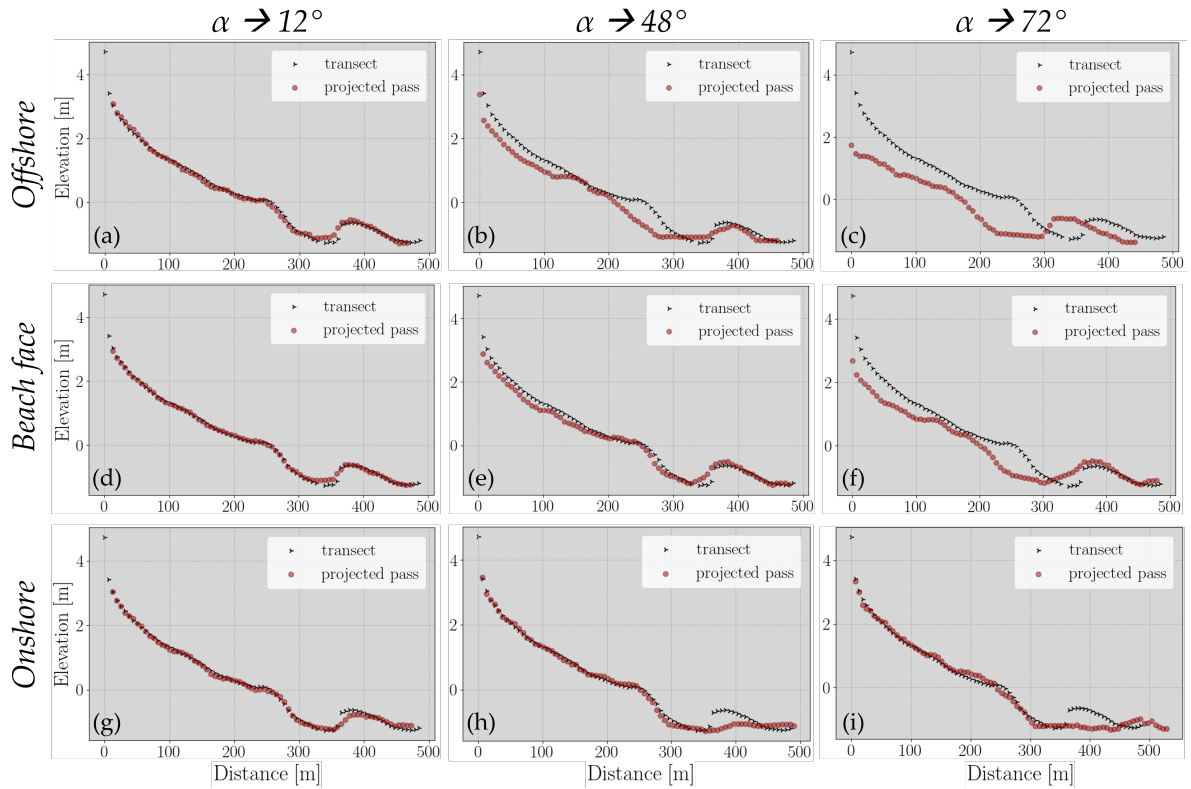


Figure 5.3: Comparisons between synthetic data and the assumed true cross-shore profile. It corresponds to the black profile, while the dark red profiles are the projected synthetic passes. The upper profiles are from passes that intersect on the offshore section of the transect, the middle ones intersect on the beach face section, and the lower panels on the most onshore section. Then, for the different intersection points, 3 different α —angle between transect and pass—are selected: 12° , 48° , and 72° .

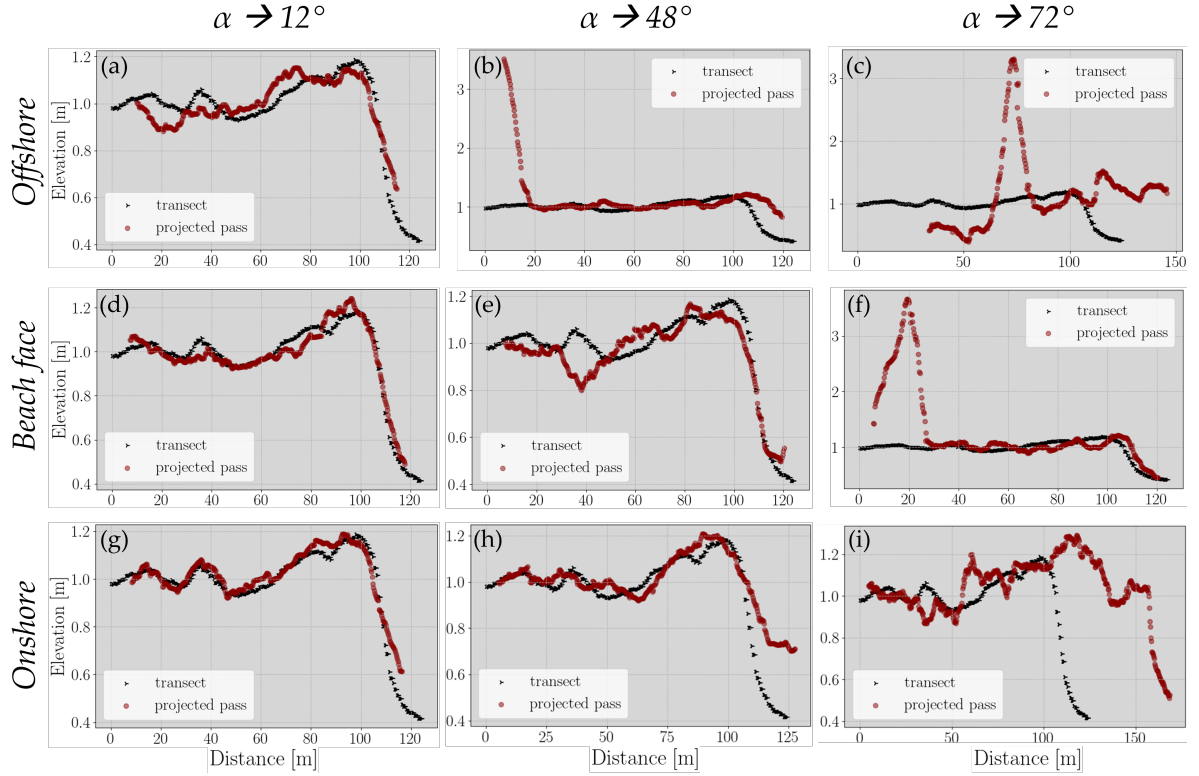


Figure 5.4: Different profiles for the beach in Marseilles, France. Three points are selected over the transect, on the onshore, beach face and offshore, and three passes with different angles intersecting over this area are chosen (12° , 48° , and 72°).

cated beach face profiles, the beach face slopes are extracted and the differences and percentage errors PE are computed for assessing their similarity.

First of all, the beach of Ameland, Netherlands, is analysed. This beach contains the most ideal beach geometry, a long, wide beach, with relatively low variability alongshore. Figure 5.3 shows that, in most cases, the profile maintains a similar shape up to an angle of $\alpha = 72^\circ$, with the exception of the pass intersecting offshore (panel c) where the upper part of the beach deviates from the projected pass.

While not much information appears to be lost after projecting the pass, there is variability in the lower part of the profile at 48 and 72 degrees. However, to some extent, the projected pass still represents the lower section of the cross-shore profile. This observation is further supported by Figure 5.5, where the beach face profile extracted with the WOP layer is representative of the beach face of the transect up to 48 degrees. Although slightly shifted to the left, the passes with $\alpha = 72^\circ$ also maintain a similar shape, suggesting a potential match in the slopes.

Table 5.5 presents the different values obtained for quantifying the similarity between profiles and beach face slopes. It is possible to see that for most of the shown cases, the MAE computed are below 30 cm for both profiles, the beach profile and the beach face profile, except for panels c and f. In general, MSE and $RMSE$ present low values resulting from a good agreement between profiles for most cases. Finally, this agreement is also translated to the beach face profile, as observed in the column with the differences in degrees, which are almost negligible. This leads to low PE that might be accounted as belonging to the own beach variability as seen in the result section of the CoastScan. From Table 5.5 and Figures 5.3 and 5.5 is possible to observe an increase in MAE , MSE , and $RMSE$ values, and visually, lost of agreement between profiles when increasing the angle. However, it does not translate to the beach face slope, with lower values of PE in profiles with high MAE values for example, or vice versa. To gain a deeper understanding of ICESat-2's performance on long beaches, the left panels of Figures 5.7, 5.8, and 5.9 are further analyzed later in this section.

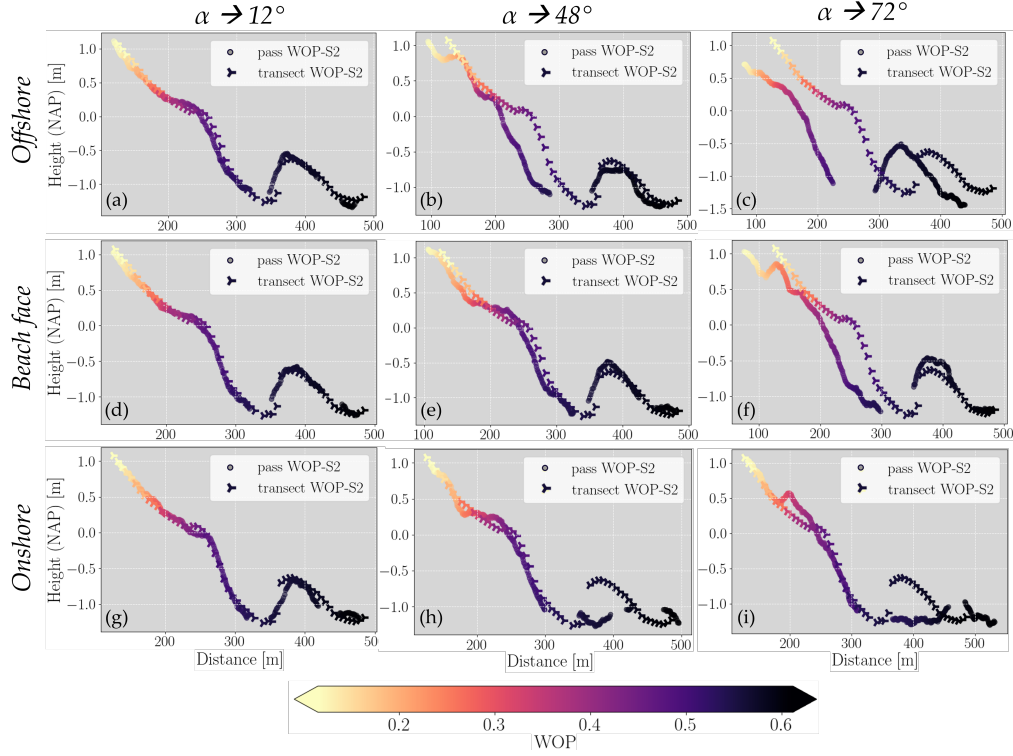


Figure 5.5: After applying the WOP layer to Figure 5.3 profiles (Ameland, Netherlands), the corresponding beach face profiles are extracted and presented in this figure. The WOP layer values are presented at the bottom of the image and it is given as probability.

Table 5.5: The differences between the profiles and slopes of Figures 5.3 and 5.5 in Ameland, Netherlands are presented here. It shows the *MAE*, *MSE*, and *RMSE* of the compared profiles for both, the beach profile (BP) and the beach face profile (BFP). Additionally, the BFP slopes are provided as $\tan\beta_T$ (true slope) and $\tan\beta_E$ (extracted slope), along with their differences in degrees. Finally, the *PE* are also given for the slopes.

	α [°]	MAE [m] BP/BFP	MSE [m^2] BP/BFP	RMSE [m] BP/BFP	$\tan\beta_T$ [°]	$\tan\beta_E$ [°]	diff [°]	PE [%]
Offshore	12	0.053/0.074	0.007/0.01	0.083/0.01	0.361	0.395	0.034	9.52
	48	0.276/0.222	0.131/0.105	0.361/0.305	0.361	0.36	0.002	0.43
	72	0.738/0.621	0.741/0.489	0.861/0.7	0.361	0.344	0.017	4.76
BF	12	0.035/0.057	0.003/0.006	0.055/0.078	0.361	0.372	0.011	3.17
	48	0.129/0.106	0.029/0.019	0.17/0.136	0.361	0.355	0.006	1.59
	72	0.383/0.267	0.278/0.136	0.527/0.368	0.361	0.315	0.046	12.7
Onshore	12	0.042/0.055	0.003/0.006	0.059/0.074	0.361	0.362	0.001	0.32
	48	0.111/0.148	0.029/0.044	0.171/0.211	0.361	0.35	0.011	3.17
	72	0.136/0.161	0.043/0.056	0.207/0.237	0.361	0.327	0.034	9.52

The findings that can be extracted from Figures 5.4 and 5.6 for the pocket beach in Marseilles, France, are similar to those observed in the previous analysis of Figures 5.3 and 5.5. However, in the full profiles shown in Figure 5.4, it becomes evident that the agreement deteriorates more rapidly as the angle between the pass and transect increases. This trend is also observed in the beach face profiles. Furthermore, there are instances where the synthetic pass lacks data for the beach face area. The profiles, when intersecting on the onshore and offshore sections of the transect, loose spatial information faster, this is, visually, the profiles do not match when intersecting far away from the beach face section. It is clear how variable alongshore this beach is with respect to the previous case. For the beach of Ameland, Netherlands, even for passes with larger angles, upper and lower sections of the profiles kept

some resemblance, opposite to what seen here, where for the last angle, 72° , the beach profiles are shifted or other beach features are projected onto the transect of interest.

When extracting the beach face profile for this section, it is observed that the applied WOP layer contains a narrower beach face profile, and only a few points contain WOP values. This is because of the small tidal range present on this beach, located in the Mediterranean Sea, which is an interior sea. Therefore, the width of the beach face and the elevation difference between upper and lower boundary of this are small. Furthermore, due to the variability of the beach and the narrow section of interest, the projected points fall outside the transect and there is no data for comparing. Then, if Table 5.6 is analysed simultaneously, it is observed that some of the PE values obtained are larger than most of the previously seen.

Table 5.6: This table summarises the differences between the profiles and slopes of Figures 5.4 and 5.6 in Marseilles, France. It shows the MAE , MSE and $RMSE$ of the compared profiles for both the beach profile (BP) and the beach face profile (BFP), as well as the BFP slopes, $\tan\beta_T$, the 'true' slope, and $\tan\beta_E$, the extracted slope, and its difference in degrees. Finally, the PE is also given for the slopes.

	α [$^\circ$]	MAE [m] BP/BFP	MSE [m^2] BP/BFP	RMSE [m] BP/BFP	$\tan\beta_T$ [$^\circ$]	$\tan\beta_E$ [$^\circ$]	diff [$^\circ$]	PE [%]
Offshore	12	0.071/0.081	0.009/0.008	0.093/0.09	1.507	2.251	0.745	49.43
	48	0.17/-	0.145/-	0.381/-	1.507	-	-	-
	72	0.407/-	0.401/-	0.634/-	1.507	-	-	-
BF	12	0.032/0.105	0.002/0.015	0.041/0.121	1.507	1.363	0.143	9.506
	48	0.059/0.06	0.006/0.005	0.076/0.067	1.507	1.489	0.017	1.14
	72	0.363/0.195	0.539/0.039	0.734/0.198	1.507	2.353	0.848	56.27
Onshore	12	0.032/0.061	0.002/0.004	0.046/0.065	1.507	1.524	0.017	1.14
	48	0.062/0.277	0.011/0.084	0.107/0.289	1.507	0.596	0.911	60.46
	72	0.107/-	0.056/-	0.238/-	1.507	-	-	-

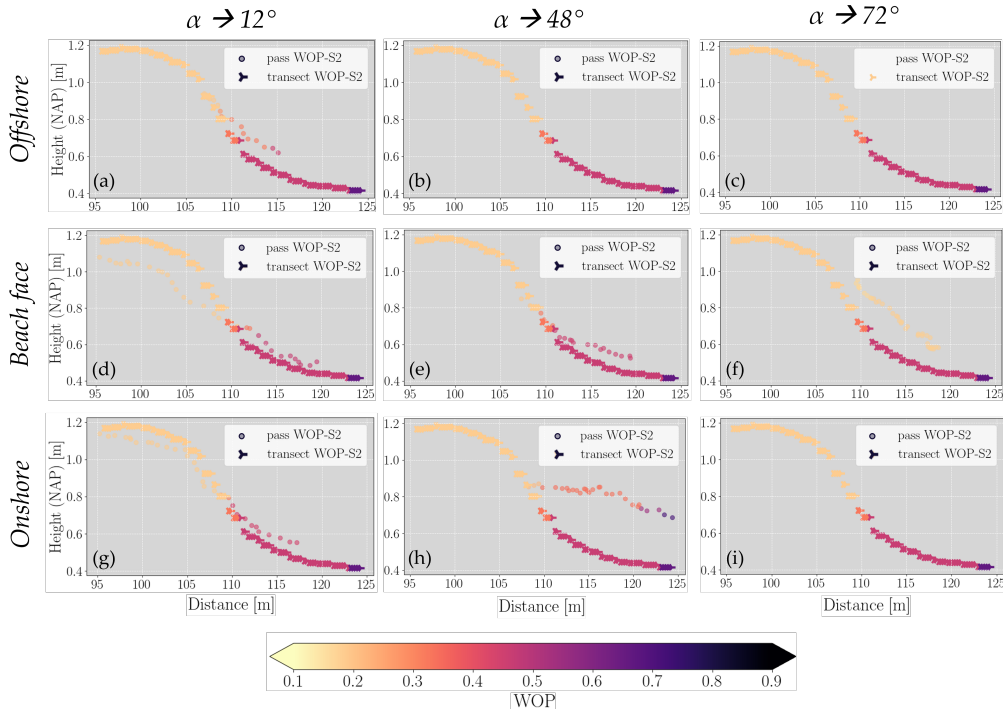


Figure 5.6: After applying the WOP layer to Figure 5.4 profiles (Marseilles, France), the corresponding beach face profiles are extracted and presented in this figure. The WOP layer values are presented at the bottom of the image and it is given as probability.

Figures 5.7 and 5.8 present the values of the MAE , MSE , and $RMSE$ for both beaches: the long, wide beach, Ameland (Netherlands), in the left panels, and the pocket-shape beach, Marseilles (France), in the right panels. These 3D mosaics present the changes on the values of the named metrics, based on the angle between pass and transect ($y - axis$, in degrees) and the intersection point of the synthetic pass over the transect ($x - axis$, in meters). Over each panel, a color bar indicating the direction of the transect is presented. In the left panels, the beginning of the transect was set in the offshore (dark blue), while for the right panels, the beginning of the transect is in the onshore section (yellow). In addition, the values for the statistics are presented in the interval from 0 to 1 for looking into possible patterns and comparisons between beaches instead of the maximum values of these metrics.

Figure 5.7 shows the values of the MAE , MSE , and $RMSE$ for the full profile, while Figure 5.8 focuses on the beach face profile after applying the WOP layer. For all cases of both, beach profiles and beach face profiles, as previously detected with the examples, an increase in the values is observed when the angle between pass and transect become larger. As expected, profiles loose agreement when the synthetic passes contain more spatial information from sections of the beach far from the transect of interest. This means, the further from the transect the elevations contained by the synthetic passes are, the larger the values of the mosaic become, leading to less agreement between profiles. Besides, it can be observed that the profiles that intersect with the transect on its offshore section seems to be in less agreement with the cross-shore profile than when the synthetic pass intersects with other sections of the beach. This is mainly due to the selected transect. The transect was drawn with the intention of positioning the beach face area somewhere around the center of the transect, but the given digital elevation models, DEMs, only comprise topography and they do not provide elevations below the beach face area. This means, that when comparing profiles of this section, the profiles do not contain information close to the transect and all the elevations are further away than for the synthetic passes intersecting on other sections of the transect, leading to profiles showing less agreement in this section.

Another pattern is observed in most of the mosaics, but it becomes more evident for the mosaics of the beach face profiles (Figure 5.8). The synthetic passes intersecting over the intertidal area retain the structure of the beach profile for larger angles than those passes that intersect on the offshore and onshore section. When analysing panels e and f of Figure 5.8, it is observed that the $RMSE$ values are lower around the center of the $x - axis$, this is, for the profiles intersecting on the beach face section, 250 to 450 m for Ameland Netherlands, and 80 to 150 m for Marseilles, France. Between the mentioned intervals, the $RMSE$ values remain relatively low even at large angles (75-80 degrees) for both beaches. The distribution of the metrics values on the mosaics follows a specific structure due to the derivation of elevations from synthetic passes closer to the actual beach profile. As a result, the beach face profiles from the synthetic passes bear a stronger resemblance the closer their intersection point with the transect is to the true beach face area.

Once the full profiles and beach face profiles of both beaches are analysed thoroughly, the beach face slopes are computed and compared to the slope extracted from the assumed true beach face profile. The results are presented again as 3D mosaics, but the metrics computed are the error —difference between the true beach face slope and the extracted from the beach face profile of the projected synthetic passes, in degrees—, and the percentage error, PE (see Eq. 4.6). From these mosaics, similar conclusions to those previously commented can be drawn. The beach of Ameland shows that the errors and the PE of the beach face slopes are relatively low up to an α of $70 - 80^\circ$, and the dependency on the distance from the pass to the transect —or intersection point of the synthetic pass over the transect— is also relatively low. However, for the beach of Marseilles, the errors and PE follow a pattern similar to the one described before, with lower values for both metrics up to large angles, $\sim 80^\circ$, when the intersection of the pass in the transect is within the beach face area, 80 to 150 meters in the $x - axis$. In general, the errors and PE are reasonably low up to approximately 60 degrees for most of the intersection points of the passes on the transect.

From the study of synthetic ICESat-2 ATL03 data over beaches with different geometries, different conclusions were derived and discussed. The conclusions can be summerised as follows: (1) The agreement between beach profiles, and the subsequent beach face profiles and beach face slopes are dependent on the angle between pass and transect, and in the distance of the pass to the transect, as well as in the

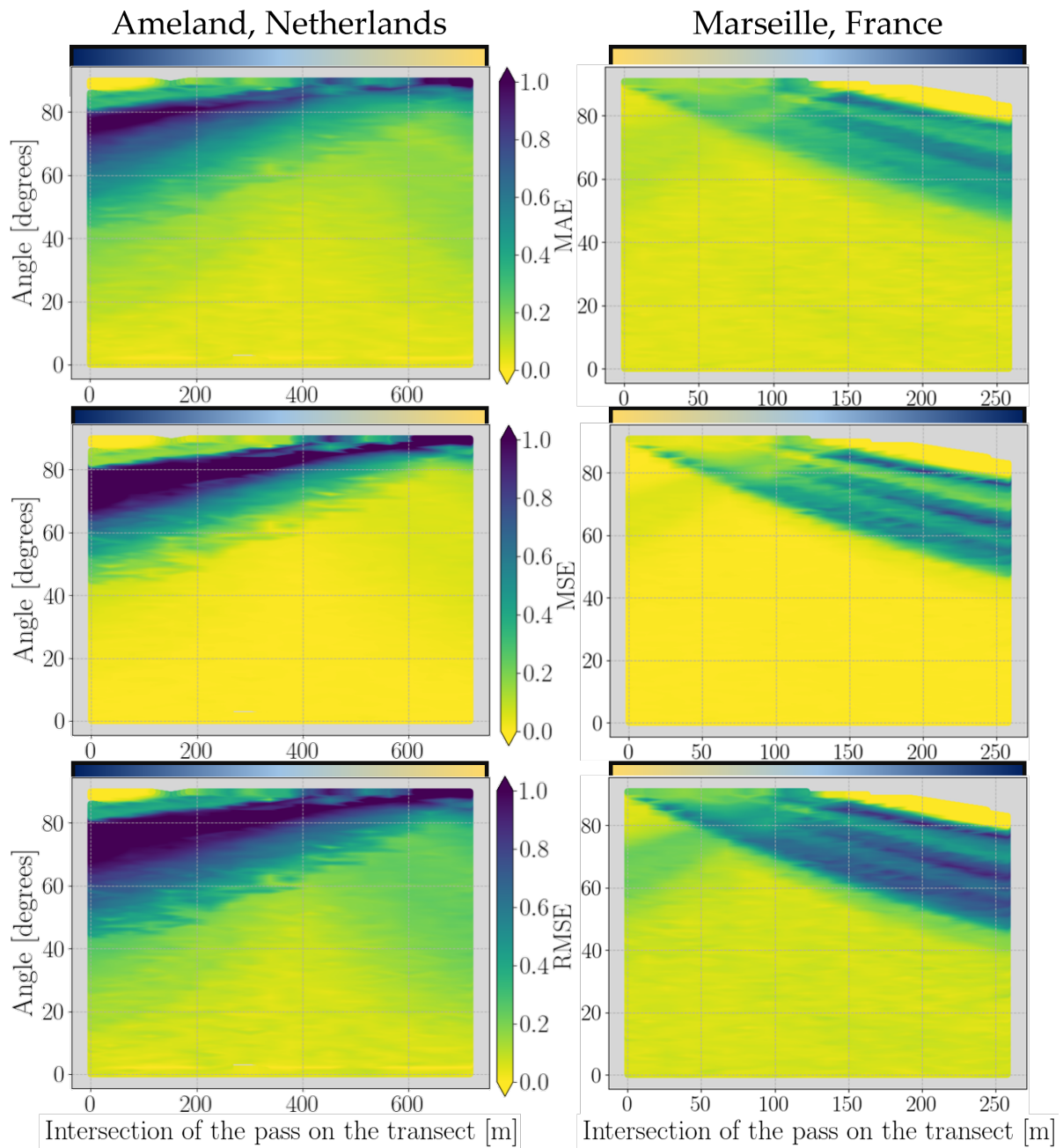


Figure 5.7: 3D representation of the different computed statistics, for the full beach profiles of both analysed beaches, Ameland in Netherlands (left) and Marseilles in France (right). The upper panels present the *MAE*, the middle ones *MSE*, and the lower panels the *RMSE*. In addition, over each panel there is a color bar indicating the direction of the profile, for the left panels, from blue to a soft yellow, this is, from ocean to land, left to right, and for the right panels in the other direction.

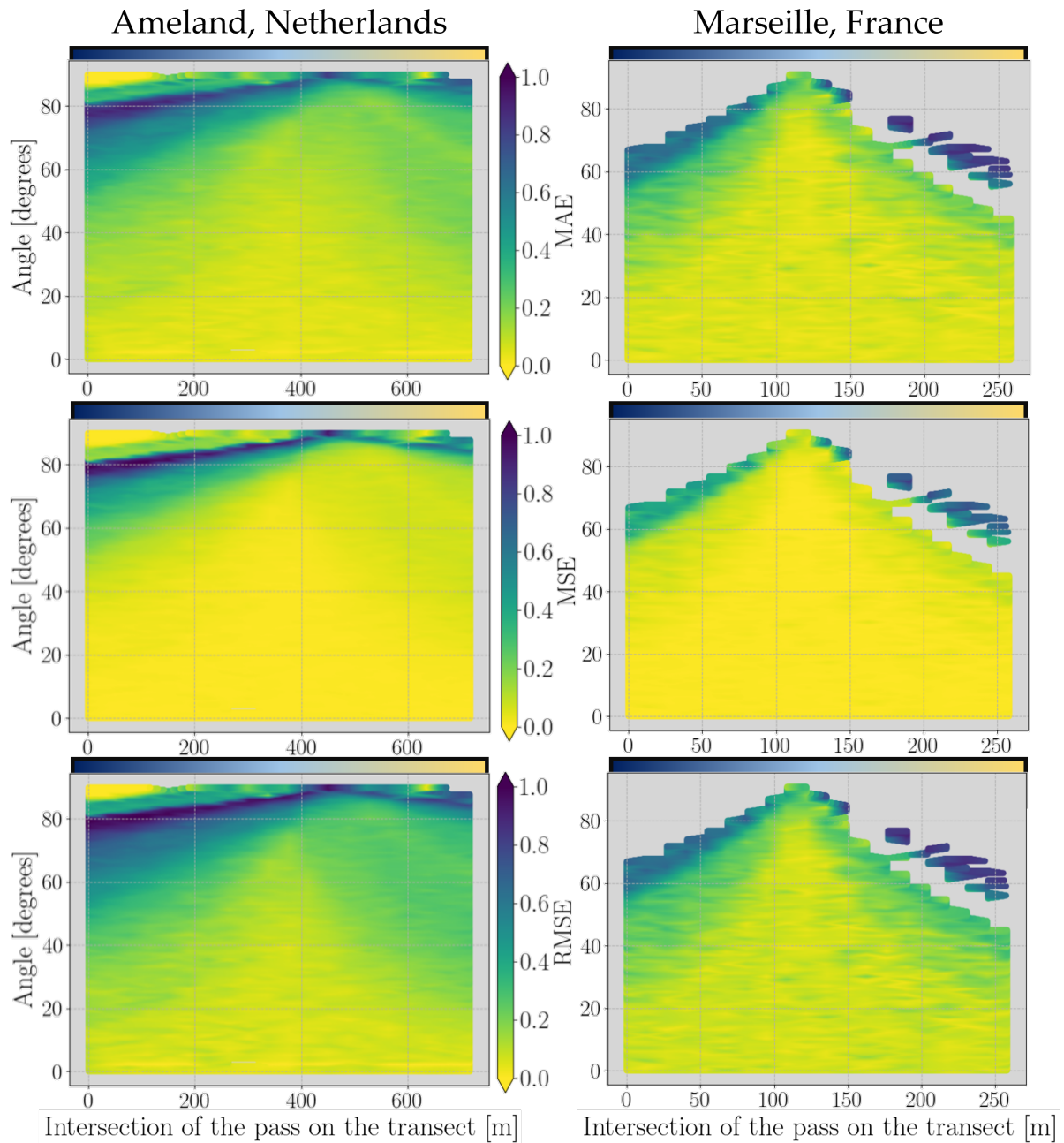


Figure 5.8: Similarly to Figure 5.7, this figure shows different statistics for both beaches of study, the *MAE* for upper panels, *MSE* for the middle ones, and the *RMSE* for the lower panels. Here, the color bars are also over each panel indicating the direction of the transect. From left to right, ocean to land for the left panels, and land to ocean for the right panels.

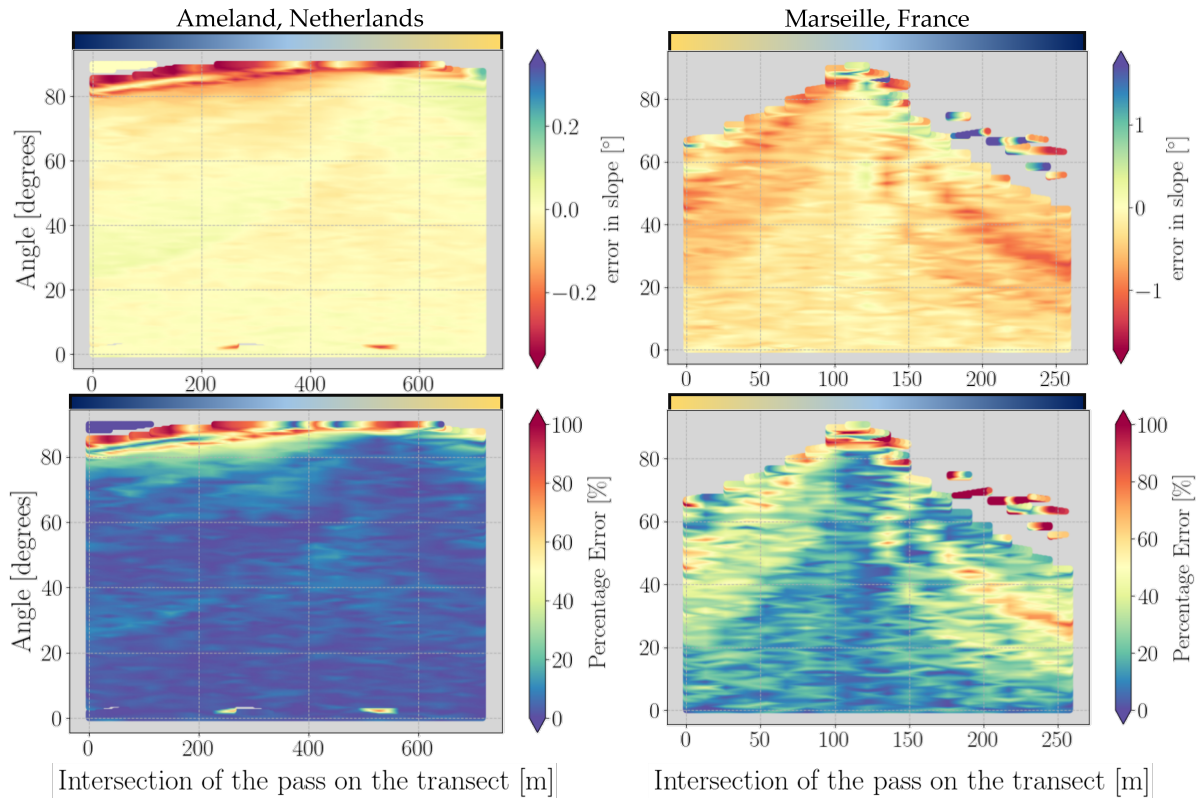


Figure 5.9: The errors between the assumed true one and the extracted from the synthetic passes are shown in the upper panels, while the lower panels present the PE . For the case in Ameland, Netherlands, see left panels, and right panels for Marseilles, France. Color bars over each panel indicates the direction of the transect. From left to right, ocean to land for the left panels, and land to ocean for the right panels.

geometry and variability of the beach; (2) For long wide beaches, with low variability alongshore, the beach face slope can be extracted with a PE value lower than 20% up to almost 80 degrees; (3) Smaller and narrower beaches, resembling a pocket beach, and more variable alongshore, are more sensitive to changes in angle, leading to larger PE values when α increases. For most of the passes, PE values lower than 40% can be found up to 60 degrees, what as concluded in section 5.1.1, falls within a reasonable tolerance range given by the own beach variability; (4) The closer the pass intersects over the center of the beach face, the closer all the elevations extracted from the pass are, and less spatial information is lost, leading to a more accurate beach profile and subsequent beach face profile and beach face slope up to larger angles.

5.3. Validation of methodology and ICESat-2 using JARKUS

The novel methodology presented in section 4.3, and schematized in Figure 4.6, is implemented. This upscaled approach allows to extract beach profiles, and subsequent beach face profiles and beach face slopes at a global level. For testing this automatised method, and assessing to what extent the beach face slope can be accurately estimated using it, the JARKUS dataset is employed. This dataset, as described on section 3.6, provides beach profiles on yearly basis along the entire coastline of continental Netherlands. Thus, this dataset provides a relatively high spatial and temporal resolution, which is essential for validating the extraction of beach profiles, beach face profiles, and slopes from ICESat-2 on a large scale. It enables a direct comparison of profiles from both datasets that correspond to the same year, facilitating comprehensive validation and analysis.

In Figure 4.6, where the methodology is presented, some requirements were not defined, the maximum angle between pass and transect, α , and the maximum distance from pass to the transect's centroid, d . Nevertheless, the results from section 5.2 yield an idea of reasonable values for this parameters, α and d .

Considering these results, in this section, the methodology is employed for three different cases, varying α and d , assuming that the more restrictive the case, the more accurate the final beach face slopes will be. Then, the three cases are: (1) no filters are used for ICESat-2 passes, therefore, each pass is linked to the closest transect, regardless of α and d ; (2) passes are filtered with $\alpha \leq 60^\circ$ and $d \leq 100$; (3) passes are filtered with $\alpha \leq 30^\circ$ and $d \leq 50$. For each case, a minimum number of photons per pass is required, this is, each pass has to contain more than 500 photons with quality flag 'High', to avoid processing passes with too many gaps due to noisy sections (clouds) and/or measurements with high quality photons too sparse. For cases (2) and (3), if more than one transect meets the requirements for the same pass, the nearest one is selected.

Figure 5.10 presents the α of the transects analysed on each case. The less restrictive case (1), panel a, where no filter is applied and therefore there are ICESat-2 passes linked to different transects throughout all the coasts of Netherlands, independently of α , the intermediate case (2), panel b, where $\alpha \leq 60^\circ$ and $d \leq 100$, and the more restrictive case (3), panel c, $\alpha \leq 30^\circ$ and $d \leq 50$. It is observed that the more stringent the case is, the number of filtered passes decreases, leading to a low number of passes in stretches of coast where the coastline is almost parallel to ICESat-2's orbit, as observed especially in panel c, where a large number of transects are discarded.

Respectively, in Figure 5.11, panels a, b, and c, represent the cases (1), (2), and (3). It is observed how in panel a, some beach face slope values greatly differ from the surrounding ones, reaching beach face slopes of up to 4 degrees. These values with substantial deviation are most probably because the employed algorithm fails to capture the actual beach face, and another section of the profile provided by ICESat-2 is being used for computing the slopes. It is observed that when more restrictive require-

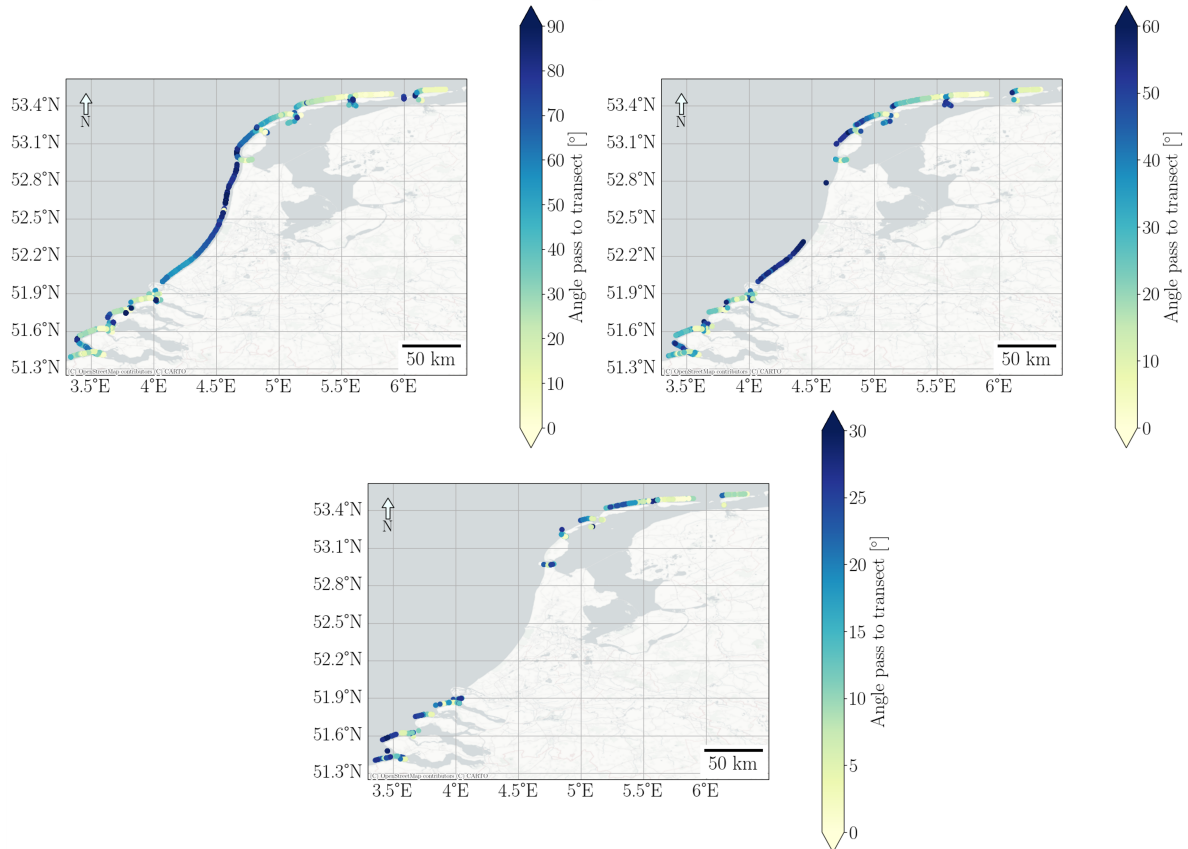


Figure 5.10: Angles between passes and the linked transects, α , are presented here as points over the centroid of the respective transects. In panel a the angles for all passes are shown, case (1). In panels b and c, the angles corresponding to the passes and linked transects meeting the requirements set for cases (2) and (3) respectively are presented ($\alpha \leq 60^\circ$; $d \leq 100$ and $\alpha \leq 30^\circ$; $d \leq 50$ respectively).

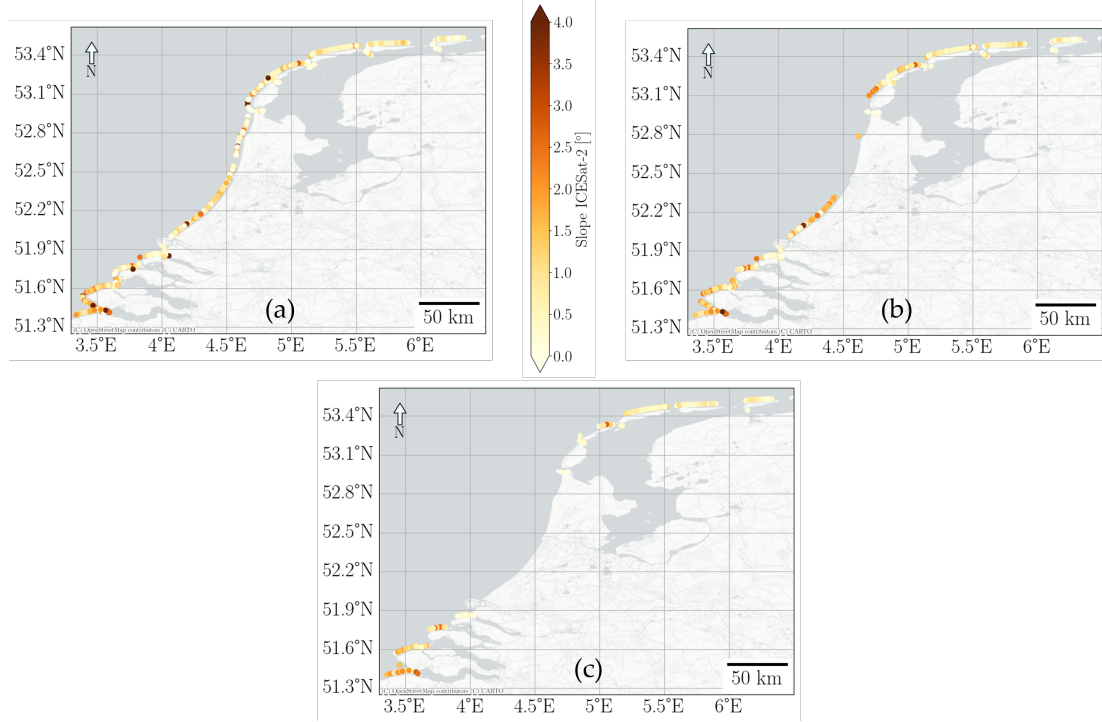


Figure 5.11: The beach face slopes estimated from ICESat-2 for the different cases are shown in this figure in the respective panels as Figure 5.10.

ments are used, these outliers disappear. However, this figure provides an example of how the beach face slopes would be extracted in coastal environments like The Netherlands without implementing a filter condition.

For assessing how realistic are the beach face slopes extracted, regression plots for each case are shown in Figure 5.12. These regression plots contains three panels, a, b, and c, which correspond for cases (1), (2), and (3) respectively. Each point represents the beach face slope value extracted from a beach face profile of ICESat-2 (x -axis) and the assumed true one, JARKUS (y -axis). Besides, each point is colored based on the angle between pass and transect, α . For further comparison, clarification and as visual aid, Figure 5.13 presents for the three cases the differences on beach face slopes between the extracted ones from ICESat-2 and the ones from JARKUS profiles (left panels), as well as the percentage error, PE (right panels).

If no filter is applied to the transects, case (1), the dataset consists on 4656 passes, from which 1904 passes can be processed. This is, 1904 profiles has data that can be projected into the transects of interest and therefore 1904 beach face slopes are extracted (see panel a in Figure 5.11). However, for this case, the less restrictive, the correlation between the assume true (from JARKUS profiles) and the extracted slopes (from ICESat-2 profiles) is weak, with a correlation coefficient, r , of 0.28. Regarding case (1), from panels a and b of Figure 5.13 it is also observed how the largest errors and PE values are found in the stretches of the coast corresponding to those with larger α . Then, when applying more restrictive conditions, cases (2) and (3) ($\alpha \leq 60^\circ; d \leq 100$ and $\alpha \leq 30^\circ; d \leq 50$ respectively), the number of passes meeting the requirements decreases, 1120 and 404 respectively, and therefore, the number of extracted slopes also decreases, 755 and 244 respectively. However, the correlation coefficient increases, with a r of 0.49 for case (2), and of 0.64 for case (3). This improvement in the correlation between slopes can be observed in the corresponding panels of Figure 5.12, b and c, where more visual correlation is observed. This is also observed in the respective panels of Figure 5.13, c, d, and e, f, where the errors and PE are comparatively smaller with fewer outliers for case (2), and even smaller values and fewer outliers for case (3). Nevertheless, the panels of Figure 5.13 reveal that despite the smaller errors and reduced values of PE , a significant number of passes are lost, resulting

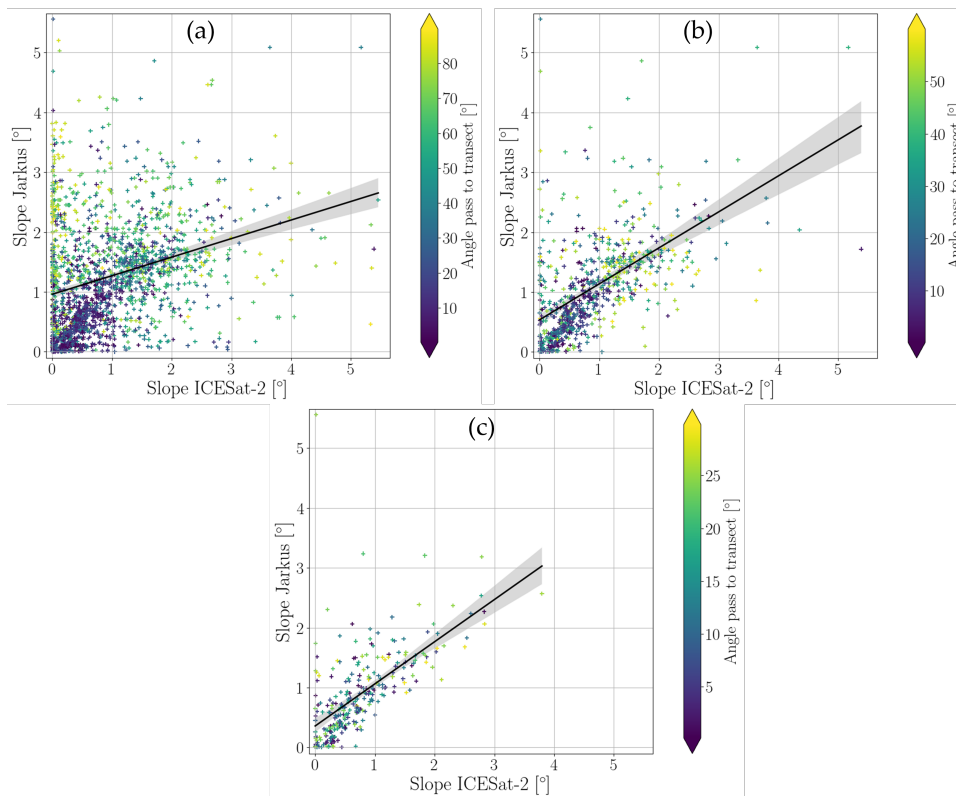


Figure 5.12: Regression plots for the beach face slope values: ICESat-2 (x - axis) and JARKUS (y - axis). The three different cases of study (1), (2), and (3) are displayed in panels a, b, and c respectively. Each point is colored based on the angle between the pass and the linked transect, α .

in extensive stretches of coastline without extracted beach face slopes. This implies that as the imposed requirements become more stringent, a greater amount of information is sacrificed, particularly in sections of the coastline that align with the orientation of ICESat-2's orbit, and therefore, its profiles.

Lastly, following the presentation and brief discussion of the results concerning the validation of the methodology and ICESat-2 beach face slope extraction using the JARKUS dataset, additional examples are provided in Figure 5.14. These profiles serve to facilitate further discussion, enhance clarity, and offer visual illustrations of potential shortcomings, successes, and potential improvements of the methodology, as well as to show the wide range of profiles that ICESat-2 may provide. Each panel provided on this figure shows the projected ICESat-2 profile (orange dots), the corresponding moving average of the geolocated photons, with a windows size of 20 points, and in brackets the angle between pass and transect is shown (blue line). Besides, it also presents the transect, into which the photons are projected, and it contains the JARKUS profile used for visual comparison (yellow line). Then, the algorithm finds the beach face profile (BFP) in both profiles, the assumed true profile (JARKUS, in green) and the extracted from ICESat-2 (IS-2, in black).

Figure 5.14 shows different profiles, in some of them the beach face area seems to be correctly extracted and both (JARKUS and IS-2) correspond to each other, leading to similar beach face slopes (panels a and b). In panel c, the existence of channels or wet sections on the beach can result in the incorrect categorization of photons as high quality. Visually, the beach face slopes may appear similar, but in comparable scenarios, minor variations in the selection of the beach face can lead to significant differences in slope between profiles, despite the overall agreement among the profiles themselves. Panel d is an example of how ICESat-2 is able to correctly represent the beach profile, as well as the beach face profile and subsequent beach face slope even for large angles (52.89°). Despite the beach face profile being shifted due to the beach geometry, there is visible agreement between both profiles. Furthermore, the selected beach face areas seem to lead to similar values of beach face slope. Moreover, this is a case

where the ICESat-2 profile seems to not contain photons before it reaches the coast, most likely due to cloud coverage. Then, for cases where ICESat-2 was not able to capture the elevations on the previous 5 km off coast, the methodology created by Ma et al. [15] —which needs the geolocated photons within 1 to 5 km offshore for estimating the coastline— would not be able to extract the beach face slope, and valuable information would be lost. Therefore, for coastal sections with a substantial cloud cover percentage, the usage of their methodology, would result in the loss of numerous passes resembling those illustrated in panels a, d, g, and h, where there is no data offshore. Consequently, the key parameter would also be lost, even though ICESat-2 might have effectively covered the area of interest.

Panels e and f present profiles where ICESat-2's profile and beach face profile seems to visually represent the true profile and beach face profile, but some deviations might be observed. In panel f, even though the profiles are not completely overlapping, it is observed that the resulting beach face slopes are most likely almost identical. This is because it seems that the first and last elevation of both beach face profiles are the same for both sources, ICESat-2 and JARKUS. However, when analysing the beach face profiles of panel e, the beach face slope extracted from ICESat-2 is not going to be representative of the beach face slope from JARKUS. There could be two reasons for this and similar cases: first, due to the angle of the pass, the measured section is steeper than the cross-shore profile presented by JARKUS. The second option is the difference in time between profiles, while JARKUS is usually measured on summer, it contains an upper berm that ICESat-2's profile does not present because the coast might have been subjected to a different wave regime. Finally, in Figure 5.14, panels g and h show cases where the implemented methodology fails to extract the beach face profile, and therefore the beach face slope greatly differs from the slope extracted from JARKUS profile. It is observed how for both cases, the geolocated photons are quite spread over the y - axis, leading to wrong extractions. See Figure A.1 in Appendix A A for more examples.

It is concluded that this novel methodology allows to extract profiles perpendicular to the coastline from ICESat-2 ATL03 geolocated photons at a large scale and it can be implemented at a global level. However, because the extraction of the beach face slope is not trivial, it is not always correctly estimated. The variety of reasons that might lead to these incorrect estimations are:

- For cases where ICESat-2 ATL03 data is nonexistent over the ocean section, the MSL will be incorrectly extracted and the beach face profile will most likely be higher than it should.
- The presence of large waves might lead to a poorly selected beach face area that can fall even in the ocean section of the profile.
- Channels on the beach face with water can create artifacts such as the one shown in panel c of Figure 5.14, what can lead to incorrect beach face slopes. Nevertheless, in general these channels will be avoided because the algorithm finds the lower boundary of the beach face and then the upper boundary is set by adding 2.5 meters. Therefore, because the artifacts are within a channel, the upper boundary will be most likely selected before the channel or after, and therefore the upper boundary will belong to the profile, and not to the artifact.
- Some passes contain information within the transect that they are projected into, but there might be small gaps without geolocated photons over the beach face, leading to a poor moving average of the profile extracted from ICESat-2, and depending on the size of the gap, a non-representative beach face slope.
- If the passes are measured with high tide, the beach face extracted will be located higher on the cross-shore profile due to the higher definition of the MSL, and therefore of coastline.

The above listed items are possible sources of errors for extracting the beach face slope. However, in this section other errors are found when comparing the extracting beach profiles, beach face profiles and beach face slopes. These lack of agreement between JARKUS and ICESat-2 on these beach features does not necessarily mean that ICESat-2 is not able to capture them correctly, but that they do not correspond to the exact cross-shore profile given by JARKUS. These differences between these features might be due to:

- Highly variable beaches alongshore, or intricate geometries. It does not mean that ICESat-2 is not able to correctly capture the beach face slope, but that the obtained beach face slope is representative of another cross-shore profile.

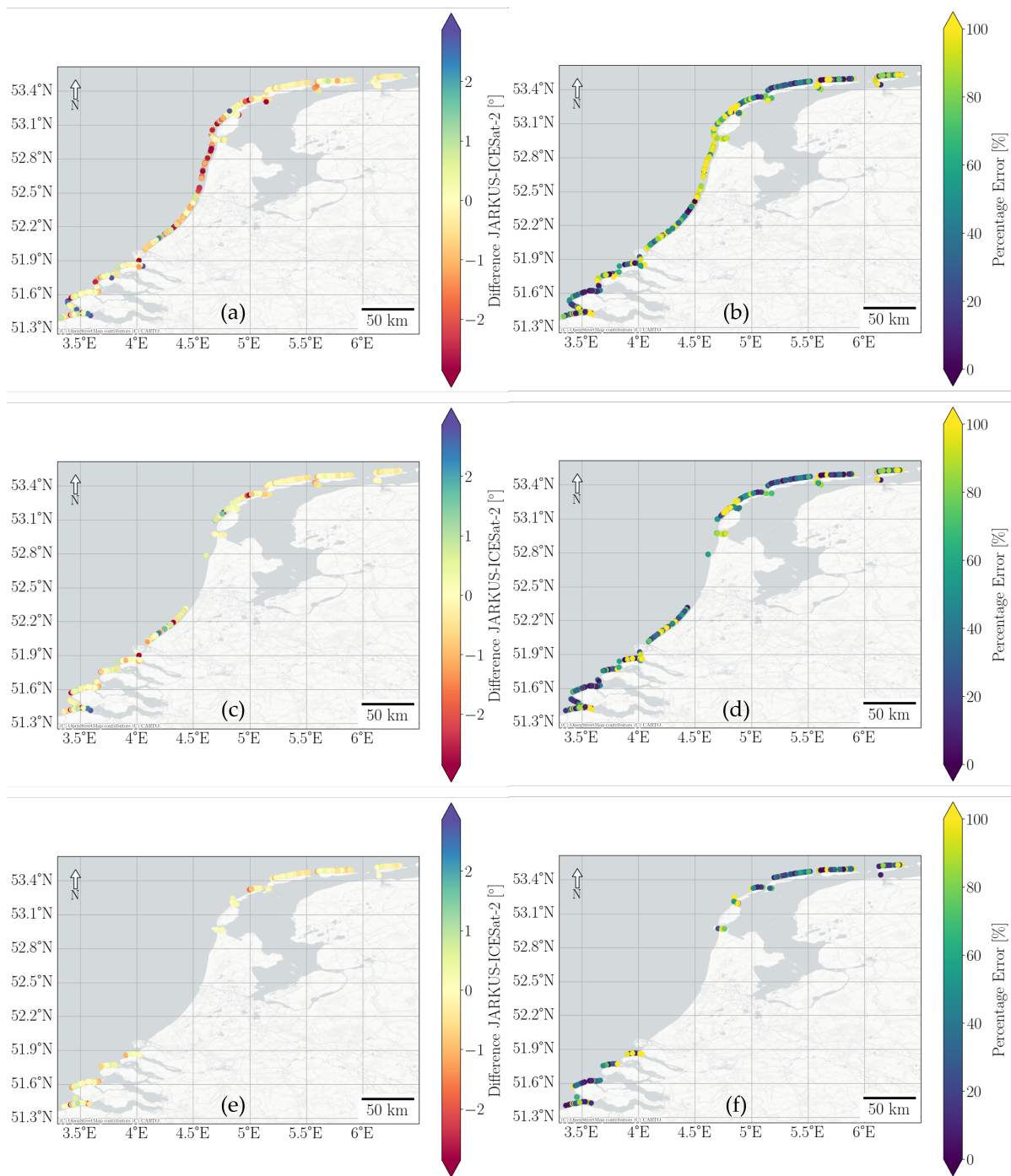


Figure 5.13: In this figure, the differences on beach face slopes between the ones extracted from ICESat-2 profiles and the ones from JARKUS profiles, as well as their percentage errors, PE , are presented. These are presented for all three cases: panels a and b for all the linked passes, c and d for the passes meeting the requirements of α below 60 degrees and d smaller than 100 meters, and finally, panels e and f show the most restrictive case, where the passes are below 30 degrees of angle between pass and transect and the distance from pass to centroid of the transect is under 50 meters.

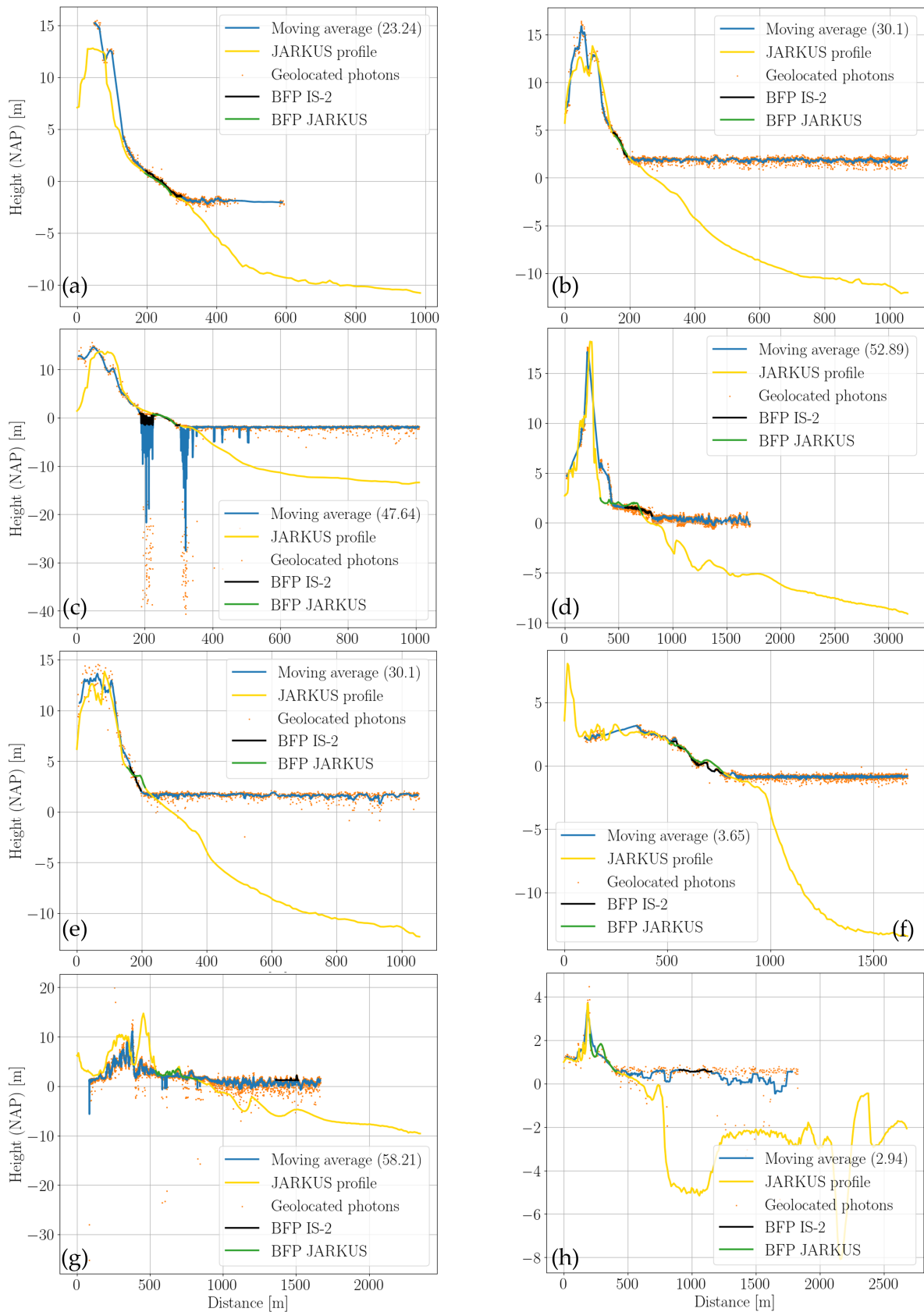


Figure 5.14: Profile examples from the implemented methodology for upscaling the beach face slope extraction at a global level (see section 4.3). This methodology has been tested using JARKUS dataset. The panels show the geolocated photons of ICESat-2 after projecting them into the transect (orange points), the corresponding moving average of these photons, with the angle between pass and transect, α , in brackets (blue line), and the profile provided by JARKUS (yellow line). In addition, the panels also contain the beach face profiles of both, the profile extracted from ICESat-2, BFP IS-2 (the moving average, blue line), and the JARKUS profile, BFP JARKUS, represented with a black and green line respectively.

- Large angle between pass and transect, α . The larger α is, the most likely is to run with some artifacts on the beach, capture different features that might not seem to belong to the beach and can cause problems to the employed algorithm to find the beach face, or even not contain the beach face.
- Different artifacts might appear due to beach houses, groynes, dikes, ports, and more human objects over the beach face.

To sum up, it is observed that the process for extracting beach face slopes can be upscaled, and an interesting and useful byproduct can be correctly extracted at a global scale, the cross-shore profile. However, the extraction of the beach face slope can be further polished. The main source of error for extracting this parameter is the correct demarcation of the lower and upper boundary of the beach face, and it is not trivial. Ma et al. [15] developed a methodology that uses ICESat-2 ATL03 and ATL08 data for extracting the beach face slope. In their methodology, the sea side within 5 km to 1 km is selected and the geolocated photons are used for calculating the local mean sea level (MSL) by averaging the elevations, H_{sea} , and define the wave height as the standard deviation of the geolocated photons within the corresponding interval, σ_{sea} . Then, they set the lower and upper boundary of the beach face as $H_{sea} + 2 * \sigma_{sea}$ and 1 m above the MSL, $H_{sea} + 1$.

Their methodology is able to extract beach face slopes and present some insights on how to work with ICESat-2 profiles on coastal environments, but it has some flaws. One of these flaws has already been commented: the lack of data within the interval used for computing the H_{sea} and σ_{sea} leads to discard valuable profiles. Furthermore, in the profile examples shown in Figure 5.14, it is observed that in some cases, the spread of the geolocated photons on the sea is quite large. Then, for cases where $\sigma_{sea} \geq 0.5$, the upper and lower boundary of the beach face will be the same height or the elevation of the upper boundary will be smaller than the elevation of the lower boundary, what is unrealistic. Moreover, for cases of standard deviation smaller than 0.5, the difference in elevation between the demarcated lower and upper boundary might be relatively small, what can lead to not being representative enough of the beach face.

The methodology developed here only uses ATL03 data, and similarly, it has as first objective to find the local MSL, what would allow to demarcate the lower boundary of the beach face. The difference from the methodology of Ma et al. [15] is that because the ATL03 data has been clipped to the coastal buffer the ICESat-2 pass is divided in 5 sections and the most offshore is taken. From here the standard deviation of that section and the MSL are computed. Then, as described in section 4.3, the position of the coastline can be located. This methodology avoids the necessity of having information far away from the area of interest, and the wave and tide conditions on the area might produce a better estimate of the local MSL. Furthermore, in the developed methodology, before computing the standard deviation, a buffer is created around the MSL, based on a primary standard deviation, and from the kept geolocated photons, another standard deviation, which is equivalent to σ_{sea} of Ma et al. [15], is computed, avoiding possible outliers.

5.4. ICESat-2 on coastal areas world-wide distribution

This section displays a comprehensive analysis of ICESat-2 ATL03 measurements in coastal regions, considering both spatial and temporal aspects. To accurately examine the behavior of ICESat-2 along coasts, it is necessary to process all available ICESat-2 data collected in these areas. The processing task is substantial due to the varying factors that affect ICESat-2 measurements, such as nadir off-pointing during the initial two years, cloud coverage, and the influence of sunlight on the photons. Consequently, ICESat-2 measurements might not present an easily detectable pattern over the world coastlines. In order to handle this large volume of data, the methodology described in section 4.3 and illustrated in Figure 4.6 is partially employed. The data analysed encompasses the period of time from the launching of the satellite, September 15th, 2018, to October 12th, 2022.

The data within the inner box of this methodology is downloaded and analysed. These boxes of 20 km^2 , as described, are generated from the centroid's transect of the system of transects used for upscaling the method. Currently, the methodology is running globally for populating the coasts of the world with

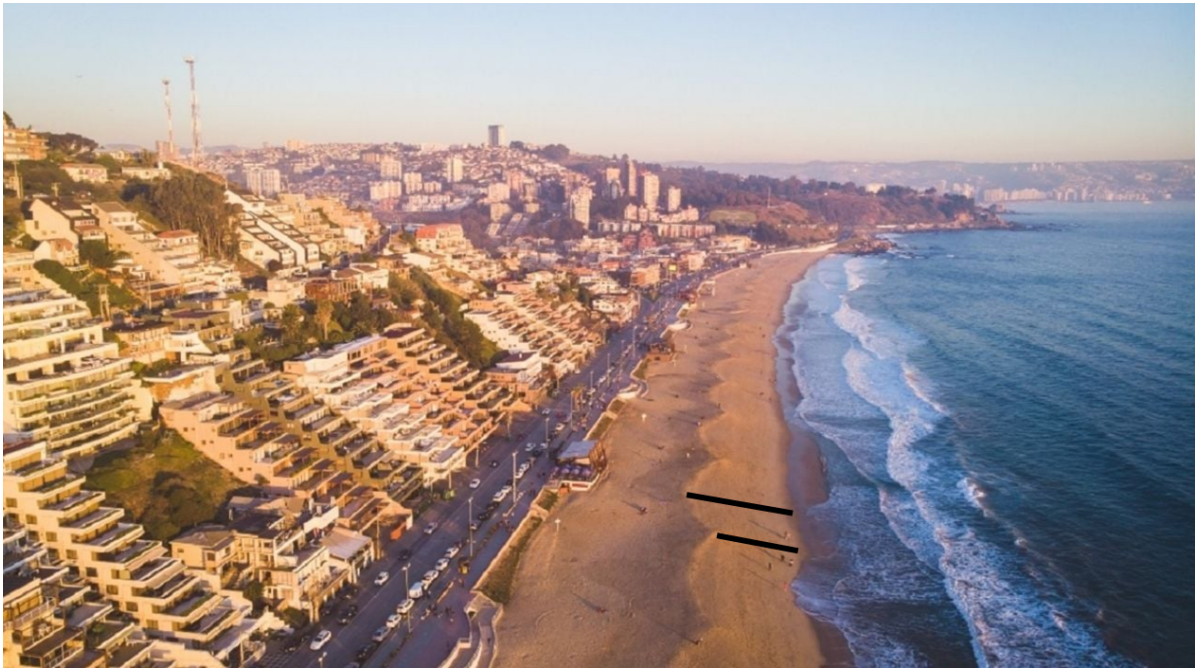


Figure 5.15: Example of different beach face profiles (black lines), and consequently beach face slopes, within the same beach, in Refiaca, Chile.

ICESat-2 passes and analysing the amount of passes over these boxes of 20 km^2 (the inner buffer shown in Figure 4.6). Not only the number of passes are obtained, but also the number of photons per box and the ratio of high quality photons. Furthermore, the dates of passes (at least 1 beam of the satellite has measured within the box of study) are filtered by amount of photons with high quality (> 5000) in order to ensure that at least one of the passes contain enough high quality photons. These are counted as valid dates and it gives an idea on how many dates are most likely to be able to provide at least one beach face slope measurement. The elaborated methodology is currently being implemented for the globe, which requires downloading and processing an enormous amount of data throughout the coasts of the whole world, therefore, this section is exploratory, analysing the data processed up to date. Therefore, this section is merely a glimpse into ICESat-2 ATL03 data distribution throughout the world coastlines and helps to understand to what extent this data could be used for monitoring beach face slopes, as well as what are the opportunities and limitations of upscaling the beach face slope extraction using similar LiDAR-based satellites.

Firstly, a small global sample of boxes of 20 km^2 are selected from different parts of the world. This selection aims to provide readers with an understanding of the information extracted from these specific areas and whether any discernible patterns or behaviors can be observed based on their geographical locations. The sample's locations are illustrated in Figure 5.16, depicting a total of 12 distinct areas as black dots. The values extracted from this analysis are provided in Table 5.7, moreover, for a visual aid of the distribution of the different indicators, colored maps are presented in Figures B.1, B.2, and B.3 on Appendix B. This table, besides of the location of the box, presents: (1) the number of photons, (2) the ratio of high quality photons [%], (3) number of dates that ICESat-2 measured the box, (4) number of dates that the measure lead to more than 5000 high quality geolocated photons, (5) the ratio of these 'valid' dates [%], (6) number of passes, (7) the number of passes considered as 'valid' passes, this is, passes with more than 500 high quality photons, and (8) the ratio of these valid passes [%].

Figure 5.17 presents the amount of photons per ICESat-2's measured date for half of the selected locations: Australia, Brazil, Canada, Japan, Namibia, and Netherlands. Furthermore, the bar provided for each date is divided, and each section colored, based on the amount of photons of the date classified as 'Noise', 'Buffer', 'Low', 'Medium', and 'High'. It allows to analyse the amount of times that ICESat-2 has flown over the box in 5 year. It also allows to observe how varying ICESat-2 measurements can

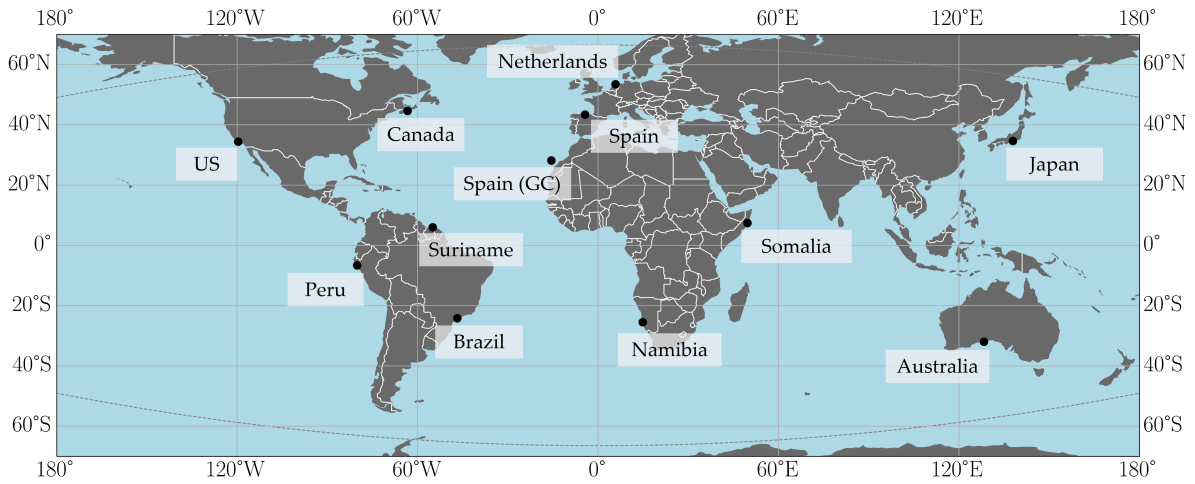


Figure 5.16: Locations of a sample of boxes taken as examples for analysing how ICESat-2 behaves inside boxes of $20km^2$.

Table 5.7: a sample of boxes taken as examples for analysing how ICESat-2 behaves inside boxes of $20km^2$. See locations in Figure 5.16.

Location	# photons	Ratio of high quality photons [%]	# dates	# of dates with ≥ 5000 high quality photons	Ratio of 'valid' dates [%]	# passes	# of passes with ≥ 500 high quality photons	Ratio of 'valid' passes [%]
Spain	4476214	17.71	33	15	45.45	121	67	55.37
Somalia	3859946	39.42	28	22	78.57	130	97	74.62
Namibia	4560243	42.49	30	23	76.67	120	87	72.5
Brazil	3433261	19.57	31	17	54.84	126	69	54.76
Peru	3140065	22.18	28	12	42.86	119	50	42.02
US	4880644	27.54	26	23	88.46	106	88	83.02
Netherlands	2172233	63.97	32	22	68.75	118	89	75.42
Spain (GC)	5268872	18.3	35	22	68.75	152	86	56.58
Suriname	4118147	45.48	29	20	68.97	129	89	68.99
Australia	3267175	42.37	30	18	60	109	75	68.81
Canada	4563209	41.08	34	19	55.88	126	83	65.87
Japan	3401445	26.12	31	18	58.07	123	77	62.6

be depending on the location that these are taken, regarding not only amount of photons but also their quality. Besides, because ICESat-2 is weather dependant, Figure 5.18 is added for comparing the selected locations with the coastal cloud coverage obtained from the optical imagery of Sentinel-2 analysis by Bergsma and Almar [54].

When evaluating simultaneously the values from the different locations of Figure 5.16, in Table 5.7, as well as the examples of the distribution of dates on Figure 5.17, with the Sentinel-2 cloud coverage map (see Figure 5.18), it is observed that even though it is known that the cloud coverage is a limitation for ICESat-2 measurements, the selected sample does not exhibit complete correlation with the cloud cover depicted in Figure 5.18. Consequently, upscaling the methodology is necessary for a better understanding and a broader perspective of ICESat-2 measurements on coastlines at a global level. Nonetheless, the information extracted from this analysis offers insights into the expected outcomes.

Due to ICESat-2's orbit configuration, and the systematic off-nadir pointing during the first two years, different amount of passes are expected based on the latitude of the box. More passes are expected for higher latitudes, whereas boxes in lower latitudes are likely to contain fewer passes. However, there are some interesting observations when comparing specific regions. For instance, in high latitudes with relatively high median cloud coverage like the Netherlands, the number of photons within a $20km^2$ box is relatively low, the lowest of the presented examples, compared to similar regions like Canada. Furthermore, boxes with a larger amount of photons than Canada are found in mid and lower latitudes such as Spain (GC) and US.

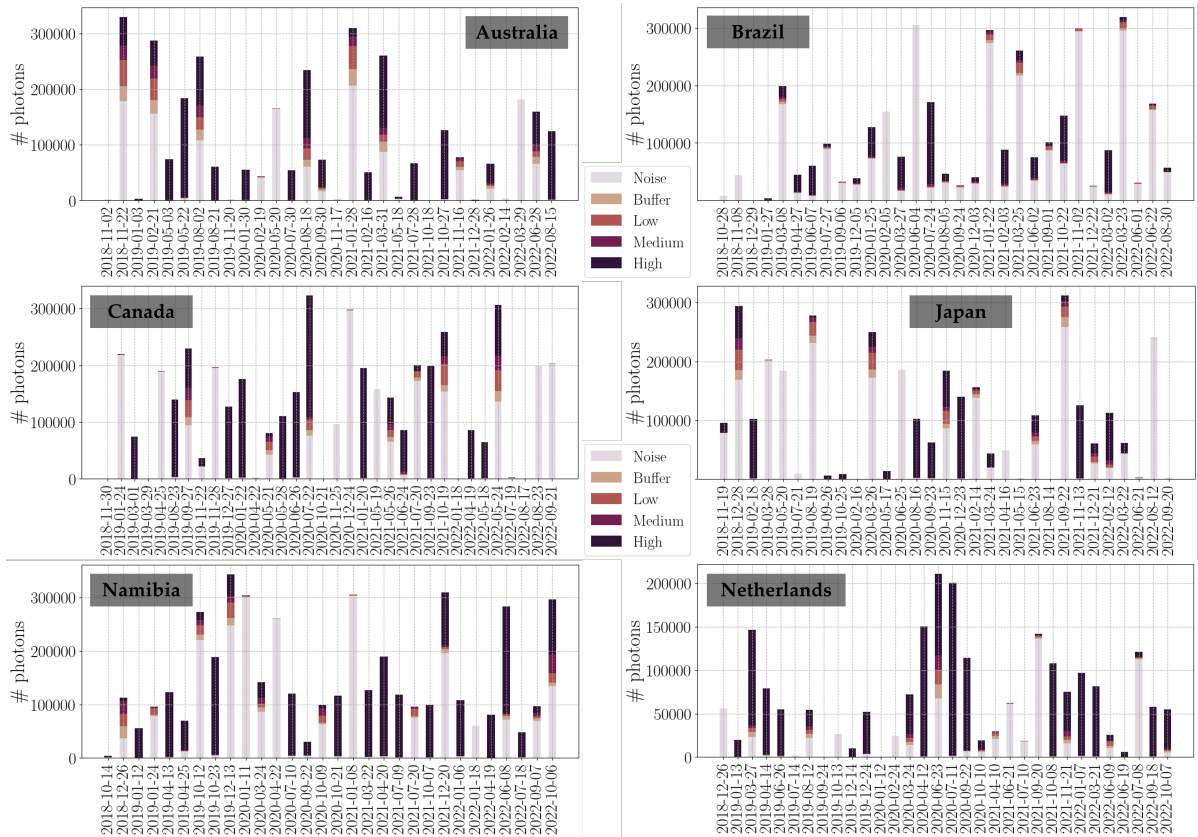


Figure 5.17: From the sample of boxes presented (see Figure 5.16), the dates of measurements are presented for a few cases. The plots present the dates on the x - axis, the number of photons on the y - axis, and the bars are colored based on the classification of the photons: 'Noise', 'Buffer', 'Low', 'Medium', and 'High'.

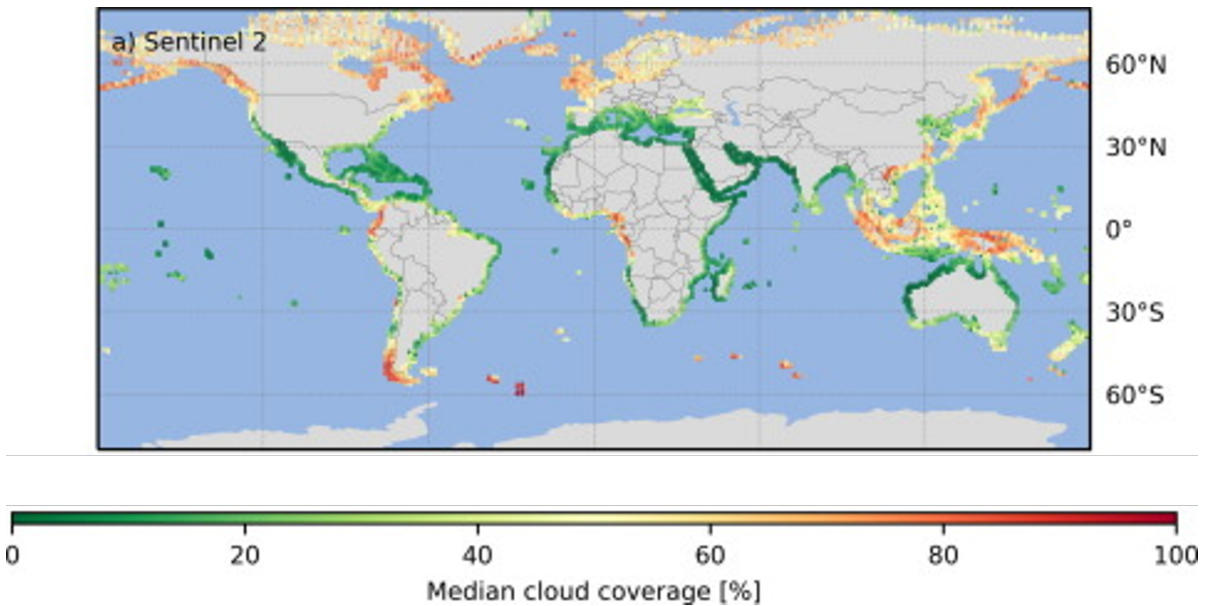


Figure 5.18: Bergsma and Almar [54] computed the median cloud coverage using Sentinel-2 optical imagery on coastal areas world-wide.

Despite the smaller spacing between tracks in higher latitudes, which should result in more passes and more photons in a given box, this is not always the case, as observed. A comparison between the Netherlands (latitude $\sim 53.46^\circ$) and Spain (GC) (latitude $\sim 28.14^\circ$) highlights these differences. Spain

(GC) is expected to have fewer dates, passes, and photons, but approximately 5.23 million photons were collected in this box, whereas the Netherlands box contains only around 2.17 million photons, less than half of the former. Moreover, despite having a larger number of photons, Spain (GC) has the lowest percentage of high-quality photons, likely due to atmospheric effects caused by the sun. Overall, the observed variations in photon counts and quality between different latitudes can be attributed to a combination of factors such as cloud coverage, orbital configuration, and atmospheric conditions.

However, if the number of passes per box is analysed, and boxes from the Netherlands and Spain (GC) compared, it is observed that the box from Spain (GC) has a larger amount of dates than Netherlands too. The differences in the number of photons and number of dates are because of the cloud coverage, the most likely explanation is that even though the box at Ameland, Netherlands, should contain more amount of passes and photons, quite often due to opaque clouds, all the photons above this area are discarded, leading to no pass. Furthermore, the relatively low amount of photons despite the relatively large number of passes, is likely to be due to the same reason, but in this case, because of gaps between clouds, some photons can be measured on the box of interest, counting as pass and as measurement date, but not extracting a large number of ground elevations.

In Table 5.7, despite the absence of discernible patterns resulting from factors such as latitude, orbital configuration, or cloud coverage, some valuable information can be extracted. The average of passes over a box of 20km^2 is 123.25 passes, while the average of valid passes is 79.75 passes. However, specific regions exhibit variations from these averages. For instance, Spain (GC) experiences over 150 passes, while Australia and the US have fewer than 110 passes. Interestingly, a higher number of passes does not necessarily translate to a greater number of valid passes, as demonstrated by the column representing the ratio of valid passes. Spain (GC) has 156 passes, but only 86 of them are valid. In contrast, the US has 106 passes, 50 less than Spain (GC), yet it boasts 88 valid passes. The considerable number of invalid passes for Spain (GC), where there are less than 500 geolocated photons classified as high quality photons, can likely be attributed to the majority of photons being flagged as 'Noise' due to low cloud coverage or atmospheric interference from sunlight.

Based on the previous analysis of Figures 5.16, 5.17, 5.18, and the figures from Appendix B, and Table 5.7, it is inferred that due to ICESat-2's weather dependency and the relatively low resolution of ICESat-2 measurements boxes might not represent what is expected for their locations. Because of the variability of ICESat-2 passes over coastal areas, analysing accurately if it would be possible to monitor or not beach profiles and beach face slopes is not trivial. Consequently, for a proper spatial and temporal exploration of ICESat-2 ATL03 data on world's coastlines the processing and analysis of all ICESat-2 ATL03 data world-wide is required. Therefore, as commented previously, the elaborated methodology (see section 4.3), tested with the JARKUS dataset (see section 5.3), is currently processing ICESat-2 ATL03 data on 20 km^2 boxes around the globe. Figure 5.19 displays the processed data to date, 5062 boxes, providing insights into the distribution of ICESat-2 ATL03 data and revealing the limitations and opportunities for extracting coastal features with this and similar devices.

As it is possible to glimpse from the different panels shown in this figure, ICESat-2 data on coastal areas follow a similar pattern as the presented in Figure 5.18, this is, the cloud coverage. This can be especially observed in the upper panel, where the ratio of high quality photons per box of 20 km^2 is shown. In areas like the west of Canada, Alaska (US), the south of Chile and the UK, it is possible to see that the ratio of high quality photons is smaller than in the Caribbean, Mediterranean, and Persian Gulf. This corresponds with the cloud coverage shown in Figure 5.18. In the middle panel representing the number of dates, it is challenging to discern a clear pattern. However, this preliminary observation suggests a potentially lower number of dates around the equator compared to higher latitudes. In order to confirm the presence of this pattern, it is essential to process a larger number of boxes. Moreover, in this panel, the values appear to be closely grouped together, exhibiting similar values for most of the boxes. It is observed that around the globe, independently of the cloud coverage and latitude, most of these boxes of 20 km^2 seem to be overflowed around 20-30 different days through a time frame of four years.

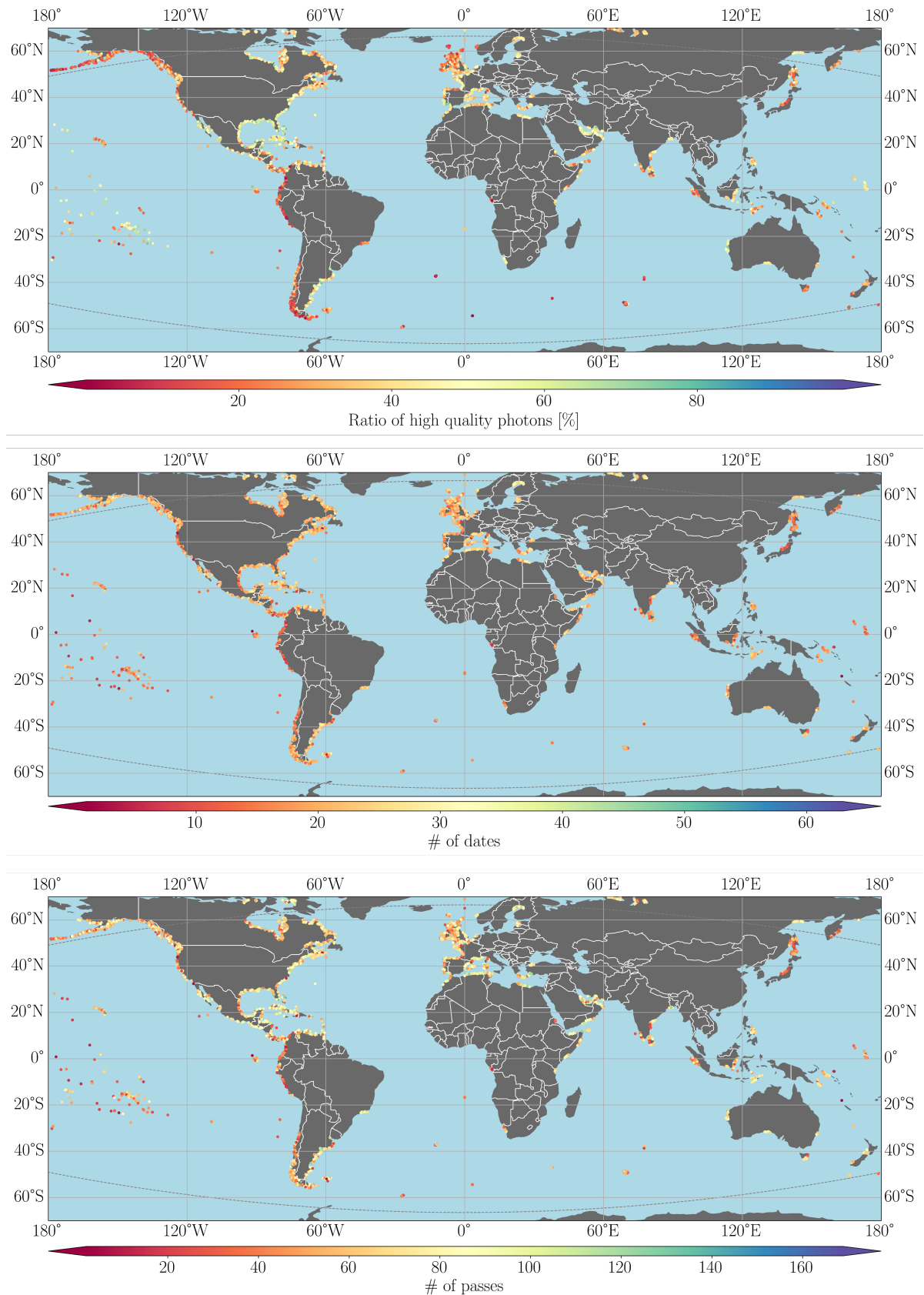


Figure 5.19: World-wide coastal ICESat-2 distribution (with data processed up to date). ICESat-2 ATL03 data is processed by analysing boxes of 20 km^2 and presented here through different indicators: the ratio of high quality photons [%] (upper panel), the number of dates (middle panel), and number of passes (lower panel). Due to time constraints and the deadline for this report, it is not feasible to download and process all ICESat-2 ATL03 data.

In the lower panel it is observed that most of the boxes contain between 40 to 100 passes and that the number of passes follow a similar distribution to the one shown in the upper panel. Besides, there appears to be a certain degree of correlation with the cloud coverage depicted in Figure 5.18, although not as strong as in the upper panel. Regarding the maximum values of the number of dates and number of passes, there are boxes that have been measured on more than 60 different days, and some boxes have even accumulated more than 160 passes. These boxes are not shown in Figure 5.19 because they are located in Greenland. In this figure, the map is centered between $70^{\circ}N$ and $70^{\circ}S$ where most of the sandy and populated coasts are located. Nevertheless, cases of boxes with around 120-140 passes can be found in areas with low cloud coverage, such as the Caribbean, Argentina, Saudi Arabia, Bangladesh, as well as in the Mediterranean.

Figure 5.20 presents the histograms from the boxes already processed (see Figure 5.19). Different indicators are used for exploring the spatial and temporal variability of ICESat-2 ATL03 data on coastal areas. These indicators are the percentage of high quality photons per box of 20 km^2 (panel a), the number of measurement date per box (panel b), number of passes per box (panel c), and finally, number of valid passes per box (panel d). It is important to remember that a valid pass is one that contains more than 500 photons classified as high quality, and that the angle between this pass and the transect is less than 60 degrees.

The histogram showing the distribution of high quality photons follows approximately a Gaussian distribution, with a mean of $\sim 35\%$. Besides, it is observed that there are boxes with almost no high quality photons, and others up to almost 80-85 % of the measured photons being classified as high quality photons. Similarly, the histograms for the number of dates and passes (panels b and c) exhibit a resemblance to the bell-shaped Gaussian distribution, with mean values of 19.91 measurement dates and 63.26 passes per box, respectively. Regarding the number of measurement dates, there are instances where a box has almost no measurements, but certain areas contain boxes with up to 60 different measurements spanning a four-year period. In terms of the number of passes, some boxes have close to zero passes, while there are cases where the count reaches approximately 160 passes per box. Furthermore, it is evident that the distribution of the number of dates is less dispersed and more centered around the mean value. In contrast, the number of passes exhibits a slower decrease in frequency as it deviates from the mean. Finally, panel d illustrates the distribution of the number of valid passes per box. The data shows an accumulation around zero, with a gradual decay as the number of valid passes increases. On average, each box contains approximately 32.57 valid passes, and some boxes can get to contain more than 100 valid passes.

The partial spatial and temporal exploration of ICESat-2 ATL03 data along the world's coastlines conducted in this section yields valuable insights regarding the dependence of ICESat-2 measurements on various factors. Specifically, the analysis sheds light on the influence of weather conditions, latitude, and coastline geometry on the data. These findings enable to draw interesting and useful conclusions about the behavior and characteristics of ICESat-2 data in different geographical regions. By examining the data along the world's coastlines, it becomes evident that ICESat-2 measurements are influenced by weather conditions, it seems to have high correlation with the cloud coverage. It is important to acknowledge that both, cloud coverage and solar effects can result in gaps within the passes, impacting data availability and completeness.

The analysis reveals that even though there seems to be large correlation between cloud coverage and ICESat-2 ATL03 data, this is mainly regarding the quality of the photons. When it comes to number of dates and number of passes, different factors might play a more important role than the cloud coverage leading to different distributions. There seems to be observed a slight dependency of ICESat-2 on the latitude, as expected due to its orbital configuration. However, it is not clear, and in order to assure it, more boxes in different parts of the world must be processed.

ICESat-2, over the course of its four-year measurement period, has collected a substantial number of geolocated photons per box. On average, approximately 35% of these photons are classified as high quality. Besides, the satellite has repeatedly measured each box an average of 19.91 times, delivering an average of 63.26 passes per box. In addition, the average amount of valid passes per box, after filtering

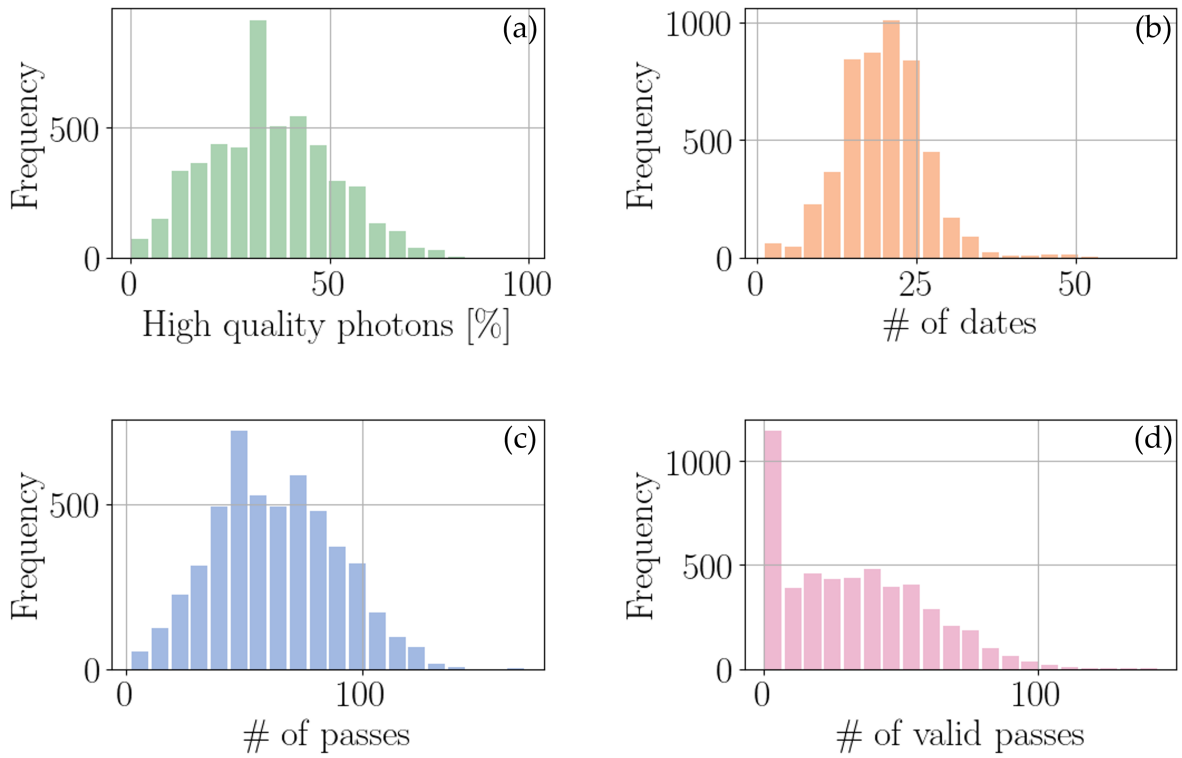


Figure 5.20: Histograms computed from boxes presented in Figure 5.19. Panel a shows number of boxes based on the number of high-quality photons. Panel b and c displays the frequency of boxes with respect to the number of dates recorded and with respect to the number of passes respectively. Panel d presents the frequency of boxes categorized by the number of valid passes (those with more than 500 photons classified as high quality).

them based on the amount of high quality photons per pass (≥ 500), and with an angle between the pass and the closer transect lower than 60 degrees, is of 32.57. This is, approximately 8 valid passes per year.

Furthermore, there is a reasonably large amount of boxes with measurement dates, passes and valid passes over 25, 90, and 60 respectively. These amounts indicate that there are approximately 6, 22.5, and 15 measurement dates, passes and valid passes respectively per year. This amount of passes might provide enough beach face slopes per year for monitoring this parameter. However, in terms of monitoring, the dependency of the beach face slope estimation on the angle between pass and transect might be a limitation for some stretches of coast. Overall, this exploration underscores the intricate relationship between ICESat-2 data and factors such as weather conditions, latitude, and coastline geometry. The findings contribute to a better understanding of the limitations and opportunities associated with the ICESat-2 dataset for coastal regions.

6

Conclusions and Recommendations

This chapter presents the conclusions drawn from the research conducted, along with recommendations for further analysis of the matter. Its purpose is to summarize the main findings of the study, provide insights into their significance, and propose directions for future research.

6.1. Conclusions

This MSc thesis research aims to provide valuable insight regarding the feasibility of extracting and monitoring the beach face slope using a LiDAR-based satellite, ICESat-2. For this, different methodologies for answering the main research question and subsequent subquestions, posed in section 1.1, were developed. These methodologies address the various subquestions and yield the essential results required to correctly answer the main research question:

To what extent can the beach face slope be derived from ICESat-2?

The findings of this research demonstrate that ICESat-2 has the potential to facilitate automatic extraction of beach face slopes at global scale, provided some challenges are overcome. The results exhibit favorable consistency between beach profiles, beach face profiles, and beach face slopes from ICESat-2 ATL03 data and the validation datasets. However, it is important to note that the extraction of beach face slopes using ICESat-2 is influenced by factors such as weather conditions, beach geometry, the angle between pass and cross-shore profile, and latitude. The variation in these factors along different coastal stretches leads to fluctuations in the accuracy of the beach face slope extraction, as well as in the feasibility of its monitoring. Furthermore, among other challenges, the automation of the beach face demarcation is the most challenging step that must be tackled before upscaling the methodology at a global scale. Nonetheless, if the correct delineation of this area is overcome, the detected amount of passes available might allow a consistent monitoring in areas with low cloud coverage, and stretches of coast favorably oriented with respect to ICESat-2's orbit. Therefore, it is encouraged to continue the research towards mapping the beach face slope at a global level using LiDAR-based satellites such as ICESat-2, acknowledging its limitations due to a variety of factors, but also its opportunities.

To delve deeper into the main findings of this research, the answers to the research subquestions are given accordingly. The key points extracted from the research done around each subquestion are concisely provided for clearly understanding the research outcomes and shed light on this novel beach face slope extraction method.

This research shows that ICESat-2 is able to capture beach features such as the beach profile and beach face profile, and therefore, from the latter, the beach face slope. However, for answering to what extent the beach profiles and beach face slopes can be derived from ICESat-2, a series of methodologies were developed for analysing different aspects of interest, which were translated to research subquestions

(presented in Chapter 1) and are answered in a corresponding manner:

How accurate can beach profiles, and the subsequent beach face slopes be extracted from ICESat-2 ATL03 data?

The analysis of the Terrain Laser Scanner (TLS) validation dataset revealed a strong agreement between ICESat-2 passes and TLS point cloud profiles. The vertical uncertainty of ICESat-2 was within its expected levels, with low MSE and $RMSE$ values, and MAE values below 17 cm, and low errors and percentage errors, PE , when comparing the subsequent slopes (PE of around 10-11%). When the passes are projected to transects perpendicular to the coastline and compared to the corresponding cross-shore profiles extracted from the TLS point cloud, the agreement between profiles deteriorates. It is reflected by higher MSE and $RMSE$ values, and MAE values of up to 34 cm, what can be considered as tolerable within the own beach alongshore variability. Despite the loss in agreement between profiles, the agreement between beach face slopes can diminish, but it can also improve. While one of the projected passes led to a PE of 40%, the PE from the beach face slope comparison of the other pass was of 4%. Then, it is concluded that ICESat-2 is able to extract beach profiles accurately, as well as beach face slopes, and that for similar beaches, 40% of PE is something that can be expected and seems to fall within the own beach alongshore variability.

As a result of the time difference between the collection of ICESat-2 data and the RTK-GPS validation dataset (~ 3.25 years), the upper part of the profile shows more variability. Then, only the beach face profiles and subsequent beach face slopes are compared. Despite this time difference, the comparisons between beach face slopes give PE values below 40%, showing that the beach face slopes from ICESat-2 passes are representative of the beach. Furthermore, for both cases, the angle between shoreline and passes are relatively large, showing that for wide long beaches, small errors are induced by projecting ICESat-2 measurements into cross-shore profiles. This was further analysed with the synthetic data and answered in the next research subquestion.

How dependant is the beach face slope extraction from ICESat-2 passes on beach geometry and the direction of its own fixed ground track?

According to the results extracted from the two analysed beaches, it is concluded that the beach face slope extraction is dependent on the angle, α , between pass and transect the pass is projected into, as well as on the distance between the pass and the transect's centroid. The extent to which these factors influence the slope extraction is further determined by the beach geometry. Therefore, the beach face slope extraction is not only dependent on the angle and distance between pass and transect, but it is also highly influenced by the beach geometry.

For long, wide beaches with low variability alongshore, it is concluded the following:

- The dependency of the beach face slope extraction on α is almost nonexistent. Beach face slopes are correctly estimated, showing low PE values, below 20%, up to 70-80 degrees.
- In terms of the beach profile and beach face profile, a noticeable relationship with the distance between pass and transect is observed, as evidenced by discernible patterns on the corresponding mosaics. However, when it comes to beach face slopes, there is no apparent dependency on this distance. Regardless of this, the slopes are consistently and accurately estimated, resulting in PE values below 20%.
- Beach face slopes can be accurately estimated and extrapolated throughout the beach due to its low variability alongshore. Then, monitoring these beaches might be feasible regardless of α and the section of the beach measured by ICESat-2.

For small, narrow, and pocket-shaped beaches the conclusions are:

- The dependency of the beach face slope extraction on α is larger than for long beaches.

More variability and larger PE values are observed.

- A distinctive pattern indicating the dependency of the beach face slope extraction on α , as well as on the distance between the pass and the beach face, is observed. On one hand, the closer the pass is to the beach face of interest, the better is the beach face slope estimation, showing low PE values (below 20%) up to 70-80 degrees.

On the other hand, as the distance and α between pass and beach face increase, the accuracy of the beach face slope estimate diminishes, showing large PE values, up to 60-70%.

As a result, the study concludes that longer and less variable alongshore beaches are more likely to yield a more accurate beach face slope estimation and have a higher potential for monitoring purposes. Furthermore, it is important to acknowledge that the more intricate and variable the beaches are, as well as the larger α becomes for these coastal stretches, the more uncertainty is induced in the beach face slope estimation.

What are the limitations regarding the ICESat-2 spatial and temporal resolution? To what extent can ATL03 data be used for monitoring beach face slopes?

It is not trivial to correctly assess the ICESat-2 spatial and temporal resolution at a global scale without downloading and processing all the data first, and this limitation is due to the high variability of ICESat-2 along the coasts of the world. The partial spatial and temporal exploration was done by analysing 5062 boxes of 20km^2 . Although it is a sample and does not cover all the world's coastlines, it provides valuable insights into the behavior of ICESat-2 and offers a glimpse into its limitations and potential opportunities for coastal areas.

The amount of measurements done per box, and therefore, the amount of passes and number of high quality photons, are dependent on:

- the latitude, due to ICESat-2's orbital configuration;
- the weather conditions, ICESat-2 LiDAR measurements are strongly affected by clouds;
- and when it comes to the beach face slope extraction, the amount of valid passes depends on the coastline's geometry. As concluded, the lower α is, the more likely the estimated beach face slope is to be accurate.

Despite the various factors on which ICESat-2 passes and beach face slope extraction depend, the quantity of available measurements in different areas is relatively large. Per box it is on average that: approximately 35% of high-quality photons, 19.91 days of measurement, 63.26 passes, and 32.57 valid passes per 20 km^2 box were recorded over a period of five years. This suggests that in regions where cloud coverage is low and beach geometry is favorable, implementing a monitoring system utilizing ICESat-2 could be feasible. This is particularly relevant for areas with low cloud coverage, and long beaches with low variability alongshore.

What are the possibilities for upscaling a beach face slope methodology from ICESat-2 ATL03 data?

As demonstrated throughout the report, the whole process can be upscaled up to the final demarcation of the intertidal area or beach face. The correct delineation of the lower and upper boundary is not trivial, as even slight changes in this selection can result in different beach face slopes. The methodology allows the extraction of cross-shore profiles at a global level. Nevertheless, the correct demarcation of beach and beach face profiles, and therefore, the final extraction of the beach face slope needs further tuning. As a result of the complex interplay between factors such as wave and environmental conditions, human activities, artifacts, and variations in beach morphology, it is not a straightforward task to accurately delineate the beach face using a ruled-based approach. Instead, a range of techniques and mathematical algorithms

must be employed to account for this diversity, and create a method for demarcating the beach face. Although several challenges have to be overcome, this study provides a novel methodology that sets the basis for a new era of coastal management and monitoring using LiDAR-based satellites at a global level.

6.2. Recommendations

From this report it was concluded that the use of ICESat-2 ATL03 data to extract beach face profiles holds significant potential for improving our understanding of coastal dynamics, as well as for managing and monitoring these areas. By following the methodology outlined in this document, researchers can obtain more precise and detailed beach profiles than ever before at a global level under the same methodology. We recommend that future studies consider incorporating ICESat-2 data to further enhance our knowledge of coastal processes and to inform decision-making in coastal management.

In this section, the recommendations for continuing this research are presented. As concluded, for correctly upscaling and optimizing the beach face slope extraction, a comprehensive method for demarcating the beach face is required. For this, it is recommended to employ the water occurrence probability layer (WOP). The WOP layer was employed in this report for extracting the beach face on the beaches used for generating the synthetic data. It was used only here because, as commented on section 3.4, this layer is not always correctly extracted. However with an improvement of the extraction of this layer, Sentinel-2 optical imagery might provide enough spatial and temporal resolution for accurately delineating the beach face.

If the WOP layer is successfully extracted, it is recommended to use an algorithm where the data within the point cloud is analysed simultaneously with the WOP layer, as well as the tidal range on the area, and the time of the measurement, which provides the tide at that moment. With this algorithm, the correct beach face slope extraction can be accurately extracted, and implemented at a global level, and potentially for almost every coastal environment where the tidal range allows the WOP layer extraction.

Regarding the beach face slope monitoring using ICESat-2, this report provides a glimpse on how ICESat-2 might be distributed over the world's coastline, the amount of passes and days of passes over boxes of 20 km^2 , and the different factors these might depend on. Then, once boxes around the globe are processed and analysed, and a better understanding on the patterns and distribution of ICESat-2 ATL03 data has on coastal areas is gained, the next step is to analyse in depth one of these boxes. For doing so, an ideal location must be selected, the characteristics of this ideal location are: 1) low cloud coverage; 2) good orientation of the coastline with respect to ICESat-2 orbit; 3) long and sandy beaches (approximately 20 km long); and 4) with two clear wave regimes, this is, two profiles, summer and winter profiles. As shown in the report, boxes in areas with these characteristics might contain more than 80 valid passes, that might lead to the extraction of 80 beach profiles and subsequent beach face slopes in a 20 km beach. Then, a time series analysis can be conducted for analysing how well the beach face slopes relate to the different wave regimes. Furthermore, it would be excellent if the beach face slope of the beach is already being monitored through other methods and comparisons can be made.

ICESat-2 ATL03 data can be used for extracting beach face slopes, however, it might only allow to monitor certain types of beaches. This is due to its dependency on weather as well as on the orbit followed by the satellite. Both are physical limitations difficult to solve, and that make the monitoring of this parameter with ICESat-2 not feasible at a global level with high temporal and spatial resolution. Nevertheless, satellite missions employing cube, micro, and small satellite platforms might be ideal to fill up this gap. These satellites are relatively inexpensive and a set of them could be launched to different orbits and be used for monitoring beaches at a higher pace and higher spatial resolution [55]. This mission could be implemented by a company, a country, or as an international effort.

References

- Hallegette, Stephane et al. (2016). *Shock Waves: Managing the Impacts of Climate Change on Poverty*. Washington, DC: World Bank. ISBN: 978-1-4648-0673-5. DOI: 10.1596/978-1-4648-0673-5. URL: <http://hdl.handle.net/10986/22787> (visited on Jan. 26, 2023).
- Martínez, M.L. et al. (Aug. 2007). “The coasts of our world: Ecological, economic and social importance”. In: *Ecological Economics* 63.2, pp. 254–272. ISSN: 09218009. DOI: 10.1016/j.ecolecon.2006.10.022. URL: <https://linkinghub.elsevier.com/retrieve/pii/S0921800906005465> (visited on Jan. 26, 2023).
- McGranahan, Gordon, Deborah Balk, and Bridget Anderson (Apr. 2007). “The rising tide: assessing the risks of climate change and human settlements in low elevation coastal zones”. In: *Environment and Urbanization* 19.1, pp. 17–37. ISSN: 0956-2478, 1746-0301. DOI: 10.1177/0956247807076960. URL: <http://journals.sagepub.com/doi/10.1177/0956247807076960> (visited on Nov. 16, 2022).
- Ahsan, Reazul, Jon Kellett, and Sadasivam Karuppanan (2016). “Climate Migration and Urban Changes in Bangladesh”. In: *Urban Disasters and Resilience in Asia*. Elsevier, pp. 293–316. ISBN: 978-0-12-802169-9. DOI: 10.1016/B978-0-12-802169-9.00019-7. URL: <https://linkinghub.elsevier.com/retrieve/pii/B9780128021699000197> (visited on Nov. 16, 2022).
- Stive, Marcel J.F et al. (Dec. 2002). “Variability of shore and shoreline evolution”. In: *Coastal Engineering* 47.2, pp. 211–235. ISSN: 03783839. DOI: 10.1016/S0378-3839(02)00126-6. URL: <https://linkinghub.elsevier.com/retrieve/pii/S0378383902001266> (visited on Nov. 16, 2022).
- Guerra-Medina, Daniel and Germán Rodríguez (May 2021). “Spatiotemporal Variability of Extreme Wave Storms in a Beach Tourism Destination Area”. In: *Geosciences* 11.6, p. 237. ISSN: 2076-3263. DOI: 10.3390/geosciences11060237. URL: <https://www.mdpi.com/2076-3263/11/6/237> (visited on Oct. 26, 2022).
- Center (U.S.), Coastal Engineering Research (1984). *Shore Protection Manual*. en. Department of the Army, Waterways Experiment Station, Corps of Engineers, Coastal Engineering Research Center.
- O’Grady, J. G. et al. (2019). “Extreme Water Levels for Australian Beaches Using Empirical Equations for Shoreline Wave Setup”. en. In: *Journal of Geophysical Research: Oceans* 124.8. eprint: <https://onlinelibrary.wiley.com/doi/pdf/10.1029/2018JC014871>, pp. 5468–5484. ISSN: 2169-9291. DOI: 10.1029/2018JC014871. URL: <https://onlinelibrary.wiley.com/doi/abs/10.1029/2018JC014871> (visited on Mar. 25, 2023).
- Melet, Angélique et al. (Mar. 2018). “Under-estimated wave contribution to coastal sea-level rise”. en. In: *Nature Climate Change* 8.3. Number: 3 Publisher: Nature Publishing Group, pp. 234–239. ISSN: 1758-6798. DOI: 10.1038/s41558-018-0088-y. URL: <https://www.nature.com/articles/s41558-018-0088-y> (visited on Mar. 25, 2023).
- Vitousek, Sean et al. (May 2017). “Doubling of coastal flooding frequency within decades due to sea-level rise”. en. In: *Scientific Reports* 7.1. Number: 1 Publisher: Nature Publishing Group, p. 1399. ISSN: 2045-2322. DOI: 10.1038/s41598-017-01362-7. URL: <https://www.nature.com/articles/s41598-017-01362-7> (visited on Mar. 25, 2023).
- Vos, Kilian et al. (Mar. 2022). “Beach-face slope dataset for Australia”. English. In: *Earth System Science Data* 14.3. Publisher: Copernicus GmbH, pp. 1345–1357. ISSN: 1866-3508. DOI: 10.5194/essd-14-1345-2022. URL: <https://essd.copernicus.org/articles/14/1345/2022/> (visited on Mar. 21, 2023).
- Bujan, Nans, Rónadh Cox, and Gerd Masselink (Nov. 2019). “From fine sand to boulders: Examining the relationship between beach-face slope and sediment size”. en. In: *Marine Geology* 417, p. 106012. ISSN: 0025-3227. DOI: 10.1016/j.margeo.2019.106012. URL: <https://www.sciencedirect.com/science/article/pii/S0025322718304365> (visited on Mar. 10, 2023).
- Athanasiou, Panagiotis et al. (Oct. 2019). “Global distribution of nearshore slopes with implications for coastal retreat”. In: *Earth System Science Data* 11, pp. 1515–1529. DOI: 10.5194/essd-11-1515-2019.

- Markus, Thorsten et al. (Mar. 2017). “The Ice, Cloud, and land Elevation Satellite-2 (ICESat-2): Science requirements, concept, and implementation”. en. In: *Remote Sensing of Environment* 190, pp. 260–273. ISSN: 0034-4257. DOI: 10.1016/j.rse.2016.12.029. URL: <https://www.sciencedirect.com/science/article/pii/S0034425716305089> (visited on Mar. 11, 2023).
- Ma, Yue et al. (2023). “Estimating coastal slope of sandy beach from ICESat-2: a case study in Texas”. en. In: *Environmental Research Letters*. ISSN: 1748-9326. DOI: 10.1088/1748-9326/acc87d. URL: <http://iopscience.iop.org/article/10.1088/1748-9326/acc87d> (visited on Apr. 3, 2023).
- Xie, Huan et al. (Sept. 2021). “Shore Zone Classification from ICESat-2 Data over Saint Lawrence Island”. In: *Marine Geodesy* 44.5, pp. 454–466. ISSN: 0149-0419. DOI: 10.1080/01490419.2021.1898498. URL: <https://doi.org/10.1080/01490419.2021.1898498> (visited on Mar. 28, 2023).
- Oppenheimer, Michael et al. (n.d.). “Sea Level Rise and Implications for Low-Lying Islands, Coasts and Communities”. en. In: ().
- T., Neumann et al. (Oct. 2021). “Algorithm Theoretical Basis Document (ATBD) for Global Geolocated Photons, ATL03.” URL: https://nsidc.org/sites/nsidc.org/files/technical-references/ICESat2_ATL03_ATBD_r005.pdf (visited on Apr. 16, 2023).
- Mangor, K. and DHI Institut for Vand og Miljø (2001). *Shoreline Management Guidelines*. DHI Water & Environment. ISBN: 978-87-981950-9-2. URL: <https://books.google.nl/books?id=D71aAAAACAAJ>.
- Schwartz, Maurice (July 2005). *Encyclopedia of Coastal Science*. Vol. 21. Journal Abbreviation: Journal of Coastal Research - J COASTAL RES Publication Title: Journal of Coastal Research - J COASTAL RES. ISBN: 978-1-4020-1903-6. DOI: 10.2112/1551-5036(2005)21[866:BR]2.0.CO;2.
- Morton, Robert A. and F. Michael Speed (1998). “Evaluation of Shorelines and Legal Boundaries Controlled by Water Levels on Sandy Beaches”. In: *Journal of Coastal Research* 14.4. Publisher: Coastal Education & Research Foundation, Inc., pp. 1373–1384. ISSN: 0749-0208. URL: <https://www.jstor.org/stable/4298899> (visited on Mar. 10, 2023).
- Iribarren RR and Nogales, C (1949). “Protection des Ports, proceedings from the XVIIth International Navigation Congress”. In.
- Ruggiero, Peter, R. A. Holman, and R. A. Beach (2004). “Wave run-up on a high-energy dissipative beach”. en. In: *Journal of Geophysical Research: Oceans* 109.C6. ISSN: 2156-2202. DOI: 10.1029/2003JC002160. URL: <https://onlinelibrary.wiley.com/doi/abs/10.1029/2003JC002160> (visited on Mar. 10, 2023).
- Passarella, Marinella et al. (May 2018). “An Assessment of Swash Excursion Predictors using Field Observations”. In: *Journal of Coastal Research* 85, pp. 1036–1040. ISSN: 0749-0208, 1551-5036. DOI: 10.2112/SI85-208.1. URL: <http://www.bioone.org/doi/10.2112/SI85-208.1> (visited on Feb. 21, 2023).
- Guza, R. T. and E. B. Thornton (1981). “Wave set-up on a natural beach”. en. In: *Journal of Geophysical Research: Oceans* 86.C5, pp. 4133–4137. ISSN: 2156-2202. DOI: 10.1029/JC086iC05p04133. URL: <https://onlinelibrary.wiley.com/doi/abs/10.1029/JC086iC05p04133> (visited on Mar. 10, 2023).
- Vos, Kilian et al. (2020). “Beach Slopes From Satellite-Derived Shorelines”. en. In: *Geophysical Research Letters* 47.14, e2020GL088365. ISSN: 1944-8007. DOI: 10.1029/2020GL088365. URL: <https://onlinelibrary.wiley.com/doi/abs/10.1029/2020GL088365> (visited on Mar. 10, 2023).
- Bosboom, Judith and Marcel J. F. Stive (Jan. 2023). “Coastal Dynamics”. en. In: *TU Delft OPEN Textbooks*. ISBN: 9789463663717. URL: <https://textbooks.open.tudelft.nl/textbooks/catalog/view/37/92/383-1> (visited on Mar. 10, 2023).
- Phillips, M. R. and C. House (Apr. 2009). “An evaluation of priorities for beach tourism: Case studies from South Wales, UK”. en. In: *Tourism Management* 30.2, pp. 176–183. ISSN: 0261-5177. DOI: 10.1016/j.tourman.2008.05.012. URL: <https://www.sciencedirect.com/science/article/pii/S0261517708000976> (visited on Mar. 10, 2023).
- Gopalakrishnan, Sathya et al. (May 2011). “The value of disappearing beaches: A hedonic pricing model with endogenous beach width”. en. In: *Journal of Environmental Economics and Management* 61.3, pp. 297–310. ISSN: 0095-0696. DOI: 10.1016/j.jeem.2010.09.003. URL: <https://www.sciencedirect.com/science/article/pii/S0095069610001221> (visited on Mar. 10, 2023).
- McLachlan, Anton and Atsu Dorvlo (July 2005). “Global Patterns in Sandy Beach Macrobenthic Communities”. In: *Journal of Coastal Research* 2005.214. Publisher: Coastal Education and Research Foundation, pp. 674–687. ISSN: 0749-0208, 1551-5036. DOI: 10.2112/03-0114.1. URL: <https://bioone.org/journals/journal-of-coastal-research/volume-2005/issue-214/03-0114>.

- 1/Global-Patterns-in-Sandy-Beach-Macrobenthic-Communities/10.2112/03-0114.1.full (visited on Mar. 10, 2023).
- Wright, L. D and A. D Short (Apr. 1984). “Morphodynamic variability of surf zones and beaches: A synthesis”. en. In: *Marine Geology* 56.1, pp. 93–118. ISSN: 0025-3227. DOI: 10.1016/0025-3227(84)90008-2. URL: <https://www.sciencedirect.com/science/article/pii/0025322784900082> (visited on Mar. 10, 2023).
- Davies, John Lloyd and K. M. Clayton (1980). *Geographical variation in coastal development*. 2d ed. Geomorphology texts 4. London ; New York: Longman. ISBN: 978-0-582-49006-2.
- Liu, Aobo, Xiao Cheng, and Zhuoqi Chen (Oct. 2021). “Performance evaluation of GEDI and ICESat-2 laser altimeter data for terrain and canopy height retrievals”. en. In: *Remote Sensing of Environment* 264, p. 112571. ISSN: 0034-4257. DOI: 10.1016/j.rse.2021.112571. URL: <https://www.sciencedirect.com/science/article/pii/S0034425721002911> (visited on Mar. 12, 2023).
- Narine, Lana L. et al. (Apr. 2019). “Estimating aboveground biomass and forest canopy cover with simulated ICESat-2 data”. en. In: *Remote Sensing of Environment* 224, pp. 1–11. ISSN: 0034-4257. DOI: 10.1016/j.rse.2019.01.037. URL: <https://www.sciencedirect.com/science/article/pii/S0034425719300434> (visited on Mar. 12, 2023).
- Weitkamp, Claus, ed. (2005). *Lidar: range-resolved optical remote sensing of the atmosphere*. Springer series in optical sciences 102. New York: Springer. ISBN: 978-0-387-40075-4.
- Neumann, Thomas A. et al. (Nov. 2019). “The Ice, Cloud, and Land Elevation Satellite – 2 mission: A global geolocated photon product derived from the Advanced Topographic Laser Altimeter System”. en. In: *Remote Sensing of Environment* 233, p. 111325. ISSN: 0034-4257. DOI: 10.1016/j.rse.2019.111325. URL: <https://www.sciencedirect.com/science/article/pii/S003442571930344X> (visited on Mar. 12, 2023).
- Ranndal, Heidi et al. (Jan. 2021). “Evaluation of a Statistical Approach for Extracting Shallow Water Bathymetry Signals from ICESat-2 ATL03 Photon Data”. en. In: *Remote Sensing* 13.17. Number: 17 Publisher: Multidisciplinary Digital Publishing Institute, p. 3548. ISSN: 2072-4292. DOI: 10.3390/rs13173548. URL: <https://www.mdpi.com/2072-4292/13/17/3548> (visited on Mar. 12, 2023).
- Magruder, Lori, Thomas Neumann, and Nathan Kurtz (2021). “ICESat-2 Early Mission Synopsis and Observatory Performance”. en. In: *Earth and Space Science* 8.5, e2020EA001555. ISSN: 2333-5084. DOI: 10.1029/2020EA001555. URL: <https://onlinelibrary.wiley.com/doi/abs/10.1029/2020EA001555> (visited on Apr. 10, 2023).
- Zhu, Xiaoxiao et al. (Sept. 2020). “The Performance of ICESat-2’s Strong and Weak Beams in Estimating Ground Elevation and Forest Height”. In: *IGARSS 2020 - 2020 IEEE International Geoscience and Remote Sensing Symposium*. ISSN: 2153-7003, pp. 6073–6076. DOI: 10.1109/IGARSS39084.2020.9323094.
- Di Biase, Valeria, Ramon F. Hanssen, and Sander E. Vos (Jan. 2021). “Sensitivity of Near-Infrared Permanent Laser Scanning Intensity for Retrieving Soil Moisture on a Coastal Beach: Calibration Procedure Using In Situ Data”. en. In: *Remote Sensing* 13.9. Number: 9 Publisher: Multidisciplinary Digital Publishing Institute, p. 1645. ISSN: 2072-4292. DOI: 10.3390/rs13091645. URL: <https://www.mdpi.com/2072-4292/13/9/1645> (visited on Apr. 19, 2023).
- Di Biase, Valeria, Mieke Kuschnerus, and Roderik C. Lindenbergh (Jan. 2022). “Permanent Laser Scanner and Synthetic Aperture Radar Data: Correlation Characterisation at a Sandy Beach”. en. In: *Sensors* 22.6. Number: 6 Publisher: Multidisciplinary Digital Publishing Institute, p. 2311. ISSN: 1424-8220. DOI: 10.3390/s22062311. URL: <https://www.mdpi.com/1424-8220/22/6/2311> (visited on Apr. 19, 2023).
- Kuschnerus, Mieke, Roderik Lindenbergh, and Sierd De Vries (June 2022). “Assessing sandy beach width variations on intertidal time scales using permanent laser scanning”. en. In: *Proceedings of the 5th Joint International Symposium on Deformation Monitoring - JISDM 2022*. Editorial de la Universitat Politècnica de València. ISBN: 978-84-9048-979-6. DOI: 10.4995/JISDM2022.2022.13729. URL: <http://ocs.editorial.upv.es/index.php/JISDM/JISDM2022/paper/view/13729> (visited on Apr. 19, 2023).
- Kizil, Unal and Lee Tisor (Apr. 2011). “Evaluation of RTK-GPS and Total Station for applications in land surveying”. In: *Journal of Earth System Science* 120, pp. 215–221. DOI: 10.1007/s12040-011-0044-y.
- Casella, V., M. Franzini, and A. M. Manzano (June 2021). “GNSS AND PHOTOGRAMMETRY BY THE SAME TOOL: A FIRST EVALUATION OF THE LEICA GS18I RECEIVER”. en. In: *The*

- International Archives of the Photogrammetry, Remote Sensing and Spatial Information Sciences* XLIII-B2-2021, pp. 709–716. ISSN: 2194-9034. DOI: 10.5194/isprs-archives-XLIII-B2-2021-709-2021. URL: <https://isprs-archives.copernicus.org/articles/XLIII-B2-2021/709/2021/> (visited on Apr. 20, 2023).
- Murray, Nicholas J. et al. (Jan. 2019). “The global distribution and trajectory of tidal flats”. en. In: *Nature* 565.7738. Number: 7738 Publisher: Nature Publishing Group, pp. 222–225. ISSN: 1476-4687. DOI: 10.1038/s41586-018-0805-8. URL: <https://www.nature.com/articles/s41586-018-0805-8> (visited on Apr. 20, 2023).
- Pekel, Jean-François et al. (Dec. 2016). “High-resolution mapping of global surface water and its long-term changes”. en. In: *Nature* 540.7633. Number: 7633 Publisher: Nature Publishing Group, pp. 418–422. ISSN: 1476-4687. DOI: 10.1038/nature20584. URL: <https://www.nature.com/articles/nature20584> (visited on Mar. 28, 2023).
- Acharya, Tri Dev et al. (2017). “Combining Water Indices for Water and Background Threshold in Landsat Image”. en. In: *Proceedings* 2.3. Number: 3 Publisher: Multidisciplinary Digital Publishing Institute, p. 143. ISSN: 2504-3900. DOI: 10.3390/ecs-a-4-04902. URL: <https://www.mdpi.com/2504-3900/2/3/143> (visited on Apr. 20, 2023).
- Otsu, Nobuyuki (Jan. 1979). “A Threshold Selection Method from Gray-Level Histograms”. In: *IEEE Transactions on Systems, Man, and Cybernetics* 9.1. Conference Name: IEEE Transactions on Systems, Man, and Cybernetics, pp. 62–66. ISSN: 2168-2909. DOI: 10.1109/TSMC.1979.4310076.
- Chen, Louis H. Y. (Sept. 1978). “Two central limit problems for dependent random variables”. en. In: *Zeitschrift für Wahrscheinlichkeitstheorie und Verwandte Gebiete* 43.3, pp. 223–243. ISSN: 1432-2064. DOI: 10.1007/BF00536204. URL: <https://doi.org/10.1007/BF00536204> (visited on Apr. 21, 2023).
- TDS Catalog* (2023). URL: https://opendap.deltares.nl/thredds/catalog/opendap/rijkswaters_taat/jarkus/profiles/catalog.html (visited on Apr. 21, 2023).
- Diamantidou, Eleni et al. (Feb. 2020). “An Automatic Procedure for Dune Foot Position Detection: Application to the Dutch Coast”. en. In: *Journal of Coastal Research* 36.3, p. 668. ISSN: 0749-0208. DOI: 10.2112/JCOASTRES-D-19-00056.1. URL: <https://bioone.org/journals/journal-of-coastal-research/volume-36/issue-3/JCOASTRES-D-19-00056.1/An-Automatic-Procedure-for-Dune-Foot-Position-Detection--Application/10.2112/JCOASTRES-D-19-00056.1.full> (visited on Apr. 21, 2023).
- Calkoen, Floris et al. (Feb. 2023). *A novel data ecosystem for coastal analyses*. en. Tech. rep. EGU23-15964. Conference Name: EGU23. Copernicus Meetings. DOI: 10.5194/egusphere-egu23-15964. URL: <https://meetingorganizer.copernicus.org/EGU23/EGU23-15964.html> (visited on Apr. 21, 2023).
- Kroon, Aart et al. (July 2008). “Statistical analysis of coastal morphological data sets over seasonal to decadal time scales”. en. In: *Coastal Engineering*. Human Interaction with Large Scale Coastal Morphological Evolution 55.7, pp. 581–600. ISSN: 0378-3839. DOI: 10.1016/j.coastaleng.2007.11.006. URL: <https://www.sciencedirect.com/science/article/pii/S037838390700155X> (visited on Apr. 20, 2023).
- Bergsma, Erwin W. J. and Rafael Almar (June 2020). “Coastal coverage of ESA’ Sentinel 2 mission”. en. In: *Advances in Space Research* 65.11, pp. 2636–2644. ISSN: 0273-1177. DOI: 10.1016/j.asr.2020.03.001. URL: <https://www.sciencedirect.com/science/article/pii/S027311772030140X> (visited on May 5, 2023).
- Storm, Mark et al. (2017). “Cubesat Lidar Concepts for Ranging, Topology, Sample Capture, Surface, and Atmospheric Science”. en. In.

A

Profiles

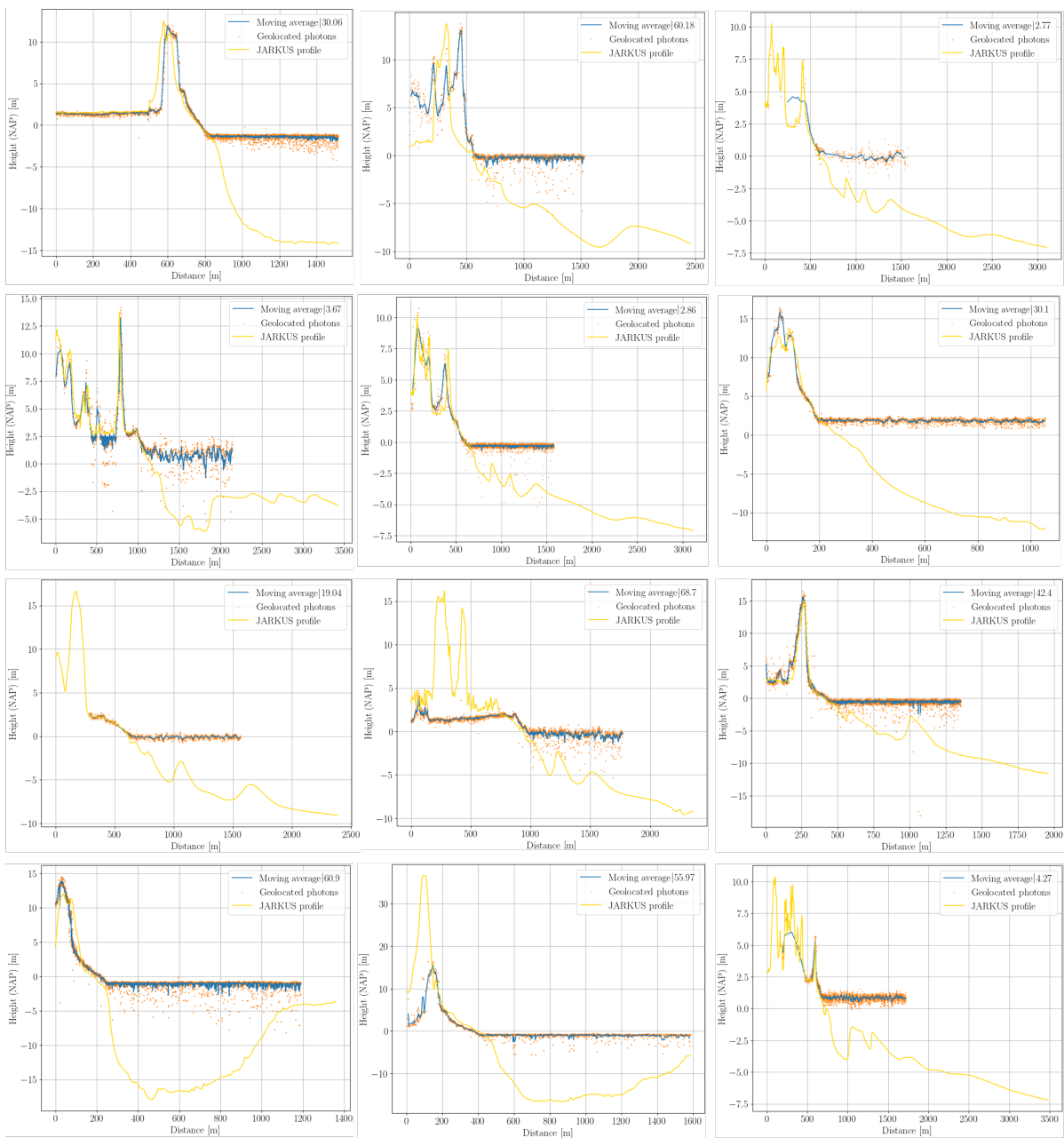


Figure A.1: Examples of profiles for different .

B

Global Boxes Sample

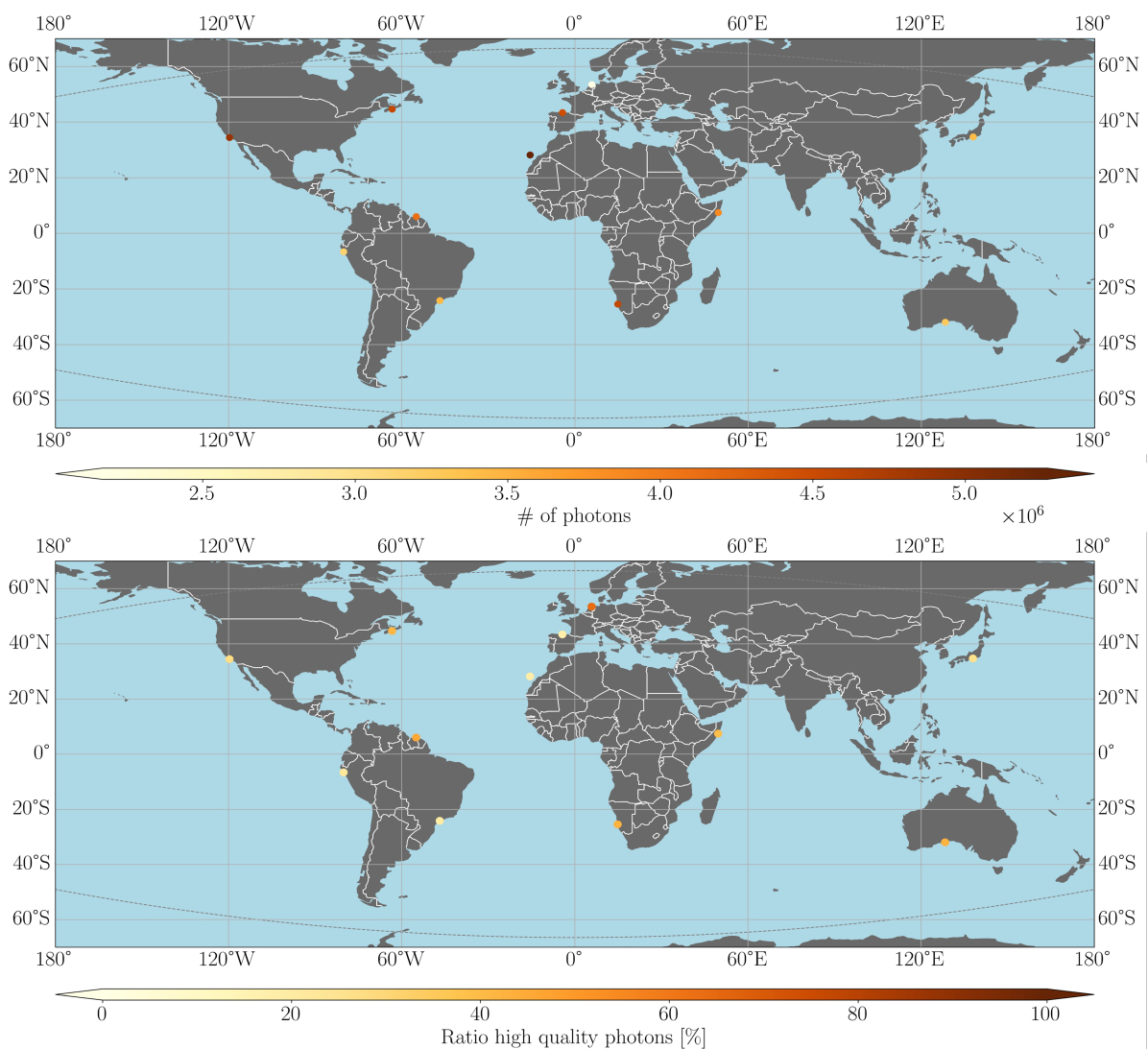


Figure B.1: Visual aid for Table 5.7. In this figure, three maps are presented with the location of the selected boxes, similar to Figure 5.16, but it shows different values: the upper panel presents the number of photons per box, the panel in the middle the ratio of high quality photons [%], and the lower panel presents the number of dates that ICESat-2 measured per box.

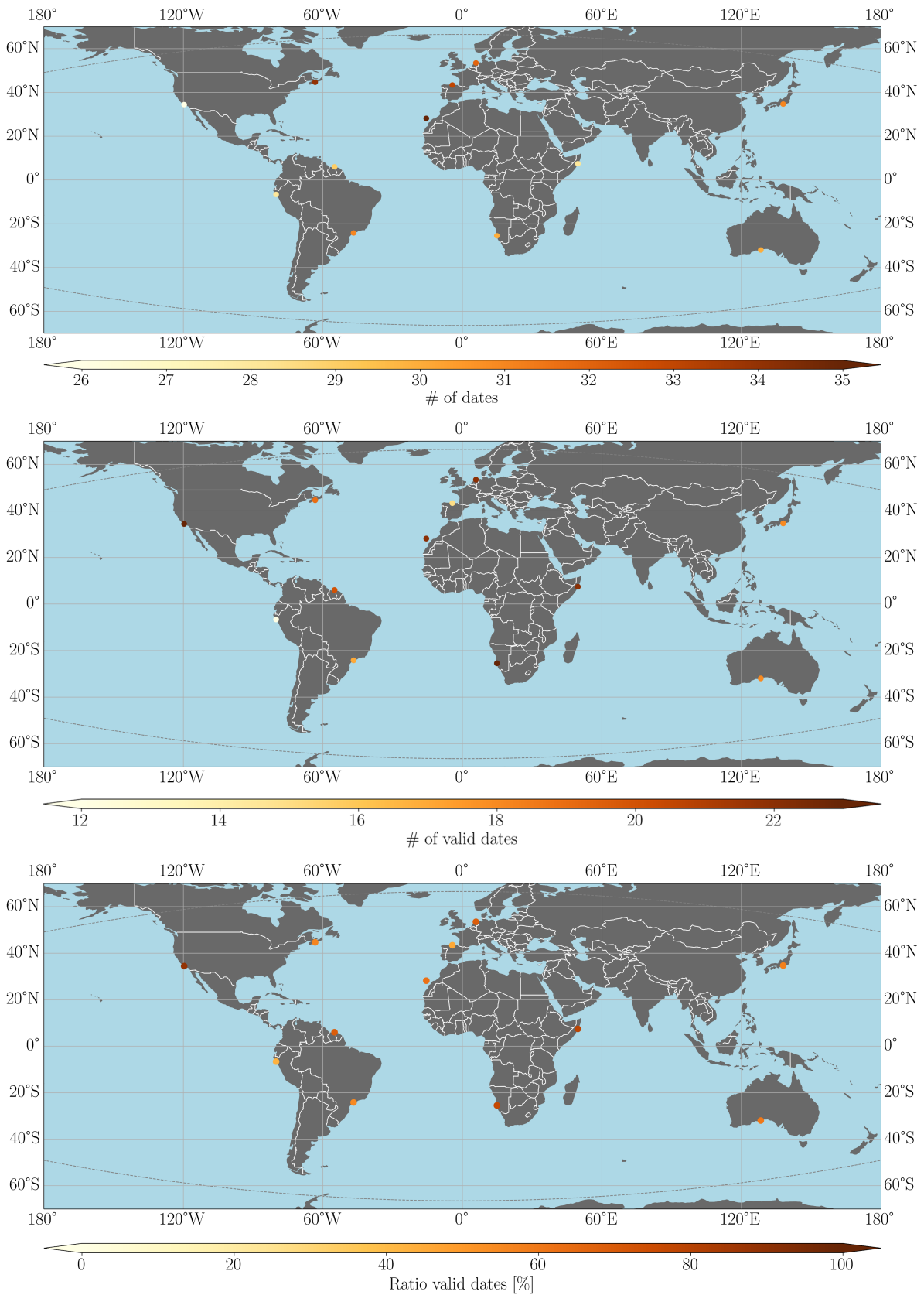


Figure B.2: Visual aid for Table 5.7. In this figure, three maps are presented with the location of the selected boxes, similar to Figure 5.16, but it shows different values: the upper panel presents the number of valid dates (dates with more than 5000 photons classified as high quality) per box, the panel in the middle the ratio of valid dates [%], and the lower panel presents the number of passes that ICESat-2 measured per box.

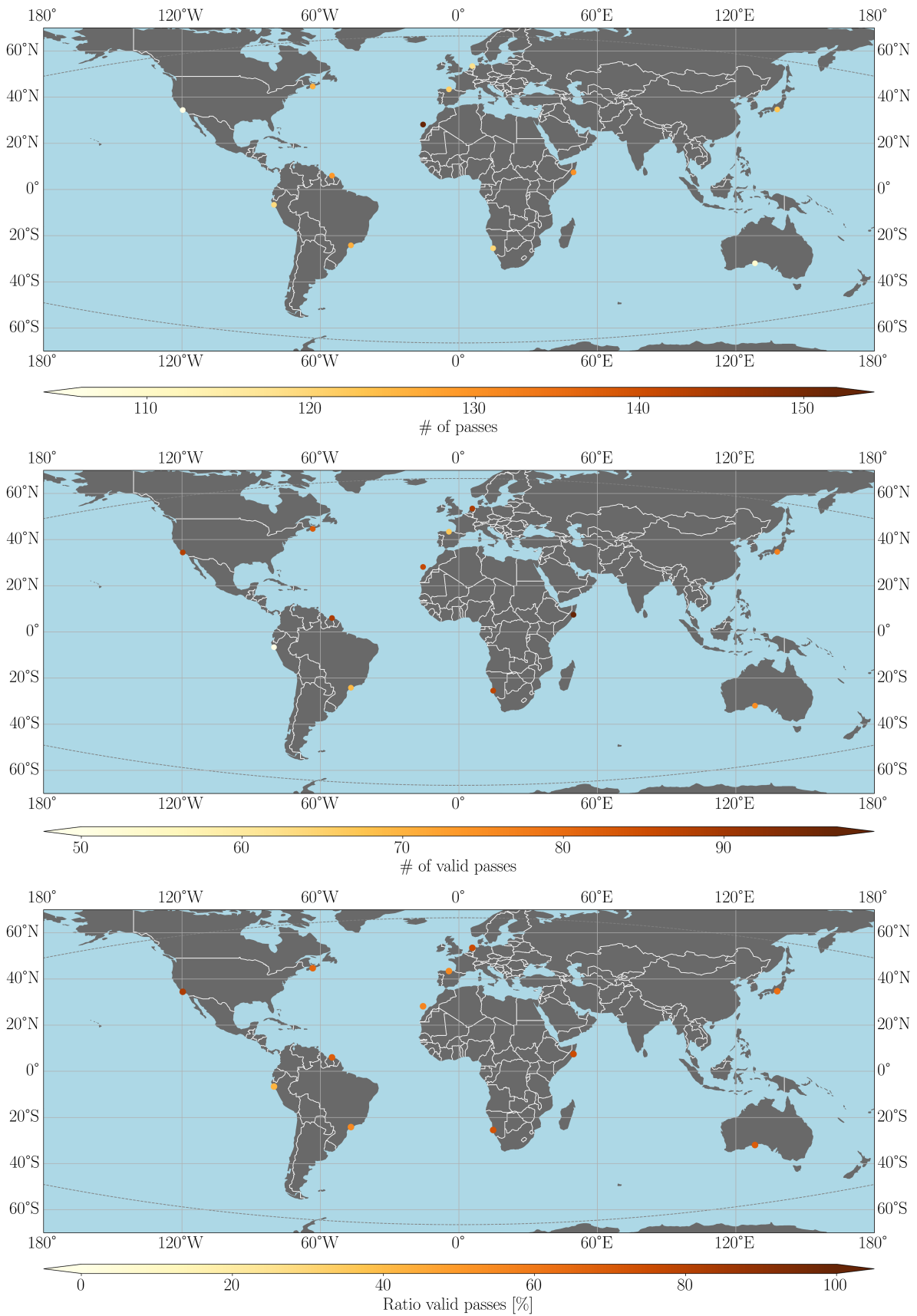


Figure B.3: Visual aid for Table 5.7. In this figure, two maps are presented with the location of the selected boxes, similar to Figure 5.16, but it shows different values: the upper panel presents the number valid passes (dates with more than 5000 photons classified as high quality) per box and the lower panel presents the ratio of valid passes [%].